Univerzita Karlova v Praze

Matematicko-fyzikální fakulta

DIPLOMOVÁ PRÁCE

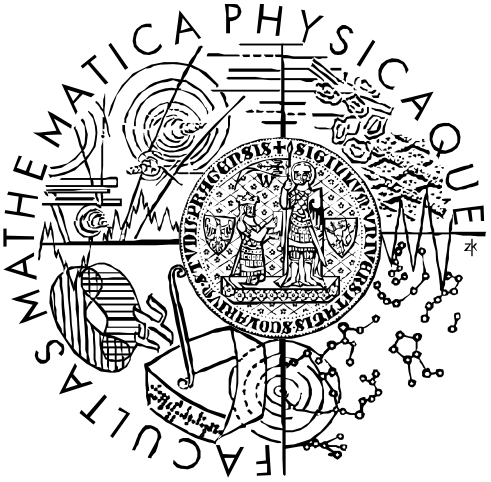

Bc. Barbara Bittová

Magnetické struktury s aplikačním potenciálem

Katedra fyziky kondenzovaných látek

Vedoucí práce: RNDr. Jana Poltierová Vejpravová, Ph.D.

Studijní obor: Fyzika kondenzovaných soustav a materiálů

2010

Charles University in Prague

Faculty of Mathematics and Physics

DIPLOMA THESIS

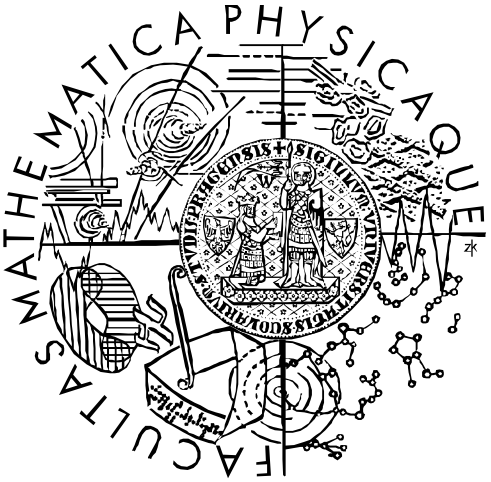

Bc. Barbara Bittová

Magnetic structures with application potential

Departemnet of Condensed Matter Physics

Supervisor: RNDr. Jana Poltierová Vejpravová, Ph.D.

Physics of Condensed systems and Materials

2010

Tímto bych chtěla poděkovat vedoucí diplomové práce, RNDr. Janě Poltierové-Vejpravové Ph.D. za podnětné a trpělivé vedení, dále Dr. Marii Puerto Morales a Dr. Alechandru Roca (ICMM CSIC Madrid) za zasvěcení do tajů přípravy nanočástic, Dr. Alexandru Dulebo (IFB AV CR Nové Hrady) za podrobné seznámení s metodou AFM, Doc. RNDr. Stanislavu Danišovi Ph.D. za konzultace strukturní analýzy a Dr. Xavierovi Roca za dodání testovacích vzorků pro MFM.

Prohlašuji, že jsem svou práci vypracovala samostatně, s výhradným použitím citovaných pramenů.

V Praze dne Bc. Barbara Bittová

Content

Název práce: Magnetické struktury s aplikačním potenciálem
Autor: Bc. Barbara Bittová
Katedra (ústav): Katedra fyziky kondenzovaných látek
Vedoucí bakalářské práce: RNDr. Jana Poltierová Vejpravová, Ph.D.
e-mail vedoucího: jana@mag.cuni.cz

Abstrakt: Hlavním zaměřením této práce je studium makroskopických a mikroskopických magnetických vlastností vybraných nanomateriálů obsahujících kobalt a železo, značná část práce se zabývá vizualizací morfologie a magnetické struktury studovaných vzorků pomocí metody magnetické silové mikroskopie (MFM) s využitím nově instalovaného skenovacího mikroskopu Multimode V od Veeca. Zkoumané nanomateriály, jmenovitě nanočástice $CoFe_2O_4$ a tenké filmy a multivrstvy SiO_2_Co_Si(111), jsou v mnoha ohledech velice slibnými materiály. Nanočástice jsou využívány např. v medicíně jako nosiče léčiv a kontrastní látky, tenké filmy jsou zkoumány z důvodu jejich potencionálního využití v paměťových médiích. Makroskopické magnetické vlastnosti vzorků jsou popisovány z hlediska superparamagnetismu. Mezičásticové interakce v nanočásticových systémech jsou diskutovány vzhledem k dosavadním znalostem, příklad silně interagujícího systému nanočástic (superspinového skla) je popsán z experimentálního hlediska. U tenkých filmů je studována jejich struktura a vývoj magnetokrystalové anizotropie. V práci jsou rovněž prezentovány první úspěšné výsledky MFM obdržené v naší laboratoři a diskuse možnosti vizualizace magnetického kontrastu superparamagnetických nanočástic.

Klíčová slova: superparamagnet (SPM), superspinové sklo (SSG), nanočástice, tenké filmy, magnetická silová mikroskopie

Title: Magnetic structures with application potential
Author: Bc. Barbara Bittová
Department: Department of condensed matter physics
Supervisor: RNDr. Jana Poltierová Vejpravová Ph.D.
Supervisor's e-mail address: jana@mag.cuni.cz

Abstract: The thesis is mainly focused on the investigation of macroscopic and microscopic magnetic properties of selected nanomaterials containing cobalt and iron, and also the capability of our new device, scanning probe microscope Multimode V by Veeco, to directly visualise morphology and magnetic structure of these samples (Magnetic Force Miscroscopy, MFM).
Investigated materials, such as $CoFe_2O_4$ nanoparticles and SiO_2_Co_Si(111) thin films and multilayers are in general promising materials in many fields. In the medicine, the nanoparticles are used as the drug targets or contrast agents whereas in electronics, the (nano)granular thin films are the starting point in fabrication of high density storage media. The macroscopic magnetic properties of our samples are discusses in a view of superparamagnetic phenomena. The interactions in systems of nanoparticles are presented theoretically within the up-to date knowledge and also experimentally by demonstrating the behavior of the strongly-interacting, super-spin-glass system. The thin films are studied in term of their granular structure and magnetic anisotropy. The morphology and the microscopic domain structure, respectively, are studied with use of the MFM. The first successful results obtained in our lab by this method are presented.
Keywords: superparamagnet (SPM), super-spin-glass (SSG), nanoparticles, thin films, magnetic force microscopy (MFM)

Introduction

The thesis belongs to the area of material science, which is dealing with the objects at the nanoscale: the nanotechnology. Nanotechnology, in its literal meaning, covers any technology done on the nanoscale that has the applications in real world. This great application potential was highlighted and defined firstly by R. Feynmann in his famous talk given in 1959 at Caltech[1]. When the size of the material is decreased from the macroscopic size (bulk) to the nanoscale, unique physical properties based on the quantum-sized effects appear[2]. Thus one, two and three dimensional nano-object such as quantum dots, nanowires, nanotubes, nanoparticles, and thin films exhibit the properties that are absolutely different from those observed in macro-size and these new materials can be used in many areas of human interest.
Nanotechnology has become one of the most exploring scientific areas in the last decade. The boom of supporting the nano-science has started in 2000 at Caltech in U.S. when the National Nanotechnology Initiative has been established[3]. Then the trend continued to Japan[4] (2001) and Europe[5] (Sixth Framework program, 2002) and it is not untrue to say that nowadays, each country with developed industry and educational system is trying to operate in this field.

Magnetic nanomaterials are mainly used in area of medical applications (detection and treatment of cancer tumours from the first stage[6], contrast agents for magnetic resonance imaging[7], MRI), and in an electronics devices such as high density magnetic storage media, smart biosensors[9,10]. The huge application potential is based on their unique magnetic properties: Frenkel and Dorfman[11] were the first to predict that a particle of a ferromagnetic material, below a critical particle size would consist of a single magnetic domain. Then Néel[12] was the first who described the magnetism of such a system (so called superparamagnetic behavior) and by the time, multiple effort was given to precious description of interactions in systems of nanoparticles, affecting their final application potential[13]. However, one of the crucial points in term of application is still to prepare single-crystalline nanoparticles with well-defined size and shape.

The thesis was in the beginning focused especially on the investigation of macroscopic magnetic properties of selected nanomaterials containing cobalt and iron, the notoriously known magnets, such as nanoparticles and granular thin films, considered in term of superparamagnetic (SPM) behavior. However, in January 2009, the possibility to directly visualise the internal magnetic structure of our samples has suddenly appeared. The department has gained one of the best scanning probe microscopes available on market (Multimode V by Veeco); thus a lot of effort devoted to this thesis has been put to learning the basic operations with the microscope.

The thesis is divided into theoretical and experimental parts, respectively. Chapter 1 describes the basics of magnetism. Chapter 2, based on the up-to date studies, properly discuss the interactions in systems of magnetic nanoparticles. Chapter 3 and 4 present the thin films in the view of their magnetic properties and the reflectivity. Chapter 5 and 6 give the background of the Scanning Probe Microscopy (SPM) a Magnetic Force Microscopy (MFM), from the basic principles up to the results from recent years. Chapter 7 summarises the experimental methods that were used in the thesis. Chapter 8 presents the first MFM phase images obtained in our lab (we have used the samples by N. Dix from Barcelona (ICMB)). Chapter 9 is mainly focused on the investigation of interactions in system of $CoFe_2O_4$ nanoparticles, but also on the comparison of samples considering different routes of preparation leading to the single-domain, highly crystalline particles. This chapter also presents possibilities of detecting the magnetostatic interactions arising from single-domain particles by MFM imaging. Chapter 10 is based on the investigation of magnetic properties of SiO_2_Co(x)_Si(111) thin films and multilayers in term of the magnetic anisotropy, also the advanced experiment of torsion magnetometry and MFM are involved. Final conclusions summarise the most important results and the further suggestions for improving the experiments by the Magnetic Force Microscopy in our lab.

1 Magnetism- basic principles

In this section, comprehension on basics of magnetism in solid state, based on the references[14-21] is presented here. Furthermore, magnetism in nanoparticles is discussed in the context of the up-to-date knowledge in the next chapter.

1.1 Constants, units and basic quantities

At first, let us define the fundamental constants, frequently used in this work:

quantity	*SI units*
electron charge e	$1{,}602.10^{-19}\ C$
electron mass m_e	$9.1095\ .10^{-31}\ kg$
Bohr magneton μ_B	$9.2741.10^{-24}\ J.T^{-1}$
reduced Planck constant $\hbar$	$1.0546.\ 10^{-34}\ J.s$
vacuum permeability μ_0	$4\pi.10^{-7}\ Hm^{-1}$
Boltzman constant k_B	$1.3807.10^{-23}\ J.K^{-1}$
Avogadro constant N_A	$6.022\ 10^{23}\ mol^{-1}$

Regarding at first the magnetism as the consequence of electric current, the magnetic moment, μ is defined as:

$$\mu = I.A, \tag{1-1}$$

where the magnetic moment is created by the current loop of area $\boldsymbol{A}$, in which the current, I is flowing. The next step is to define *magnetization* as a sum of magnetic dipoles μ:

$$M = \sum_{i=1}^{N} \mu_i \ / V\,, \tag{1-2}$$

where N is a number of magnetic units per unit volume and V is the volume of a magnetic unit. Magnetization could be either induced by magnetic field (paramagnet, diamagnet) or to be spontaneous (magnetically ordered materials).
As already mentioned, magnetic fields are created by electric currents. The magnetic field in free space created by a current element $I\mathrm{d}\boldsymbol{l}$ is given by the Biot-Savart law:

$$\delta \boldsymbol{B} = -\left(\mu_0 / 4\pi\right) I(\boldsymbol{r} \times d\boldsymbol{l}) / r^3\,, \tag{1-3}$$

where $\boldsymbol{B}$ is the magnetic field induction measured in Tesla, T. The magnetic fields are described by two quantities; induction, $\boldsymbol{B}$ and intensity, $\boldsymbol{H}$ (measured in Am^{-1}). The

reason why we introduce the magnetic field intensity, $\boldsymbol{H}$, originates from the Maxwell equations and Amper's law; $\boldsymbol{H}$ is the response of material to the free current flow, otherwise *rot* $\boldsymbol{B}$ is proportional to current which is the superposition of current associated with the magnetization (which is un-measurable) and the free current.
These two quantities are in free space related via formula:

$$\boldsymbol{B} = \mu_0 \boldsymbol{H} . \qquad (1\text{-}4)$$

If one describes magnetic behavior of matter, it is necessary to consider the macroscopic magnetization, $\boldsymbol{M}$, which arises from internal magnetic field in the matter; the finite magnetic induction is then defined as:

$$\boldsymbol{B} = \mu_0 (\boldsymbol{H} + \lambda \boldsymbol{M}) . \qquad (1\text{-}5)$$

Magnetic susceptibility is defined as the linear response of magnetization to the applied field:

$$\chi = \frac{d\boldsymbol{M}}{d\boldsymbol{H}} , \qquad (1\text{-}6)$$

where $\boldsymbol{H}$ is the intensity of the applied external magnetic field and $\boldsymbol{M}$ is the magnetization. Depending on the susceptibility, the paramagnetic (χ is positive) and diamagnetic (χ is negative) materials are defined.
More general, the response of magnetically ordered material to the magnetic field could be non-linear, irreversible and time-dependent; leading to the famous *hysteresis behavior*, where magnetization as a function of the magnetic field $\boldsymbol{M} = f(\mathbf{H})$ is measured.

1.2 Atomic magnetism

Let us consider a single free atom. In quantum mechanics, magnetic moment is associated with the total angular momentum, J of electron (there is an analogy with the current loop), which has three contributions:
a) spin moment (S),
b) orbital moment (L),
c) change of the orbital moment due to the external magnetic field.

Magnetism is in general connected with the partially occupied shells (because both the spin and the orbital moments exist only in the atom with unclosed electron shells). Magnetic moment of the ground state of the free atom with an unfilled shell (ion) is described by the well-known Hund's rules.
If the Hamiltonian, H of an free atom in presence of uniform magnetic field, $\boldsymbol{B}$ is introduced:

$$H = \sum_i \left(\frac{\boldsymbol{p}_i^{\,2}}{2m_e} + V_i \right) + \mu_B (\boldsymbol{L} + g\boldsymbol{S})\boldsymbol{B} + \sum_i \frac{e^2}{8m_e} (\boldsymbol{B} \times \boldsymbol{r}_i)^2 \quad , \tag{1-7}$$

the dependence of the magnetic susceptibility on the shell occupancy can be treated, using the formula for energy shift calculation through the second order perturbation theory. This is the so-called model of localized electrons.

1.2.1 Larmor diamagnetism

Considering the solid composed of non-interacting ions with filled electron shells, the total angular (and also spin and orbital moments) is equal to zero; so only the last term in (1-7) contributes to the resulting susceptibility, which is given as:

$$\chi_{dia} = -\frac{N}{V} \frac{\mu_0 e^2}{6m_e} \sum_i \left\langle r_i^{\,2} \right\rangle \, . \tag{1-8}$$

1.2.2 Van Vleck paramagnetism

If the ionic shell is one electron short to be half-filled (J = 0), the paramagnetic contribution to the Larmor diamagnetic susceptibility arises as the so-called Van Vleck paramagnetism (magnetic moments align parallel to the applied field):

$$\Delta E_0 = \sum_n \frac{\left| \langle 0 | \mu_B (\boldsymbol{L} + g\boldsymbol{S})\boldsymbol{B} | n \rangle \right|_2}{E_0 - E_n} + \sum_i \frac{e^2}{8m_e} (\boldsymbol{B} \times \boldsymbol{r}_i)^2 \, . \tag{1-9}$$

1.2.3 Paramagnetism of non-interacting ions

The magnetization of set of non-interacting ions with non-zero J at finite temperature T is given by the Brillouin function as

$$M = Ng \; J\mu_B B_J(x), \tag{1-10}$$

$$x \equiv \frac{gJ\mu_B B}{k_B T} \equiv \frac{\mu B}{k_B T}, \tag{1-11}$$

where g is the Landée g factor

$$g = \frac{3}{2} + \frac{S(S+1) - L(L+1)}{2J(J+1)} \quad . \tag{1-12}$$

For huge number of spins in the system ($J \approx \infty$), (1-10) can be simplified to:

$$M = M_0 L(x), \tag{1-13}$$

where M_0 is the saturated magnetization and $L(x)$ is the Langevin function:

$$L(x) = \lim_{J\to\infty} B_J(x) = \coth x - \frac{1}{x}. \tag{1-14}$$

The final paramagnetic susceptibility of non-interacting ions obeys the *Curie law*:

$$\chi = \frac{N}{V}\frac{(g\mu_B)^2}{3}\frac{J(J+1)}{k_B T} = \frac{C}{T}\ , \tag{1-15}$$

where C is the Curie constant.

1.3 Magnetism of free electrons

Solving the problem of magnetism of free electron gas is a right way how to describe magnetism of metals. The conducting electrons are not localized like those in partially filled electron shells, so they respond independently to the applied magnetic field. The magnetic moment of the electron is equal to the Bohr magneton, μ_B, and the total magnetization of electron gas is the sum of electrons with magnetic moments pointing parallel and anti-parallel to the field, ***H***

$$M = -\mu_B (n_+ - n_-), \tag{1-16}$$

n_+ and n_- are number of electrons per unit volume with spins pointing parallel or anti-parallel with respect to the magnetic field, respectively.

1.3.1 Pauli paramagnetism

Introducing the density of electron levels for a given spin orientation and energy, $g\pm(\varepsilon)$; presence of the field, ***H*** creates an imbalance in population of the spins pointing up and down:

$$g\pm(\varepsilon) = \frac{1}{2} g(\varepsilon \mp \mu_B H)\ , \tag{1.-17}$$

and gives rise to the *Pauli paramagnetic susceptibility:*

$$\chi_{Pauli} = \mu_B{}^2 g(\varepsilon_F)\ , \tag{1-18}$$

($g(\varepsilon_F)$ is the density of states at the Fermi level) which is two order of magnitude smaller than the free ion paramagnetic susceptibility at room temperature.

1.3.2 Landau diamagnetism

The paramagnetism of the free electron gas is associated with the spin of the electrons; however, there is also orbital contribution to the antiparallel magnetization and hence to the susceptibility, known as the *Landau diamagnetism*,

$$\chi_{Landau} = -\frac{1}{3}\chi_{Pauli} \ , \qquad (1\text{-}19)$$

The temperature dependencies of the all above-discussed magnetic susceptibilities are illustrated in Fig. 1.1.

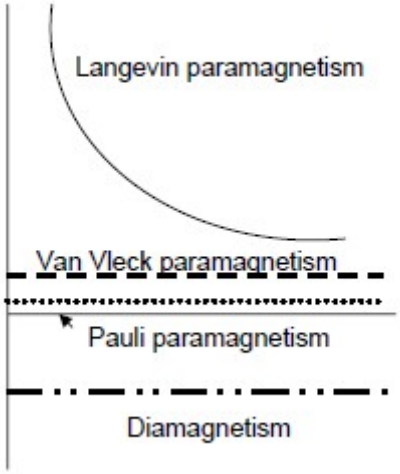

Fig. 1.1: The image of temperature dependence of the magnetic susceptibilities. The image adapted from the Kittel course-book[17].

1.4 Magnetic ordering

A lot of materials exhibit a non-vanishing magnetization bellow a specific temperature; this magnetization is created by a specific alignment of magnetic ions and the material is said to be magnetically ordered. The magnetism of magnetically ordered material can be described by two types of basic models, considering either the magnetic moments localized at the lattice sites or the so-called band models. Treating localized models of magnetism, all of them use at the beginning the Heisenberg Hamiltonian, which describes interaction between the spins localized on the sites *i* and *j*:

$$H = \sum_{\substack{i,j \\ i \neq j}} J_{ij} S_i . S_j \ , \qquad (1\text{-}20)$$

where J_{ij} is the exchange integral describing interaction between spins S_i and S_j.

1.4.1 Interactions between magnetic moments

There are several types of interactions between magnetic moments. The simplest one is the *dipole-dipole interaction* which energy is inversely proportional to the $1/r^3$ (***r*** is the separation distance).

Any interaction between spins leading to a magnetically ordered state is known as the exchange interaction, several types are described here:

Direct exchange interaction arises from the Coulomb interaction among electrons from the two neighboring ions. This interaction is common in 3d (4d, 5d) metals.

Superexchange is an indirect exchange interaction between non-neighboring magnetic ions, which is mediated by orbitals of a non-magnetic ion placed in between.

RKKY (Ruderman–Kittel–Kasuya–Yosida) is a type of indirect interaction observed in metals, mediated by spin-polarization of the conducting electrons by localized spins. It could be either ferromagnetic or antiferromagnetic depending on the interatomic distances.

1.4.2 Ferromagnetism

Ferromagnet in ferromagnetic state exhibits spontaneous magnetization without presence of any external field as a consequence of exchange interactions acting between magnetic ions. At T = 0 K, all magnetic moments favour parallel alignment and magnetization has its maximum possible value, M_S. With increasing temperature, magnetization decreases (because of the thermal fluctuations) until it becomes zero at a characteristic temperature called the Curie temperature, T_C. For the temperatures above the T_C, the system is in the paramagnetic state without any magnetic order. The magnetic phase transition at the Curie temperature is a type of the second order phase transition.

One of the easiest approaches to describe ferromagnetism is the *Weiss model*, in which the exchange interaction J_{ij} is replaced by an effective molecular field, $\boldsymbol{B}_m = \lambda \boldsymbol{M}$, produced by all neighbouring spins. Hamiltonian described by (1-20) is transformed into that for paramagnet in magnetic field $\boldsymbol{B} + \boldsymbol{B}_m$ (second term in eq. (1-7)).

Magnetization is also given by the Brillouin function or the Langevin function if J goes to infinity, eq. (1-10); x in (1-11) is now modified to:

$$x = \frac{g\mu_B J(B + \lambda M)}{k_B T} \quad . \tag{1-21}$$

The susceptibility of a ferromagnet in paramagnetic state above the Curie temperature, T_C is given by the *Currie-Weiss law*:

$$\chi = \frac{C}{T - T_C} . \qquad (1\text{-}22)$$

Another elegant way how to show that total magnetization has non-zero value only for temperatures above the T_C is the famous Landau approach in which the free energy of a system is taken in form of a power series with only even powers of M. Finding the ground state of a system by minimizing the F with respect to the M implies the behavior described above. The temperature dependence of magnetization and susceptibility in the ferromagnet is illustrated in Fig. 1.2.

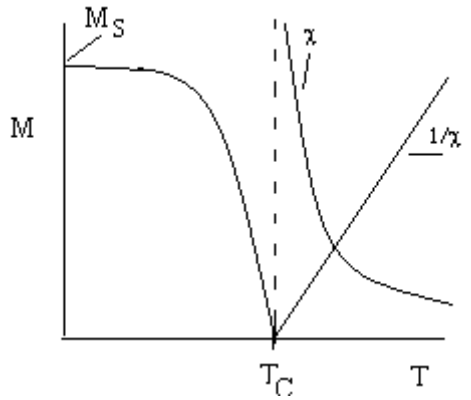

Fig. 1.2: The temperature dependence of magnetization and susceptibility in the ferromagnet.

Domain structure

In a ferromagnet below the T_C, the system of the spins splits into separate regions with the same direction of the internal magnetization, so-called magnetic domains; thus the total magnetostatic energy is minimised. Orientation of the domains depends both on the temperature and the applied external magnetic field. Domains are separated by the boundaries called the domain walls. Depending on the configuration of magnetic moments inside the wall, we distinguish between the Néel and the Bloch wall, respectively; that separate the domains with opposite magnetization (the examples of the domain walls are given in Chap. 3).

It is clear that the direction of the final magnetization in a sample depends on the domain structure, which is influenced by the crystal structure and the shape of the sample. Furthermore, the energy of a magnetic material depends on the direction of the magnetization with respect to the crystal axes. This important property is known as the *magnetic anisotropy,* which acts as the origin of the hysteresis and coercivity. The different types of anisotropies that contribute to the total magnetic anisotropy are:

1) the Magnetocrystalline Anisotropy,

which is the main contribution to the total magnetic anisotropy, arising from the crystal symmetry. It is defined as the energy that needs to be applied to deflect the magnetic moment in single crystal from the easy to the hard axis of magnetization. In the simplest form, for an uniaxial magnet of volume V, the uniaxial magnetocrystalline anisotropy is given as:

$$E_A = K_1 V \sin^2 \theta \,, \tag{1-23}$$

where K_1 is the first order anisotropy constant and θ is the angle between direction of the magnetic moment and the easy axis.

In a lot of magnetic materials with higher crystal symmetry, the additional non-uniaxial contributions to the anisotropy constants have to be involved.

2) the Shape Anisotropy,

which is the demagnetizing energy associated with the sample shape.

Because of the limited size of the sample, the internal magnetic field proportional to the local magnetization, $\boldsymbol{M}$ produces the surface charge distribution, which is the source of another magnetic field, called the demagnetizing field (which points in opposite direction to the field producing it).

Thus the internal magnetic field, $\boldsymbol{H}_\mathrm{i}$, in the sample is given by:

$$\boldsymbol{H}_\mathrm{i} = \boldsymbol{H}_\mathrm{ext} - \boldsymbol{H}_\mathrm{D}\,, \tag{1-24}$$

where $\boldsymbol{H}_\mathrm{ext}$ is the external magnetic field and $\boldsymbol{H}_\mathrm{D}$ is the demagnetizing field, which is defined for a ferromagnet of an arbitrary shape as a:

$$\boldsymbol{H}_D = -\sum N_{ij} \boldsymbol{M}_j \,, \tag{1-25}$$

where N is the demagnetizing factor (tensor in general case) and $\boldsymbol{M}_\mathrm{j}$ is the local magnetic moment. Demagnetizing factor, N can be diagonalized for spatial symmetric geometries (such as for spheres, wires, disk, thin films), so just the coefficients N_x, N_y and N_z survive. The coefficients for a flat plane and disk perpendicular to the z-axis are namely 0, 0 and 1 whereas those for the sphere are all reduced to 1/3.

The demagnetization energy follows general formula:

$$E_D = \frac{\mu_0}{2} \int_V \boldsymbol{M}\boldsymbol{H}_D dv \,. \tag{1-26}$$

3) other anisotropies

contribute to the total magnetic anisotropy. One of these is the magneto-elastic anisotropy caused by mechanical strain, which is physically equivalent to the magnetocrystalline anisotropy, but with lowered symmetry.

Measuring the magnetization of a ferromagnet as a function of the applied magnetic field, one obtains a typical hysteresis loop. Depending on the direction in which the field is applied, the easy and the hard axis of magnetization, respectively, two limiting cases (Fig. 1.4. (a) and (c)) occur.

In majority of ferromagnetic samples, the final magnetization in the zero external field is zero (if the lowest energy state is the demagnetised one). If the field is applied in some of non-specified direction, the domains start to follow the field orientation with increasing intensity of the external magnetic field and final magnetization raise upon reaching specific value called the saturated magnetization, $M_{s.}$ Appling of the magnetic field causes irreversible changes in material's permanent magnetization in zero magnetic field, reaching in the so-called remanent magnetization, M_R. The zero magnetization is set up for the coercivity field, H_C. The behavior of the ferromagnet is similar for opposite polarity of the applied magnetic field, magnetization of particular domains turns to the opposite directions, and the same values of the specific quantities in opposite directions of the applied field are obtained. The example is illustrated in Fig. 1.3.

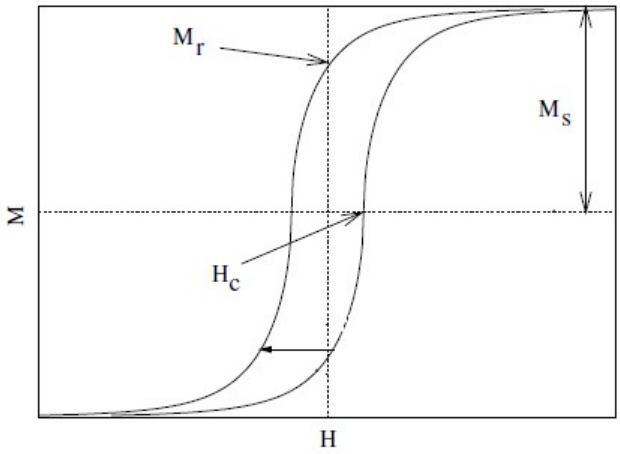

Fig. 1.3: Hysteresis curve in a ferromagnet, adapted from paper by Tannous and Geraltowski[19].

If we inspect the dependence of magnetization vs. intensity of the magnetic field for a system measured in temperatures above its T_C, the hysteresis loops vanishes.

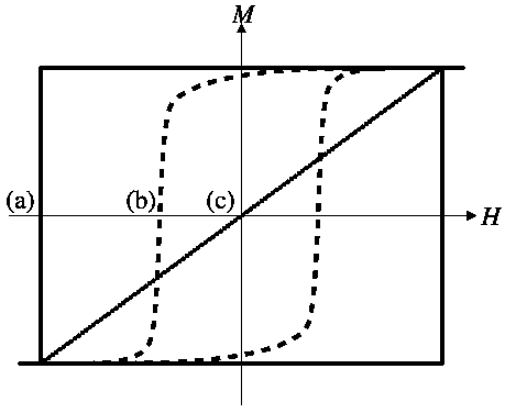

Fig. 1.4: Shape of hysteresis loop as a function of $\Theta_{(H)}$, the angle between anisotropy axis and applied field H, for: (a) Θ_H, = 0°, (b) 45° and (c) 90°. Adapted from J. Bland Thesis[21].

Stoner-Wohlfarth model

When the size of a ferromagnetic sample reaches critical size, surface (and also domain wall) energies became more energetically costly than the volume energies, so the sample minimizes its total energy through removing of the domain walls and establishing itself as a single domain. Stoner-Wohlfart model is the simple description of magnetic properties of non or weakly interacting single-domain grains, considering their coherent rotation.

Because these single-domain grain posses uniaxial anisotropy, direction of magnetic moment, μ, in presence of external magnetic field is given by competition of alignment forces: that one which is given by the uniaxial anisotropy (characterized by K_1), and second one given by the external magnetic field, H, described in similar meaning as eq. (1-23) like:

$$E_A = K_1 V \sin^2\theta - HM_s \cos(\theta - \phi), \qquad (1\text{-}27)$$

where K_1 has similar meaning as in eq. (1-23), M_S is the saturated magnetic moment of the particle, θ is the angle between the M and H and φ is the angles between H and particles anisotropy axis.

If the influence of demagnetising field is also considered (for the ellipsoidal grain), the demagnetising coefficients parallel and perpendicular to the easy axis of the particle are involved in the anisotropy constant K_1, which verges to the anisotropy energy constant K_{eff}. Then the energy of Stoner particle is given as[19]:

$$E_A = K_{eff} V \sin^2\theta - HM_s \cos(\theta - \phi). \qquad (1\text{-}28)$$

Applying the magnetic field, ***H*** and measuring the magnetization, ***M***, two limiting cases that depend on the direction of grain easy axis occur. The first one is the case represented by the square loop, which coercivity is equal to the anisotropy field

($2K_{eff}/\mu_0 M_s$), when the applied field is perpendicular to the grain easy axis. The second case is the degenerated line with the zero coercivity, which slope is given by $d\boldsymbol{M}/d\boldsymbol{H}=2K/\mu_0.M_s^2$, observed when the grain easy axis is parallel to the applied field.
The hysteresis loops for a single domain particle in magnetic field applied in different direction are depicted in Fig. 1.5.
When the predictions of Stoner-Wohlfart model are compared with the macroscopic ferromagnetic material, the coercivity is reduced with respect to that of the model predictions.

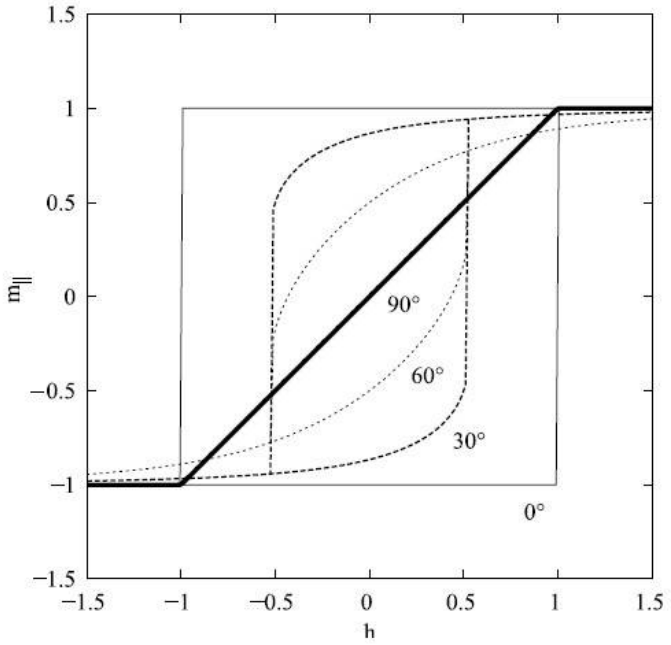

Fig. 1.5: Stoner-Wohlfarth model. Sketch of the hysteresis loops for various angles. Adapted from paper by Tannous and Geraltowski[19].

1.4.3 Antiferromagnetism

In a simple antiferromagnetic material, the magnetic lattice can be described by two equivalent sub-lattices, A and B. The A atoms have only the B atoms as the nearest neighbours and vice versa. The magnetizations of the sub-lattices are anti-parallel so the finite magnetization is zero below the temperature of the ordering, called the Néel temperature, T_N. At $T = 0$ K, each sub-lattice has its maximum magnetization and with the increasing temperature, the thermal activation reduces the magnetizations in the same way as in ferromagnets.
In case of the magnetic susceptibility, we obtain the law similar to the Curie-Weiss law in ferromagnets. The *Curie-Weiss law* for the antiferromagnet is defined as:

$$\chi = \frac{C}{T + T_N}, \; T_N = -\theta_p . \tag{1-30}$$

The temperature dependence of the susceptibility for antiferromagnet is depicted in Fig. 1.6.

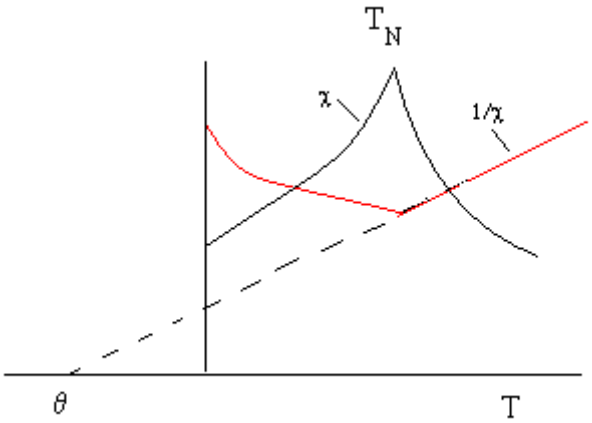

Fig. 1.6: The susceptibility and inverse susceptibility of an antiferromagnet with respect to temperature.

1.4.4 Ferrimagnetism

Ferrimagnetism can be regarded as the special case of antiferromagnetism in which the magnetic moments of sub-lattices A and B are not compensated (equal); thus the ferrimagnet exhibit the net magnetic moment even at zero magnetic field and temperature. Each sub-lattice can dominates at different temperature so the evolution of net magnetization with temperature can be either regarded as the reduction to zero from positive (or negative) values, up to changing the sign of the magnetization.
The name "ferrimagnet' was originally established to describe magnetic behavior of ferrites-magnetic oxides with chemical formula $MO.Fe_2O_3$, where M is the divalent ion (Zn^{2+}, Fe^{2+}, Co^{2+} etc.). The structure of cubic ferrites is known as the spinel structure[22] (space group Fd-3m), composed of two types of lattices sites for the cations.

The oxygen ions create the face-centre-cubic lattice (FCC) in which metallic ions occupy either tetrahedral (A) or octahedral (B) coordinates. In a normal spinel arrangement, divalent ion (M^{2+}) occupies tetrahedral site and trivalent ion (Fe^{3+}) octahedral site. In an inverse spinel arrangement, the half of the M^{2+} is present on the B sites, while the trivalent ion occupies all A sites and other half of the B sites. In this case, magnetic moments of trivalent ions are antiparallel, thus the total magnetic moment is given only by M^{2+} ions.

Cobalt-ferrite oxide, $CoFe_2O_4$, belongs to the family of inverse spinels; thus the total magnetic moment per lattice unit is $3\mu_B$ (in a low spin state when the energy of crystal field is weaker than the coulomb pairing energy).

2 Magnetism in nanoparticles

2.1 Superparamagnetism and related phenomena

Superparamagnetic state is defined for system of magnetic non-interacting single-domain particles[12], whose susceptibility follows the Curie law and magnetization curve can be described by the Langevin function (explained bellow). The critical size of a magnetic domain in a classical bulk ferromagnetic material is typically 10^{-8}-10^{-9} m, which also defines the critical size of a single ferromagnetic nanoparticle[14].

Following parameters and laws sufficiently defines the SPM system:

1) *Particle magnetization,* μ

The first assumption of SPM nanoparticle considers coherent rotation of spins inside the particle; thus the resulting net particle magnetic moment, μ can be represented by a single vector[23] as a sum of single spins (that's the reason why the particle magnetic moment is sometimes called the *superspin*):

$$\mu = \sum_i \mu_i \,. \qquad (2\text{-}1)$$

2) The *blocking temperature*, T_B

The T_B can be characterized as a freezing temperature of the nanoparticle's magnetic moment (superspin). It is the analogy with the Curie temperature, T_C in ferromagnets. The T_B can be also defined as a critical point of a phase transition between the blocked and the superparamagnetic state, respectively; the point in which the system exhibits a phase transition from a high temperature disordered state to the low temperature ordered state[14]. For temperatures above the T_B, a stable bulk magnetization cannot be established due to the thermal fluctuations and the magnetic susceptiblity of the system exhibits the SPM behaviour[12] following the Curie law. The random orientation of each magnetic moment causes the reduction of the total magnetization. For the temperatures bellow the T_B, the superspins of the particles freeze in a random orientation (they cannot rotate freely because of an energy barrier). The thermal activation of particles cannot overcome the particle anisotropy energy, E_A which serves as the energy barrier for blocking the flips of magnetic moments[14] and the magnetic moment of each particle rotates to the nearest easy axes of magnetization (we obtain nonzero coercivity field H_C, similarly as in ferromagnets). T_B increases with the increasing nanoparticle size; the larger particles of the same material become superparamagnetic at higher temperatures than the smaller ones.

3) The intrinsic *magnetocrystalline anisotropy energy* E_A

As was already mentioned in Chap. 1, the term 'magnetic anisotropy' is used to describe the dependence of the internal energy on the direction of the spontaneous

magnetization of the ferro/ferrimagnetic nanoparticle, creating the "easy" and "hard" directions of the magnetization. In general, a bulk sample of a ferromagnet exhibits magnetic anisotropy with the same symmetry as is the symmetry of the crystal structure[13]. The magnetic anisotropy, E_A of nanoparticle is usually defined for two basic symmetries - the cubic and the unaxial ones. The uniaxial anisotropy, E_A is defined in its simplest form (without considering the shape and surface contributions) in Chap. 1, eq. (1-23)[24].

As has been previously declared, if the single domain particles do not have spherical symmetry or there is some kind of inter-particle interaction, the magnetic anisotropy is accompanied with shape and surface contributions. Considering only effective anisotropy constant in the same meaning as in Chap. 1, $K_{eff.,}$ it is useful to treat both contributions to the anisotropy constant separately and the anisotropy energy for a nanoparticle can be written in a term:

$$E_A = K_{eff} V = K_b V + K_s(d) A\,, \qquad (2\text{-}2)$$

where K_b is the bulk anisotropy constant, K_s is the surface anisotropy constant, d is the particle diameter and A is the particle surface area[25]. In the system of non-interacting nanoparticles, core (bulk) anisotropy is more or less equivalent to the surface anisotropy (without consideration of the particle size). Surface anisotropy energy becomes significant when the particle size decreases or there is some kind of inter-particle interaction, which changes the natural spin alignment at the surface (in ideal case, the spin alignment is homogenous through the whole particle). Like in the "chicken and egg scenario", large surface anisotropy causes the surface influences the core structure and the interaction between particles is set up (through the exchange coupling). Finally, the magnitude of the particle magnetic moment is changed in comparison with the case of a particle in which the surface and the bulk anisotropies are equal[26].

It is very difficult to estimate K_s for nanoparticles; in the simplest case of a spherical particle, it is defined as $K_s = K_{eff}\, d/6$[25]. Recently, K_s has been determined experimentally by measurements of the ac susceptibility under pressure[27].

4) *Relaxation phenomena*

As has been already mentioned, for the temperatures above the T_B, the particle's magnetic moment rotates due to thermal fluctuations, when the thermal energy overcomes the energy barrier of the particle given by the E_A. The relaxation process in a system of single domain naoparticles was first proposed and studied by Néel in 1949[12] and further developed by Brown in 1963[28]. Relaxations of nanoparticles in SPM regime obey the Arrhenius law:

$$M(t) = M_0 \exp(-t/\tau)\,, \qquad (2\text{-}3)$$

where $M(t)$ is the total magnetization of sample at time t, M_0 is the initial magnetization and τ is the characteristic relaxation time[23] (or let say the particle switching time), when the magnetic moment of the particle rotates to the easy axis of magnetization.

The characteristic relaxation time, τ of the particle's moment is given by the Arrhenius-Néel law[29]:

$$\tau = \tau_0 \exp\left(-\frac{K_{eff}V}{k_BT}\right) = \tau_0 \exp\left(-\frac{E_A}{k_BT}\right), \qquad (2\text{-}4)$$

where K_{eff} is the effective anisotropy constant, V is the particle volume, T is the temperature and E_A is the anisotropy energy. τ_0 can be experimentally determined or theoretically calculated and ranges typically from 10^{-9} to 10^{-12} s for superparamagnetic systems[13]. It is important to remark that the system appears to be static when τ becomes much larger than the measuring time t of the used particular experimental technique[14].

5) Magnetization curves- *Langevin equation*

Considering a system of monodisperse non-interacting mono-domain nanoparticles with magnetic moments μ, the system behavior is the same as in the case of paramagnetism and follows the Langevin equation, in which the superspins are considered instead of the single spins.

There is he non-negligible particle size and hence magnetic moment distribution in the real systems. For a given distribution of magnetic moment, $f(\mu)$, the macroscopic magnetization is given by the weight sum of Langevin functions:

$$M(H,T) = \int_0^\infty L(\mu)M_s = \int_0^\infty \mu L(\frac{\mu H}{k_BT}) f(\mu)d\mu \ , \qquad (2\text{-}5)$$

where $f(\mu)$ is the log-normal distribution of magnetic moments:

$$f(\mu) = \frac{N}{\sqrt{2\pi}} \exp(\frac{-\ln^2(\mu/\mu_0)}{2\sigma^2} \ . \qquad (2\text{-}6)$$

2.2 SPM system with interactions

Pure superparamagnetic behavior is practically observed only in extremely diluted samples (like ferrofluids with low density or nanoparticles diluted in a matrix). In the real concentrated systems, in which the particles are close enough, additional interparticle interactions are noticeable and affect the macroscopic magnetic

properties[23,30]. It has been shown that with increasing concentration of the particles, the magnetic behavior may evolve from superparamagnetic to spin-glass-like behavior[13,30] .

There are several types of inter-particle interactions in granular nanoparticle systems: RKKY, dipolar, direct exchange (among touching particles) or superexchange[23]. It is extremely difficult (or rather impossible) to experimentally determine, which type of interaction is playing the main and incident roles in the examined sample, because the combined effects of interactions, particle shape, distribution of sizes and anisotropy axis, surface effects and surface-core interactions act together.

Depending on the strength of the inter-particle interactions, the weakly and strongly interacting systems are defined. The examples of weakly interacting systems are the SPM-with interaction and superferromagnets (SFM); strongly interacting systems are the super-spin glass (SSG) or a system, which has the attributes of the SSG but the particle behavior is quite different, theso called super-spin-glass-like systems. Basic properties of each system are described in the next part, illustrations are summarised in Appendix A.

2.2.1 Superferromagnetism

Superferromagnetism is a term, which describes the collective behavior in clusters of nanoparticles, which results in a behavior of a large effective magnetic nanoparticle[23]. The major difference between the super-paramagnetic and the super-ferromagnetic system is (only) in case of existence of the dipolar interparticle interaction between the superspins, leading to the ferromagnetic-like coupling of particles. Even if the ferromagnetic coupling between particles occurs, it has no distinctive effect on the blocking temperature. Above the T_B, the magnetic susceptibility corresponds to the Curie-Weiss law instead of the simple Curie law valid in case of ideal superparamagnets. Similarly, the field-cooled (FC) curve does not follow the Curie law down to low temperatures; there is a saturation of the FC magnetization at low temperatures due to the interparticle exchange interaction (explanation and example is given in Appendix A).

2.2.2 Interacting Superparamagnet

This model considers dipolar interactions as a perturbation of the superparamagnetic regime[23]. It is necessary to point out that the interparticle interactions are weak (not so strong such as in the SSG) and the energy for the single particle still can be defined[31], which is not the case of SSG. Regarding the magnetization, inter-particle interactions are involved in the model by adding the additional phenomenological temperature T^* to the real temperature in Langevin function:

$$M(H,T) = \int_0^\infty \mu L\left(\frac{\mu H}{k_B(T+T^*)}\right) f(\mu)d\mu \,. \qquad (2\text{-}7)$$

Following the Langevin function fitting procedure, the true function of mean magnetic moment, $f(\mu)$, can be obtained.

Let us point out how is the blocking temperature affected by the interparticle interaction. The increase of the T_B with increasing interaction strength is commonly observed in measurements of magnetization and has been theoretically proved in Dormann-Bessias-Fiorani model[32]. The reasons for shift of the blocking temperature up to the higher values are the dipolar interactions that enhance the effective energy barrier. However, it was also numerically shown for weak interactions (or strong anisotropy) that the T_B decreases with the increasing interaction strength; but for moderate-high interaction (or weak anisotropy) the T_B increases[13,33]. Regarding this contradiction, an increase of the apparent blocking temperature is clearly the case only for the strongly interacting nanoparticle samples[13].

Relaxation phenomena in systems with weak interactions

In case of system with weak interactions, we can modify the Arrhenius-Néel law by adding the term involving interactions; $T \rightarrow T\text{-}T_0$. Writing the relaxation time τ as $1/f$, the dependence of the applied alternating magnetic field frequency, f, on the temperature gives the *Vogel-Fulcher law*:

$$\ln f = \ln f_0 - \frac{E_A}{k_B (T - T_0)} \ , \qquad (2\text{-}8)$$

where f_0 is a constant from which the τ_0 can be calculated and T_0 is the Vogel-Fulcher temperature - a measure of inter-particle (cluster) interaction strength.

2.2.3 Super-spin glasses: strongly interacting nanoparticles systems

Dormann et al.[32] introduced as the first the collective phenomena in systems of nanoparticle, similar to those of the single spins (spin-glass behavior), and used the same formula to its description[34]. The (super)-spin glass can be described as a random, strongly interacting magnetic system of nanoparticles (superspins) characterized by a random cooperative freezing of the superspins at defined freezing temperature, T_f. Below the T_f, a highly irreversible, meta-stable frozen state appears without a typical magnetic long range ordering[24]. To simplify it – the blocking of the single particle is not independent in SSG systems any more. Interactions between particles are sufficiently strong not to obey the superparamagnetic model and the relaxation processes become strongly correlated[30]. The independent spins are built up into locally correlated units, called clusters that are able to interact with each other via dipole or even exchange interaction. The spins that are not involved in the clusters take part in the interactions between clusters. It has been suggested that mainly dipolar interactions are responsible for the glassy dynamics in densely packed nanoparticles[35].

System evolution at temperature

At high temperatures, $T > T_f$, superspins are in the SPM state. When the SSG is cooled down to the low temperature, $T < T_f$, the clusters are created, the ground state appears to be 'glassy', which means the system exhibits a metastable and extremely slow relaxation behaviour due to the strong dipolar interactions among the particles, which makes the dynamics dependent on the total age of the systems (so called aging effects)[36].

As the temperature reaches the T_f, the superspin fluctuations in the clusters slow down. At the T_f, the system is locked into one of the possible ground states and freezes.

Relaxations

Looking at the formula (2-4) (Arrhenius-Néel law) for spin glasses, the $\tau \sim 10^{-13}$ s is the fluctuation time of the atomic moment. For nanoparticles, τ can be assigned to the superparamagnetic relaxation time of a single particle of average size. Using the approximation such as in the weakly interacting systems, the Vogel-Fulcher expression, resulting values of relaxation times of superspin in SSG systems belong to the interval: $\tau_0 \sim 10^{-9} - 10^{-12}$ s (the same as for the SPM systems of nanoparticles)[24]. This approximation is not valid in SSG, because it is not enough to involve perturbation of strong inter-particle interactions in the same way as in the case of weakly interacting systems (SPM with interaction or SFM).

Relaxation times of superspins in (strongly coupled) granular systems are much longer than in case of SPMs and atomic spin glasses and another formula describing critical behavior near the glassy temperature, T_g, has to be used.

Above the T_g, it is possible to relate the equilibrium spin-spin correlation length ξ to a relaxation time τ through the relation[37]:

$$\tau_m = \tau_0 (T_m/T_g - 1)^{z\nu} , \qquad (2\text{-}9)$$

where T_m is the temperature maximum (maximum at ac susceptibility curve), T_g is the glassy temperature, ν is the correlation length exponent describing the divergence of ξ as T_g is approached from higher temperatures, and z is a dynamic critical exponent[38]. The values usually founded in literature valid for SSG systems are $z\nu = 5 - 11$[39,40], and the τ_0 is ranging from 10^{-5} up to 10^{-11} s [39].

The relaxation phenomena in all nanoparticle systems is summarised in Table 2.1.

Aging effects

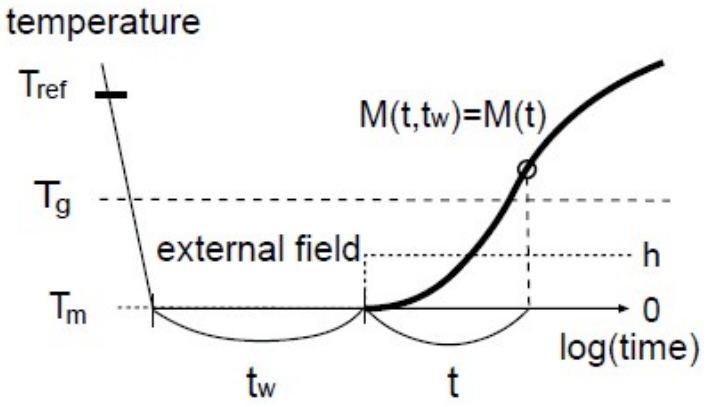

Fig. 2.1: Protocol of the ZFC relaxation experiment[13].

Aging effect is the term of the irreversibility in the temperature dependence of the magnetization; it is the synonym of revealing the so-called 'waiting time' dependence of the magnetization dynamics[41]. Studies of the aging effect are the elegant way how to distinguish between weakly and strongly correlated systems of nanoparticles (SPM, SPM-with-interaction and SFM versus SSG).

The ideal superparamagnet does not exhibit any aging effects - clearly speaking mean value of its magnetization measured at arbitrary temperature below the T_B is constant and independent on the waiting time. The reason is the short spin-spin (superspin-superspin) correlation lengths[36]. Unlike the ideal superparamagnets, SSG systems exhibit the relaxation of ZFC magnetization, which is logarithmic in time[41].

The aging effects are usually studied through the ZFC (zero-field-cooled) relaxation experiment. The measurement protocol is illustrated in Fig.2.1. At the beginning, the sample is cooled down to the measurement temperature T_m (under T_g in SSG) under zero field, after a waiting time, t_w, a small probing field, $\boldsymbol{h}$ is applied and the ZFC magnetization M(T) is recorded as a function of time[13].

Table 2.1: Relaxation phenomena in various nanoparticle systems.

	Interparticle interactions	origin	Relaxation phenomena	τ_0 (s)	aging effects
superparamagnet	none	none	$\tau_m = \tau_0 \exp\left(\frac{K_{eff}V}{k_B T}\right)$	10^{-9}-10^{-12}	none
superferromagnet	weak	exchange	$\tau_m = \tau_0 \exp\left(\frac{K_{eff}V}{k_B (T - T_0)}\right)$	10^{-9}-10^{-12}	none
SPM with interaction	weak	dipolar	$\tau_m = \tau_0 \exp\left(\frac{K_{eff}V}{k_B (T - T_0)}\right)$	10^{-9}-10^{-12}	none
Super-spin glass	strong	dipolar (exchange)	$\tau_m = \tau_0 (Tm/Tg-1)^{zv}$	10^{-5}-10^{-4}	yes
Super-spin-like glass	strong	dipolar (exchange)	$\tau_m = \tau_0 (Tm/Tg-1)^{zv}$	10^{-5}-10^{-4}	none

3 Magnetic Properties of Thin Films

3.1 Basic characteristic

3.1.1 Structural and magnetic properties

The thin films are defined as the layers of material whose thickness is small in comparison with other dimensions. These films could be also regarded as layers whose thickness is less than any characteristic length of electron (screening length, diffusion length, mean free path and others), or comparable to it. Also the physical properties are affected by the size effects or the quantum size effects in a limiting case, in which the film thickness is comparable to the de Broglie wavelength of electron, λ.[42]

Considering the internal structure of the layer, thin films can be divided into two main groups: continuous media such as epitaxial films (0.1-100 nm thick monocrystalline layers) and polycrystalline films (in which the layer is separated into many μm-sized crystallites) and granular films (composed of grains that could be considered as nanoparticles).

Similarly as in the bulk material and nanoparticles, one of the basically studied properties of the thin films is the direction of their total magnetization, given by the magnetic anisotropy energy.

In a term of magnetic anisotropy in thin films, two basic geometries are defined: films with *in-plane (parallel)* anisotropy and films with *out-of-plane* (*perpendicular)* anisotropy.

In *'planar'* films, the magnetization of the domains is parallel to the film plane and the anisotropy may be either uniaxial (there is one easy axis of magnetization) or biaxial (two easy axis). In *'perpendicular'* films, the magnetization in the domains is perpendicular to the film surface. Typical example of perpendicular films is the bubble memory carrier ('bubbles' are isolated cylindrical domains that can be used for magnetic storage applications) and perpendicular or magneto-optical storage media[43].

As was mentioned briefly in Chap. 1, the domains in bulk material, with opposite orientation of magnetization are separated by the boundaries called the domain walls. The same situation is set up in thin films, so the proper description of the two possible configurations of walls, *Bloch* and *Néel* walls, is given in this chapter. In the *Bloch* wall, magnetization rotates in the plane parallel to the plane of the wall; while in the *Néel* wall, magnetization rotates in the plane perpendicular to the plane of the wall[14].

Bloch wall width determines which type of anisotropy (and hence the domain alignment) evolves in the thin film. In-plane alignment of domains is typically the case

of soft magnetic films which thickness is comparable to the Bloch wall width; the out-of-plain anisotropy is observed in films which thickness is higher that the Bloch wall width. The typical alignment of domains and domain walls in planar and perpendicular film is demonstrated in Fig. 3.1. The domain width in planar thin films ranges typically up to hundreds of microns; however, domain width in perpendicular films could be 3 orders of magnitude smaller (Fig. 3.2).

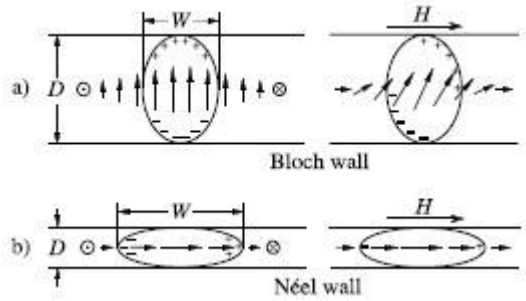

Fig. 3.1: Domain walls in a) perpendicular thick film, b) planar thin film[43].

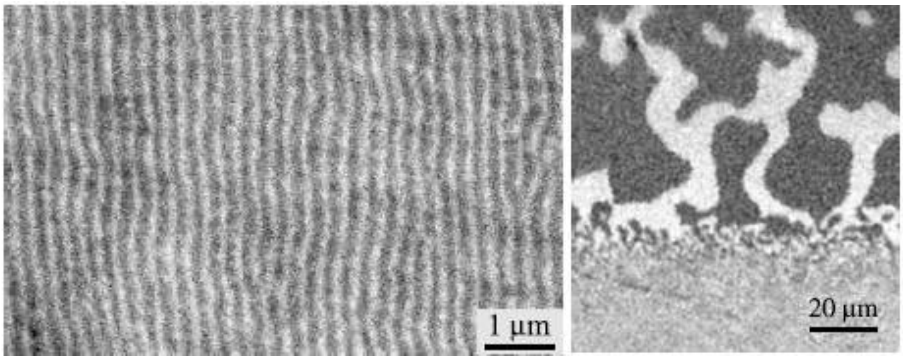

Fig. 3.2: Left: stripe domains in film with out-of plain anisotropy (permalloy, thickness 210 nm), right: domains in film with in-plain anisotropy (3 ML of Co film).[43] ML is the short-cut for the monolayer; a single layer of atoms of which the multi-layered films are composed.

3.1.2 Origin of direction of total magnetization

This part is based on the review by Poulopoulus and Baberchke[44] and gives introduction to the magnetic anisotropy in thin films.

As was already mentioned, the thin and thick film can be described, in view of their magnetic symmetry, in term of its internal energy arising from the domain structure, which is in general given by the film thickness. If the thickness of the film is smaller than the exchange interaction length (between two magnetic moments), ultra-thin films behave as a giant magnetic molecule and obey single domain description (see Stoner-Wohlfart model, Chap. 1). If the thickness overcame the exchange length, the direction of magnetization in thin films is given by the total anisotropy energy, which especially in thin films originates mainly from competition between two anisotropy energies: the magnetic anisotropy energy (MAE) and the shape anisotropy energy (SAE).

1) Magnetic anisotropy energy (MAE)

MAE in thin films is the term considering only intrinsic anisotropy, in which the inter-domains dipole-dipole interactions dependent on the shape are not involved. If the description in Chap. 1 is considered, MAE can be regarded as the magnetocrystalline anisotropy together with the anisotropy arising from the induced stress, strain and surface contributions.

MAE is numerically proportional to the area enclosed by magnetization curves measured along easy and hard axis of magnetization:

$$MAE \approx 1/2 \Delta M \Delta B . \qquad (3\text{-}1)$$

In ultra-thin films and multilayers, MAE is by order of magnitude higher than in the bulk ferromagnets. This increase is mainly caused by the reduction of spatial symmetry on the surface and by the lattice distortions due to the strain between the layer and the substrate or at the boundaries, between the magnetic and the non-magnetic layers (in case of multi-layers).

The surface and the volume energy contributions to the MAE are described in the same meaning such as in the bulk and nanoparticles (Chap. 1 and 2) by magnetic surface and volume anisotropy constants K_S and K_V, respectively. The volume anisotropy constant, K_V, is assumed to have bulk values in the middle of the film. K_S is thickness dependent and has two different contributions arising from two different film surfaces, interface with the substrate and the surface facing the air/vacuum.

2) Shape anisotropy energy (SAE)

It originates from long-range dipolar interactions between the magnetic moments and is strongly influenced by shape of the specimen ($2\pi M^2$). Depending on the film thickness, MAE is smaller or higher than the SAE. For thin films, the SAE dominates above the MAE so the easy axis of magnetization lies in plain. Otherwise, for thicker films, the MAE overcomes the SAE and easy axis of magnetization favours out-of-plain direction.

Spin reorientation transition

Magnetic anisotropy constants are temperature dependent quantities, so the final MAE should be calculated and presented at temperatures above the T_C (or T_B in case of granular nanoparticle films). Because of this temperature dependence, the spin reorientation transition from out-of-plain magnetization direction at low temperatures to in-plain magnetization at high temperatures sometimes occurs.

3.2 Co Thin Films

Many publications treat the structural and magnetic properties of Co-thin films because those with perpendicular magnetic anisotropy are good candidates for high density

storage media and those with the low coercivity are usable in fast GHz switching memories[45].

Kharmouche et al.[46] studied polycrystalline Co thin films evaporated on Si and glass, with thickness ranging from 50 to 195 nm.

It was shown that the magnetic properties closely depend on the film structure (crystallographic structure, texture, grain size and lattice constant). These granular cobalt films evaporated on Si(100) and glass surface developed the *hcp* structure with preferred orientation in the (0001) direction. The *in plain coercivity*, H_C, was constant for films with thickness less than 125 nm (0.23 and 0.25 mT for Si and glass substrates, respectively). Thicker samples exhibited sharp rise of H_C, its absolute values were independent on the substrate material.

The *out of plane coercivity*, H_C, was two orders of magnitude higher, and increased with the increasing grain size (so with increasing film thickness).

Magnetocrystalline anisotropy was supposed to be *uniaxial*; effective anisotropy uniaxial constant, K_{eff} decreased monotonously with increasing film thickness.

In the films evaporated on Si and glass with nominal thickness 173 and 195 nm, the stripe domain structure, typical for films with perpendicular anisotropy, was observed (Fig. 3.3). As expected, thinner films evaporated on both Si and glass substrates did not exhibit such a domain structure.

Authors also found out that thicker samples with the stripe domain structure had higher coercive fields (approximately 23 and 28 mT for glass and Si substrates, respectively, with the layer thickness $t_{C\ o}$= 173 nm; and 0.25 T for t_{Co} = 195 nm at Si substrate) in comparison with the thin films with thickness of Co layer less than 125 nm.

The very interesting feature was also observed in thin Co/glass films by the MFM method: the so-called cross-tie walls that are expected to be seen in films with in-plain magnetization. This effect was not noted in the corresponding Co/Si samples. The example of the cross-tie wall in 30 nm Fe(100) film is shown in Fig. 3.4.

Unambiguously, there was an effect of the substrate on the evolution of the domain structure, probably due to different growth mode of Co depending on the substrate nature.

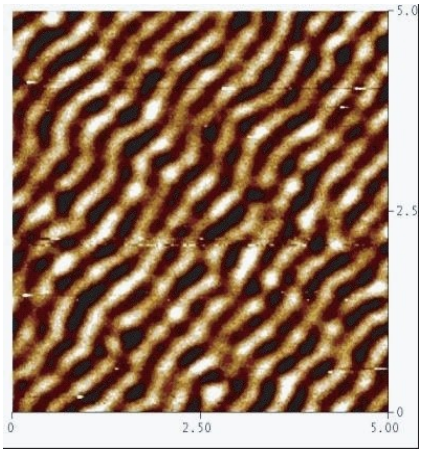

Fig. 3.3: Stripe domain structure of Co(193nm)/Si(100) thin film[46].

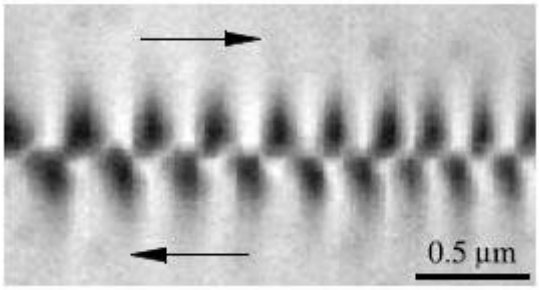

Fig. 3.4: High resolution MFM image of cross-tie wall in Fe(100) 30 nm film[43].

Li and Wang[47] studied the magnetic properties of ultra-thin granular Co films with thickness ranging from 1 to 19 monolayers (ML) on SiO_2/Si (111) surface. They observed the decrease of coercivity with the increasing film thickness from values of 1.4 ± 0.1 mT (3 ML) to 0.87 ± 0.1 mT (19 ML). This decrease of H_C was accompanied with the consequence of the decrease of the surface roughness, which reduced the surface macro- and micro-pinning effects. The decreasing surface roughness was supported by the decrease of Co electrical resistivity vs. Co film thickness. The electrical resistivity was measured in situ, roughness parameters were measured by the AFM.

Gubiotti et al.[48] studied the evaluation of perpendicular (out-of-plain) anisotropy in granular Co (0.9nm)/Au(5 nm) multilayers on number of bi-layer repetitions.

Authors claimed that perpendicular magnetic anisotropy in Co/Au multilayers was not affected only by the layer thickness, but crucially depended on interface quality (which was determined by method of preparation and annealing temperature). The detailed investigation of magnetic properties as a function of number of bi-layer repetition, N was done and spin reorientation transition from in-plane to out-of plane with increasing N was observed.

The evolution of perpendicular anisotropy with increasing number of multilayers was demonstrated by the MFM studies, in which the phase contrast was much higher for the films with N = 30 and 50 than for films with N = 10.

The calculated K_{eff} for each multilayer ranged from 1.65×10^{-1} J/m^3 for N = 10 to 1.98×10^{-1} J/m^3 (N = 50), positive values proved that the easy axis of magnetization was perpendicular to the film plane.

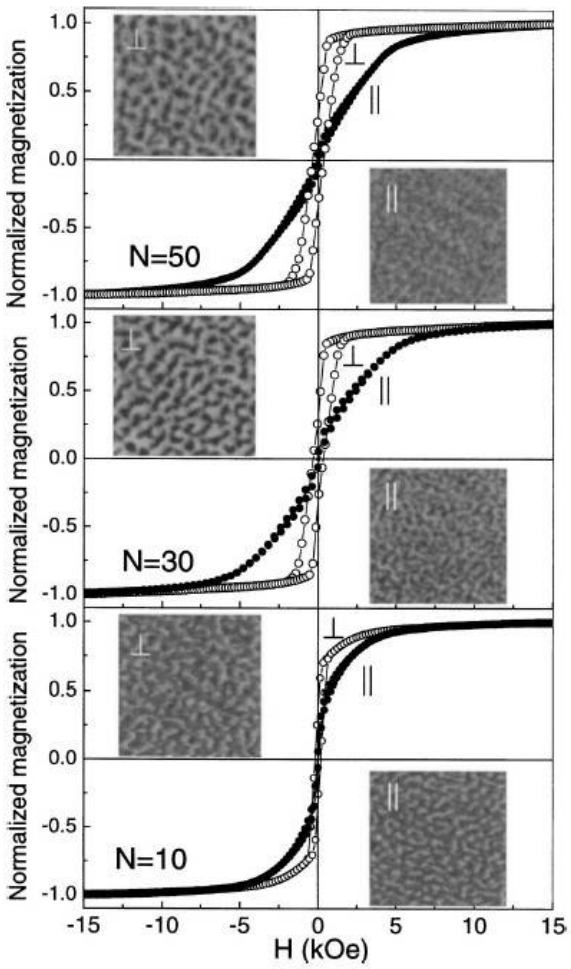

Fig. 3.5: Parallel and perpendicular normalized hysteresis loops for the Co/Au multilayers with different number of repetitions, *N*. MFM images were measured at remanence, after the application of the parallel and the perpendicular magnetic field of 1 T (scanning area is 5 mm× mm)[48].

4 X-ray reflectivity on thin films

The X-ray reflectivity is method based on diffusion of radiation in the proximity of total external reflection area and can be treated in general by principles and formulas well known from optics, only with little corrections. That's the reason why this chapter draw main information from review by Gibaud and Hazra[49] course-books of optics [50-51].

The X-ray reflectivity is not sensitive to the crystal structure of matter, only to electron density, because reflection occurs at boundaries with different indexes of refraction, n, described by formula:

$$n = 1 - \delta - i\beta , \tag{4-1}$$

where δ and β are constants connected with the scattering and absorption of material, respectively, through the formulas:

$$\delta = \frac{r_e}{2\pi}\lambda^2 \rho , \tag{4-2}$$

$$\beta = \frac{\lambda}{4\pi}\mu , \tag{4-3}$$

where r_e is radius of electron, λ wavelength, μ is the material absorption factor and ρ is the electron density.

For X rays, refractive index of the material, n is slightly smaller than unity; thus when passing from the air (n = 1) to reflecting material (n < 1), the beam is totally reflected for the angle of incidence which is smaller than the critical angle of incidence, α_c defined as:

$$\cos\alpha_c = n = 1 - \delta \quad \text{leading to the formula} \quad \alpha_c^{\,2} = 2\delta = \frac{r_e \lambda^2}{\pi}\rho . \tag{4-4, 4-5}$$

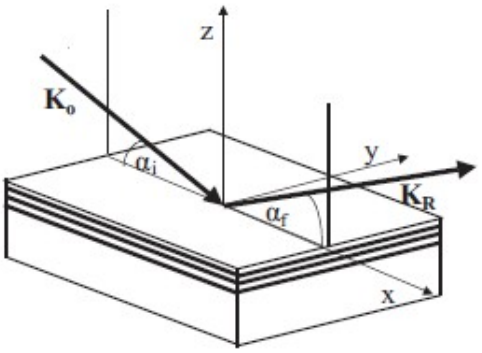

Fig. 4.1: Demonstration of the specular reflectivity[50].

4.1 X-ray Reflection by ideally flat surface

Not only do the light, but also X-rays are partially reflected and transmitted through the material. If the surface is flat, the radiation incoming from single direction is reflected into a single outgoing direction. This reflectivity is said to be the *specular* and is defined as:

$$R(\theta) = \frac{I(\theta)}{I_0}, \tag{4-6}$$

where $I(\theta)$ is the reflected intensity at angle of incidence θ and I_0 is incident intensity. If one wants to threat the dependence of reflected radiation intensity on the angle of incidence, the approximation solving the reflection of the electromagnetic wave at interface can be used, what leads to the classical Fresnel relationship which gives the reflection coefficients of amplitude for *s* and *p* polarization. The reflectivity is then the modulus square of this coefficient.

4.2 X-ray Reflection by rough surfaces

It is not possible to have atomically flat surface in real experiment, so the surface roughness, σ has to be considered when treating the material reflectivity measurements.

The effect of surface roughness is to reduce the reflectivity (written in the formula valid in $\boldsymbol{q}$-space) as:

$$R^{rough}(q_z) = R^{flat}(q_z)\exp(-q_{z,0}{}^2\sigma^2), \tag{4-7}$$

where q_z is the wave vector of reflected X-ray radiation and $q_{z,0}$ is the wave vector transfer in air. The connection between the real (angle of incidence) and $\boldsymbol{q}$-space is following:

$$\boldsymbol{q} = (0,0,q_z = 4\pi\sin\theta/\lambda)\ . \tag{4-8}$$

The reason to consider only the *z* component is the reflectivity only occurs for specular conditions (Fig. 4.1).

The typical shape of specular reflectivity curve, both for smooth and rough surface, respectively, is depicted in Fig. 4.2. For angles of incidence under the critical angle (and also appropriate *q* vectors), all radiation is reflected and the reflectivity is equal to 1 in ideal case. Above the α_c, radiation penetrates into the matter more and more with increasing angle of incidence.

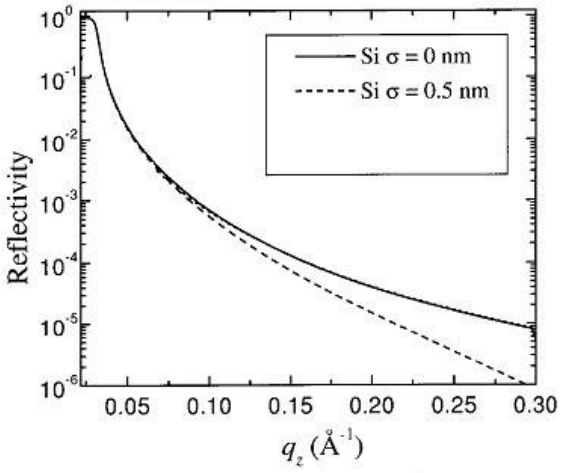

Fig. 4.2: Reflectivity curve for ideally flat (solid line) and rough (dotted line) surfaces[49].

4.3 X-ray reflection by thin film

The reflectivity curve of a thin film is modulated by oscillations called Bragg peaks which creation is a consequence of the interference in the film. If the thickness of the film deposited on substrate is *t,* the position of m^{th} interference Bragg maxima is given by equation which is an analogy with that for diffraction on plains in a single crystal:

$$2t\sqrt{\sin^2\alpha_m - \sin^2\alpha_c} = m\lambda\,. \qquad (4\text{-}9)$$

The solid curve in Fig. 4.3 represents the reflectivity at thin film with zero surface (σ_0) and film-substrate interface (σ_t) roughness. The influence of non-zero σ_0 and σ_t on reflectivity curve is also demonstrated.

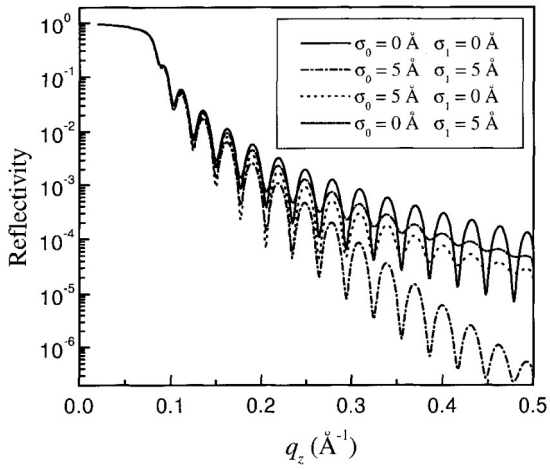

Fig. 4.3: The thin film reflectivity curves for different surface (σ_0) and film-substrate interface (σ_t) roughness, respectively[49].

4.4 X-ray reflection by planar multilayers

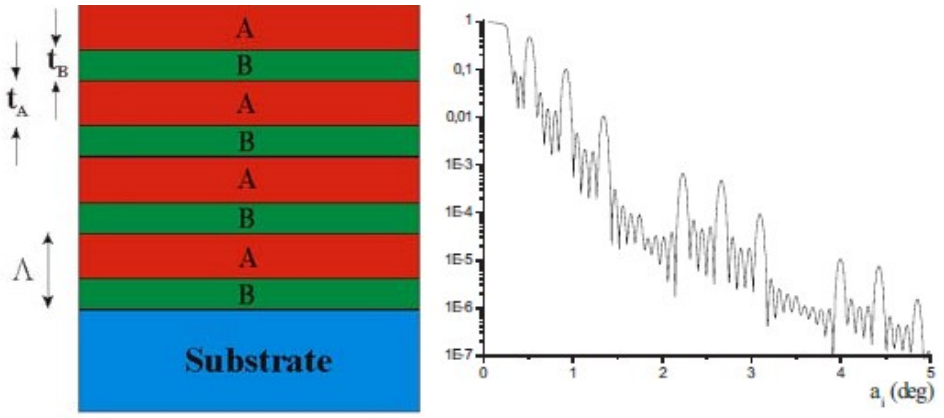

Fig. 4.4: Left: schematics of a multilayer; right: reflectivity curve from a multilayer[49].

The typical structure of planar multilayer is depicted in Fig. 4.4, where t_A and t_B is the thickness of layer A and B, respectively; period is labelled as Λ. In contrast to the single layer, the reflectivity curve of multilayer exhibits two types of oscillations:

1. Braggs peaks,

   which position is given by periodicity of the multilayer (Fig. 4.4). Regarding eq. (4-9), the distance between two Bragg peaks in q space is inversely proportional to the period of the multilayer.

2. Kissing fringes

   are the small oscillations between Bragg peaks, which periodicity is connected with the multilayer thickness. The distance between two fringes is inversely proportional to the thickness of the film. If the N is the number of repeated bi-layers, one should expect N-2 Kissing fringes between two Bragg peaks.

As was demonstrated at a single layer, the reflectivity curve is strongly influenced by roughness of the interface. Also the non-homogenity of adjacent layer structure (its electron density) has to be taken into account in multilayer reflectivity calculations. It means the Fresnel equation cannot be used directly and also the multiple reflections have to be involved.

5 Scanning probe microscopy

This chapter serves as an introduction to the scanning probe microscopy, describes both the technical problems and the capabilities of method to image as small objects as is possible. Because of this reason, a lot of information is drawn from the handbooks[52,53], manuals[54] and up-to date reviews.

5.1 History and basic characteristics

Scanning Probe Microscopy in general covers methods based on monitoring the sharp probe's interactions with the scanned surface. The variety of techniques is used to gain information not only about the surface topography, but also about surface mechanical properties (elasticity, friction, adhesion), magnetic domain imaging, conductivity and capacitance measurements, measurements of inter-molecular forces (force spectroscopy) and many others.

There are two basic modes of the SPM:

1) Scanning Tunnelling microscopy (STM), and
2) Atomic Force Microscopy (AFM).

1) Scanning Tunnelling Microscopy was developed in 1982 by Binning, Rohrer, Gerber and Weibel at IBM laboratories in Zurich, Switzerland. Principle of operation is based on the measuring the tunnelling current between the tip and the conductive sample (in high vacuum). Because the tip-sample tunnelling current exhibit exponential decrees with the tip-sample distance, this method allows reach vertical resolution less then 0.1 nm and lateral resolution less than 1nm, which is sufficient to define the position of a single atom[52].

2) AFM was developed in 1986 by Binning, Quate and Gerber. The tip placed on the edge of the soft cantilever is scanning across the sample surface and, the forces acting directly between the tip and samples are used to create appropriate contrast. Unlike STM, this method allows measurements of variety samples either in ambient atmosphere or liquid[52].

There are three primary modes of operation are summarised below.

1) Contact mode (tip is in the direct contact with the sample).
2) Non-contact mode (tip is oscillating in a distance, there is no contact with the sample)
3) Tapping mode (tip is oscillating and touching the surface during each oscillation).

5.2 Microscope - principles of operation

The principle of operation is based on raster scanning of sample surface with an appropriate probe. The probe mechanical reaction to the sample (caused by the long and short-range interactions acting between the probe and the sample) is being monitored and the image contrast proportional to this mechanical probe displacement (deflection, frequency, amplitude or phase) is created.

The AFM (with optical detection system) consist of the tree main parts, as listed bellow.

1) The optical head which senses the cantilever deflection.
2) Piezo tube scanner which controls the scanning motion of the sample mounted on it.
3) The base that support the scanner and head and includes cirquits for detection of the signal.

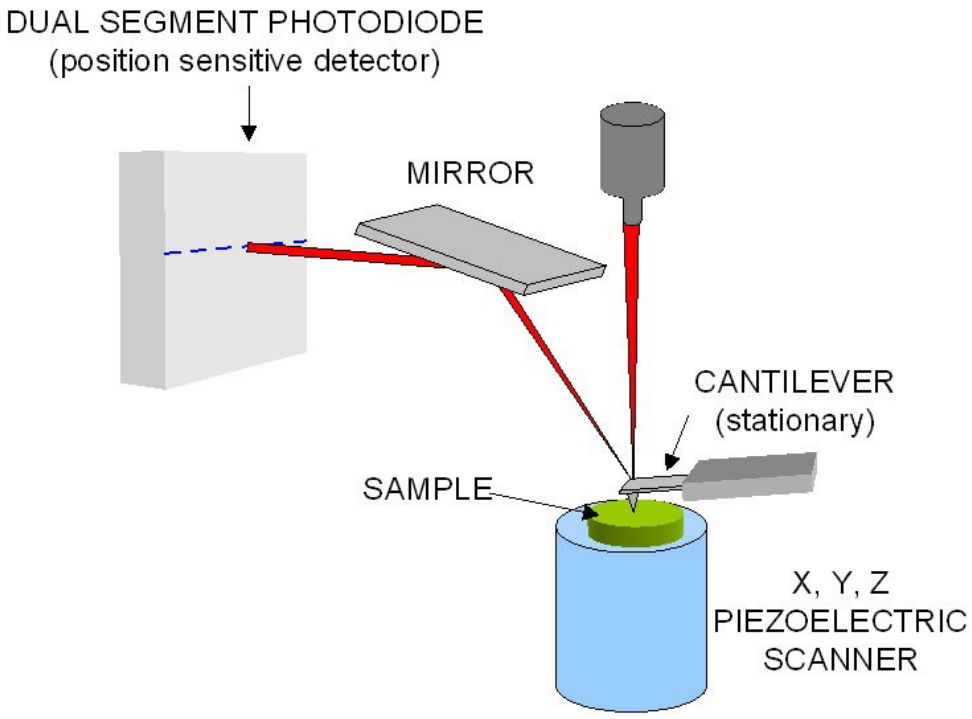

Fig. 5.1: Illustration of typical AFM hardware[54].

1) Optical head with deflection detection

The response of the probe to the sample during scanning, leading to the creation of proper image, is mediated by the optical lever detection system in the most of the commercially available microscopes. The principle of operation is following: the laser

shinning at the edge of the cantilever is refracted through the mirror to the photo-detector. While the cantilever is deflected due to the tip-sample interaction, this deflection changes the signal at the photo-detector and is measured directly. The detectors could be either two-segment or the four-segment. The advantage of the four-segment photo-detector is option of the direct friction measurements.

The detail of the optical head of the Multimode V microscope with four-segment photo-detector is depicted in Fig.5.2.

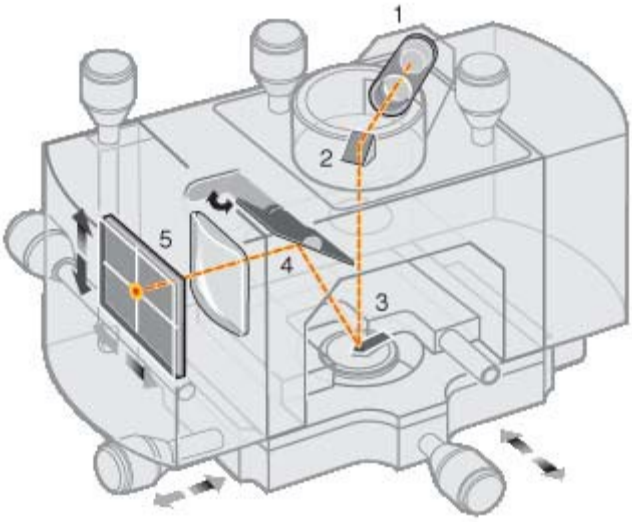

Fig.5.2: Multimode V optical head. Labels: 1. Laser. 2. Mirror. 3. Cantilever. 4. Tilt mirror. 5. Photo-detector.[54]

2) Piezoelectric scanners

Piezoelectric scanners are responsible for all the probe/sample movements during scanning. SPM scanners are made from such a piezoelectric material, which expands and contracts proportionally to an applied voltage. The scanner is constructed into the single tube from 3 independently operated piezo electrodes allowing the movements in X, Y, and Z direction and can manipulate with sample with extreme precision in three directions.

Because of differences in the material and dimension properties of each single piezoelectric element, each scanner replies differently to the applied voltage. The response, sensitivity (which decreases exponentially with time as the piezo is aging), is defined as the ratio of piezo-movement to piezo-applied-voltage and it is not linear with respect to the scan size. The movement in dependence on the applied voltage is not linear, either. The sensitivity is highest at the beginning and at the end of the scan line-this is displayed by the hysteresis between two scan directions (trace and retrace).

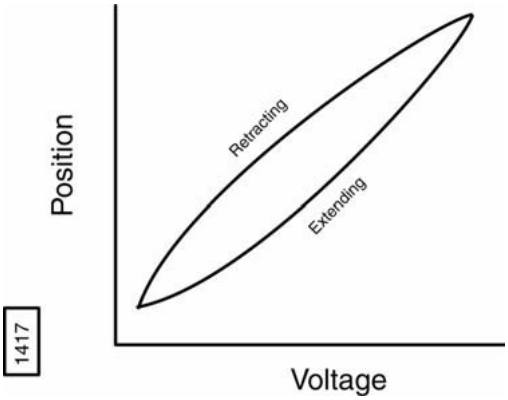

Fig.5.3**:** Piezo hysteresis- position change with applied voltage. [54]

Non-linearity and hysteresis can cause feature distortion in SPM images.

Non-linearity can be corrected by scanner calibration routine, when the non-linear voltage is applied to the scanner to obtain linear scan.

Hysteresis usually come into the play when the scan size is changing dramatically, the way to get rid of this effect is to wait until the scanner movement is stabilised.

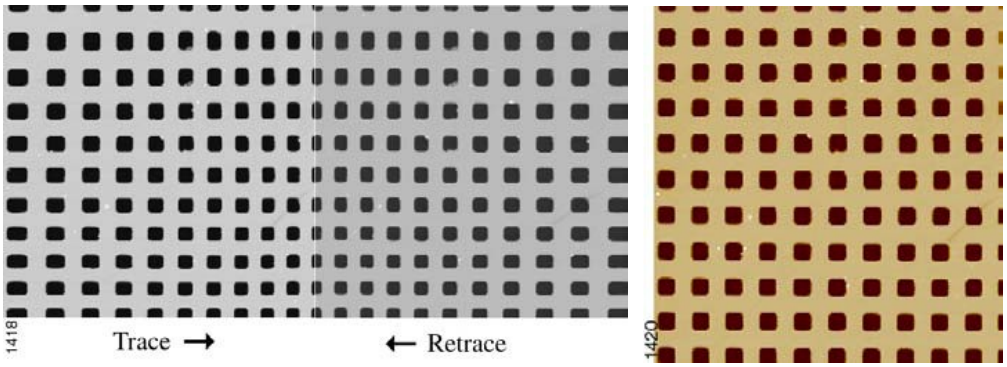

Fig.5.4**:** Left: non-linear scans taken in trace and retrace. Right: the same picture taken after calibration. [54]

5.3 Modes of operation

5.3.1 Static mode

Contact mode

In the contact mode, the tip attached to the end of a cantilever is scanning across the sample surface while the change in cantilever deflection *q*, $q=F/k$ (where F is the force acting on the tip and k is the spring constant) is being monitored with a split photodiode, capacitive or tunnelling detector[54]. The direct contact between the tip and the sample is mediated through the overlap of the atomic electronic orbitals at the edge of the tip and the sample surface. The tip experiences the weak repulsive force that causes the cantilever to deflect[52].

In this mode, the cantilever deflection is used as a feedback. The force acting between the tip and the sample remains constant during scanning by keeping the cantilever deflection constant moving the scanner in each (X,Y) data-point. The distance the scanner moves vertically at each (X,Y) data point is stored by the computer to form the topographic image of the sample surface.

Resolution at topographic images in vertical direction reach values of 0.1 nm (as low as 0.01 nm) and lateral resolution values of about 0.2 nm in commercially available AFMs. Forces in range from 10nN to 1 pN are measurable with displacement sensitivity of 0.01 nm[52].

Advantages/disadvantages: Scanning in contact mode allows scanning surfaces with high rates. Otherwise, lateral forces acting on the tip can distort the features at the surface and the combination of lateral and normal forces can lead to the sample damage mainly in case of soft polymeric or biological samples[54] .

5.3.2 Dynamic modes

Non- contact mode

In this mode the tip does not contact the sample surface directly, but oscillates above it. The cantilever oscillates slightly above the cantilever's resonance frequency with and amplitude of few nanometers (< 10nm) in order to obtain ac signal from the cantilever.

The cantilever resonance frequency is decreased by the Wan der Vaals forces acting between the tip and the sample (mainly in the distances of 1-10 nm), and other long-range forces that extend above the surface.

If we consider the oscillating tip as a linear harmonic oscillator, the shift of resonance frequency can be calculated as following[53]:

$$\Delta f \approx \frac{f}{2k}\frac{\partial F}{\partial x} \tag{5-1}$$

that highlight the fact that the force gradient can be directly measured. The more precious formula for calculating the resonance frequency shift gives

$$\Delta f = f_0\left(\sqrt{1+\frac{k_{\text{int}}^{\ eff}}{k_c}}-1\right), \tag{5-2}$$

where f_0 is the resonant frequency when the tip does not interact with the surface, $k_{\text{int}}^{\ eff}$ is the effective spring constant describing changes of the interaction between the tip and the surface over an oscillation period, and $\underline{k_c}$ is the cantilever spring constant[56].

To create the topographical image contrast, the feedback loop is maintaining either the amplitude or the frequency constant by moving it in the vertical direction at each (X,Y) data-point.

Advantages/disadvantages: Lower lateral resolution is limited by the tip-sample separation distance, slower scan speed results in the tip getting stuck, it is the only method to obtain "true atomic resolution" images.

Tapping mode

In the tapping mode the cantilever is vibrating at frequencies slightly bellow its own resonance frequency (70-100 kHz) with amplitude in range of 20-100 nm. During scanning, the tip slightly taps on the surface at the bottom of each cantilever swing. The oscillation amplitude is kept as a feedback; topographical image is created from the changes in vertical scanner positions such as in the non-contact mode[54].

Advantages/disadvantages: Scanning in TM leads to the high lateral resolution (1-5nm), the forces acting on the sample are lower than in the contact mode and less damage the samples. The main advantage is the reduction of the lateral forces. The speeds used for scanning are lower than in case of CM.

The illustration of both operating principle and the feedback loops are depicted in Fig. 5.5 - 7.

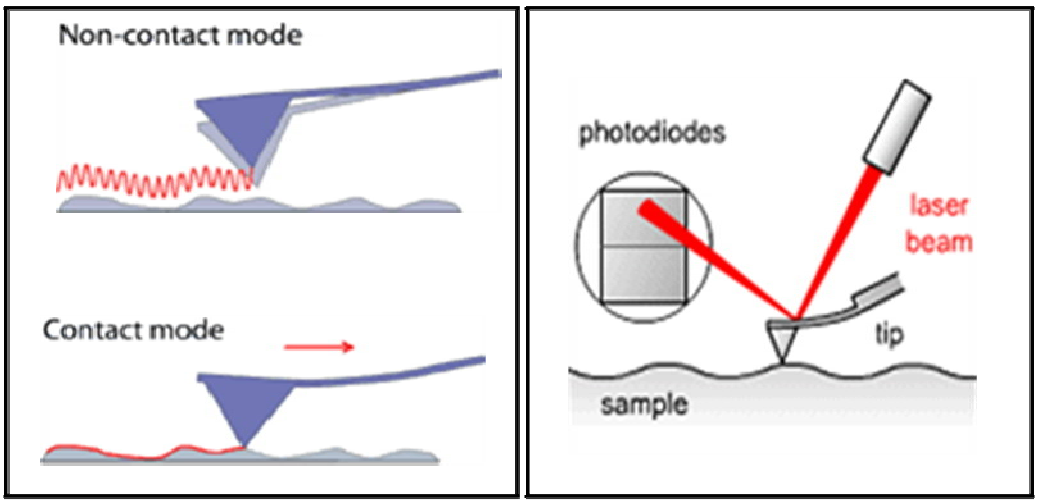

Fig. 5.5: Left: Probe-surface interaction in non-contact and contact mode. Right: The basic principle of the cantilever deflection detection. [54]

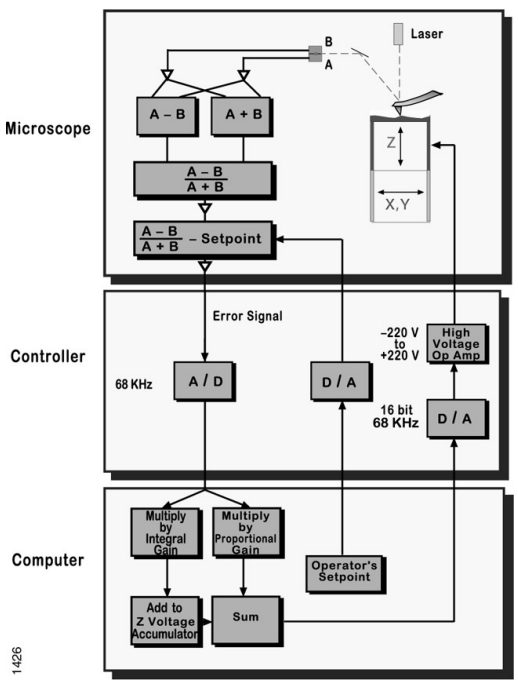

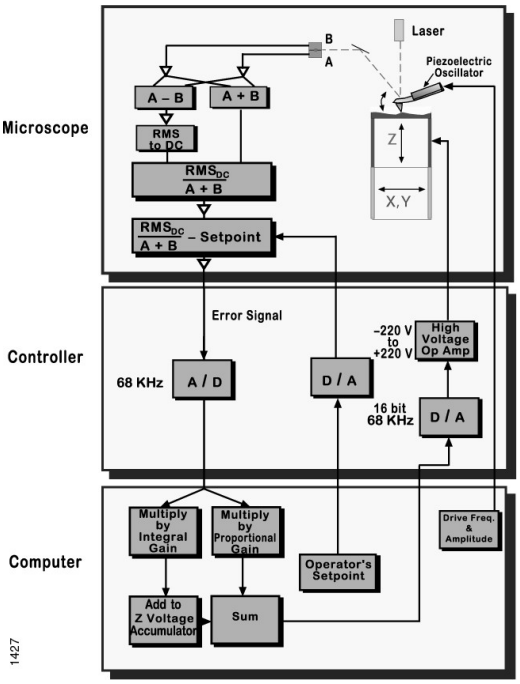

Fig. 5.6: Feedback loop-Contact Mode[54] **Fig. 5.7:** Feedback Loop – Tapping Mode[54]

5.4 Probes (Cantilevers and Tips)

5.4.1 Probes for Contact and Tapping Mode Imaging

The properties and dimensions of probes have an impeccable role in AFM resolution and determining the sensitivity. The most advanced cantilevers are made of silicon (TM) or silicon nitride (CM) using photolithographic techniques. The proper cantilever has to be chosen with regards to the mode of operation and material of the sample. Variety of probes are available on market (Veeco inc., Nanoprobes inc.), only the basic types for contact and non-contact mode together with the special high-resolution probes are presented here. Those used for Magnetic Force Microscopy are discussed in detail in Chap. 6.

The parameters that usually characterise probes are the spring constant k, resonant frequency f, and the size and shape parameters like cantilever length L and tip radius of curvature R. The value of spring constant determines in which media (air, liquid) and at which samples can be the probe used. It holds that the lower is the spring constant the 'softer' is the cantilever; thus the cantilevers with the low spring constants are usually used on soft samples.

Cantilevers for a contact mode imaging are usually short and thin, because they are required to be sufficiently soft to be deflected by very small forces and to have high resonant frequency to avoid vibrational instabilities.

The classical silicon nitride cantilevers that are mainly used for contact mode have spring constants ranging from 0.06 to 0.58 N/m (Fig. 5.8).

The silicon probes for *tapping mode* are much stiffer than the silicon nitride probes (spring constant 20-100 N/m), resulting in the large force constant and resonant frequencies.

Following figures show the basic probes for contact and tapping mode, together with its characteristic parameters. The tip and cantilever schematics with defined parameters used for probe description are in Fig.5.8.

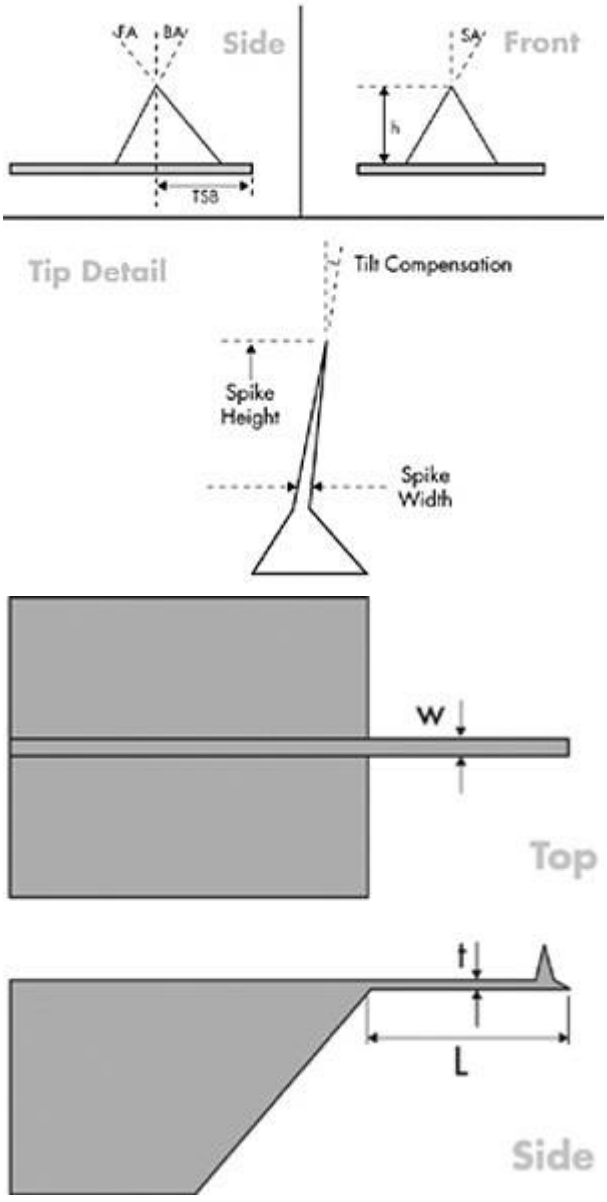

Fig. 5.8: Left: tip schematic. FA-front angle, BA-back angle, SA-side angle, h-tip height. Right: cantilever schematic. W: wide, t-thickness, L-length.[55]

Fig. 5.9: Schematics of the chip with four silicon nitride cantilevers, showing the spring constants (N/m).[55]

Fig. 5.10: Silicon nitride cantilevers with silicon tips, on a chip. Material: Silicon Nitride. Thickness (t): 0.55 - 0.65µm. Coated by Au.[55]

Fig. 5.11: Sharp silicon probe for the Tapping mode imaging. Cantilever properties: spring constant (k): 42N/m, resonance frequency (f_0): 320 kHz. No coatings. Material: 0.01 - 0.025 Ωcm Antimony (n) doped Si . Thickness (t): 3.5 - 4.5µm. [55]

Fig. 5.12: Sharp silicon tip for tapping mode in detail. Tip parameters: Tip Height (h): 10 - 15µm. Front Angle (FA): 25 ± 2.5°. Back Angle (BA): 15 ± 2.5°. Side Angle (SA): 22.5 ± 2.5°. Tip Radius (R): 8-10 nm[55.]

5.4.2 Special Probes

This category includes probes with ultra sharp tips for high resolution, probes with special tip coating for MFM and conductive-AFM, and modified probes for force spectroscopy experiments. Only the ultra-sharp probes are discussed in this chapter.

Sharp probes

Super sharp AFM probes provide enhanced resolution imaging. The typical tip radius is as small as 2nm and also the higher aspect ratio near the apex is great advantage. Super sharp probes are available for dynamic mode, force modulation mode and contact mode. Several types and materials of probes are available on a market.

Silicon probes

These probes are the cheapest and the most available option to capture images in higher resolution than with the classical silicon or silicon nitride tips. The tip radius of curvature is less than 5 nm, which also allow scan features down to the 5 nm size.

Fig. 5.14: Super sharp spike tip. The small spike is silicon tip processed for the first 200nm of the tip apex. Cantilever parameters: spring constant (k): 42N/m, resonant frequency (f_0): 320 kHz. Tip parameters: tip radius (R): 2-5nm. Tip Height (h): 10 - 15µm. Front Angle (FA): 25 ± 2.5°. Back Angle (BA): 15 ± 2.5°. Side Angle (SA): 22.5 ± 2.5° [55].

Carbon probes

This category includes pure solid carbon or diamond-like carbon probes that are the good compromise between super sharp silicon probes and the more sophisticated Carbon Nanotubes (CNTs) probes. Carbon probes are not designed for use in contact mode to prevent scratching the soft surface or damaging the tip. If there are many diamond wires at the tip, such as in the diamond-like carbon probes by Veeco company (Fig. 5.15), the longest one is automatically chosen to scan the surface. It makes the probe be able to be used for several times after breaking the scanning ‘wire’ because another one acts as the tip after next approach.

Fig. 5.15: Diamond-like carbon sharp tip (DLCS) by Veeco. Tip parameters are following: Tip Height (h): 15 - 20µm. Front Angle (FA): 15 ± 2°. Back Angle (BA): 15 ± 2°. Side Angle (SA): 15 ± 2°. Tip Radius (R): 1-5nm.[55]

CNTs probes

These probes use the single or double wall carbon nanotubes that are grown by Chemical Vapor Deposition (CVD) at the apex of classical silicon tip. CNT probes are designed for high resolution measurements in Tapping Mode or Non-Contact Mode operations in air or vacuum. Due to the flexibility and elasticity of the CNT, the forces applied to the sample surface are very low and self-limiting. This makes the CNT probe dedicated for the use on soft matter as well as on hard surfaces. Due to their elastic properties, single/double wall CNTs are not suitable for measuring high aspect ratio features like deep trenches or contact holes and should only be used by the experienced AFM user. The average diameters of the CNTs are between 1.2 (Single Wall CNTs) and 2.4 nm (Double Wall CNTs). The length of the CNT is between 50 and 750 nm[56].

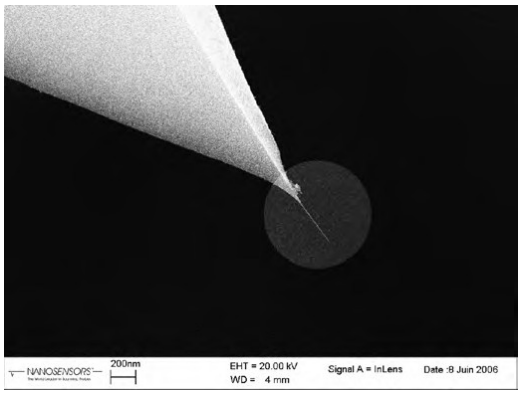

Fig. 5.16: CNT probe in detail (Nanosensors inc.).[57]

Magnetic and electrostatic force imaging

Cantilevers for MFM/EFM are made of antimony doped with bismuth; the tips are coated by ferromagnetic layer (Co, Cr). The thickness of the layer has the influence on

the probe sensitivity and determines the resolution of magnetic domain. Details are discussed in Chap. 6.

5.4.3 Effect of the tip shape to the quality of the image

In the Scanning Probe Microscopy, the image is the result of the tip-topography convolution. The two primary tip-features that directly affect the SPM image are the radius of curvature and the tip sidewall angles[54].

It is obvious that the smaller is the radius of curvature, the smaller features can be resolved. The effect of the sharp and the blunt tip on the image profile of the same features is demonstrated on Figs. 5.17 and 5.18.

One of the basic rules, when you are scanning the steep sidewalls on a sample surface, is that the steepness of the surface should be lower than the sidewall angle of the tip.

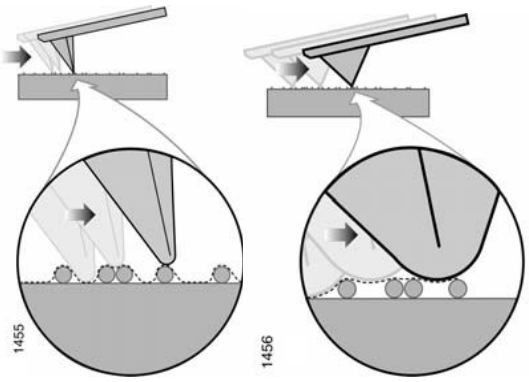

Fig. 5.17: Scanning the surface with sharp tip

Fig. 5.18: Scanning of the surface with blunt tip[54].

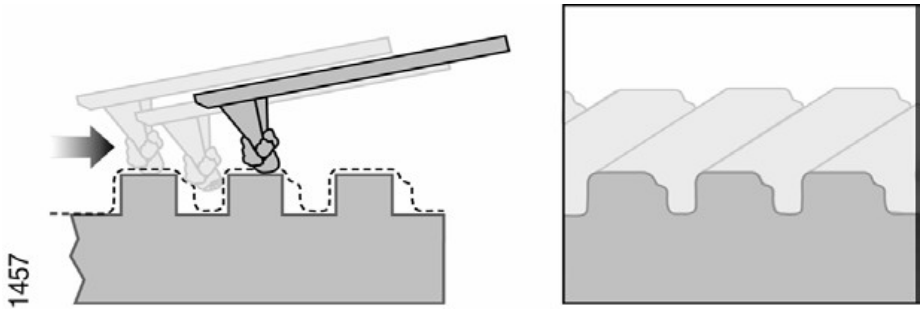

Fig. 5.19: Left: surface topography scanned with the dust stick on the tip. Right: resulting profile.[54]

5.5 Down to the Atomic Resolution

Resolution capability of SPM is an every-day experimental task and is discussed a lot in literature.

It is obvious that maximum lateral resolution of SPM is limited by the tip geometry, while the vertical resolution is given by the precision of the piezo scanner movement (if

the feedback is switch on) or the detection of change in cantilever deflection/frequency (if the feedback is switch off).

Even if the *vertical resolution* is primarily determined by the resolution of the scanner vertical movement, which is smaller than 1 Å, it is limited by the thermal noise of the deflection detection system[58]. For the optical lever system, the thermal noise of a free rectangular cantilever can be calculated like

$$\Delta z = \sqrt{\frac{4k_B T}{3k}}, \tag{5-3}$$

where the Δz is the thermal displacement in vertical direction, T is absolute temperature and k is the cantilever spring constant. At room temperature, Δz is equal to $0.074\text{nm/k}^{1/2}$.[58] The best commercial AFM can reach vertical resolution of 0.01 nm.

Lateral resolution is defined as the minimum detectable distance between two sharp spikes of different heights. This minimum detectable distance, d is related to the radius of curvature of the tip R and the vertical resolution Δz that is larger than the noise in z direction, assuming a small relative height Δh of the two spikes[59]:

$$d = \sqrt{2R}(\sqrt{\Delta z} + \sqrt{\Delta z + \Delta h}\,. \tag{5-4}$$

AFM is capable of atomic and subatomic resolution with the use of a sharp tip, but it was presented at the SPM workshop in Prague (Simultaneous STM/AFM measurements using tuning fork based sensors, FZU AV CR, 14.10-15.10. 2009) that also blunt tips (such as Ni(001) edge) at 'accurate' surface leads to creation of atomically resolved images.

When the two people scan the same surface with a different AFM, different probes and use different set of scanning parameters, final images may demonstrate significantly different resolution.

There exist various types of interactions that influence the final sample image, like long-range Van der Waals forces, capillary force, short range forces and electric double layer forces in a liquid, contamination effects, tip load effects and finally limitation of AFM as the local probe technique[58]. We will discuss the most of these interactions in following paragraphs.

5.5.1 Models of tip-sample interaction

At first let us discuss the basic options of tip-surface interactions through different continuum models. A continuum model treats the materials of the tip and sample as continuum solids. Various continuum models consider mechanical deformation or surface energy alone, or both[58].

The *Hertz model* considers elastic deformation of an elastic sphere, representing the AFM tip[60]. This model does not involve the adhesion, so the elastic deformation of probe recovers completely. In reality, there is additional force needed to overcome the adhesion (attractive force) of the tip to the surface.

Other, more realistic models use the previous one and takes into account attractive interactions of various types. The *JKR* model introduces the adhesion through the surface energy term[61]. The *DMT mode*l introduces a long-range attraction[62]; the *MD model* introduces a potential term; and finally the *Schwarz model*[63] (explicitly splits the surface force into surface energy and long-range components). Fig. 5.20 summarises all the various models.

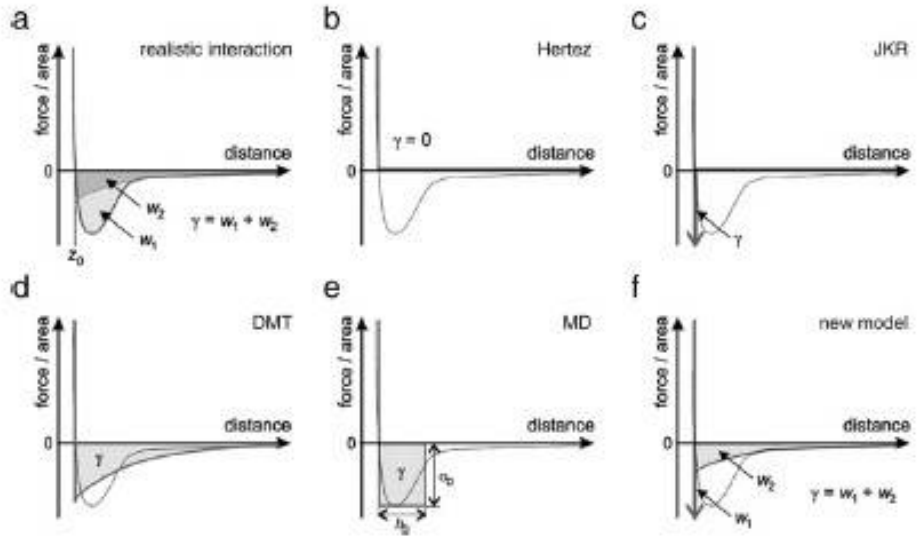

Fig. 5.20: Comparison of tip-sample interaction models. The shaded areas are the work of adhesion γ, separated into two parts w_1, long range component and w_2, short range component. (a) Realistic interaction, (b) Hertz model: attractive forces are included. (c) JKR model: surface energy is account for an adhesion. (d) DMT model: long-range interactions are added. (e) MD model: step function is introduced. (f) Schwarz model: combination of surface energy and the long-range forces is introduced[58].

Long-range van der Waals (vdW) forces

For the interactions of macroscopic objects, spherical tip with radius R next to a flat surface in a distance z, the vdW potential is given by equation[64]

$$V_{vdW} = -\frac{A_H R}{6z}, \qquad (5\text{-}5)$$

where the A_H is so called *Hamaker constant*, tabulated for different materials. For most solids and interactions across a vacuum, A_H is in the order of 1eV. The van der Waals force for spherical tips is thus proportional to $1/z^2$, while for pyramidal and conical tips the force is proportional to $1/z$[65]. Van der Waals forces are the major disturbance in the force microscopy, but Ohnesorge and Binning[66] have shown that these can be reduced by immersing the tip and the sample in a liquid[53]. Fig. 5.21 shows the calculated vdW forces versus tip-sample distance for different shape of tips.

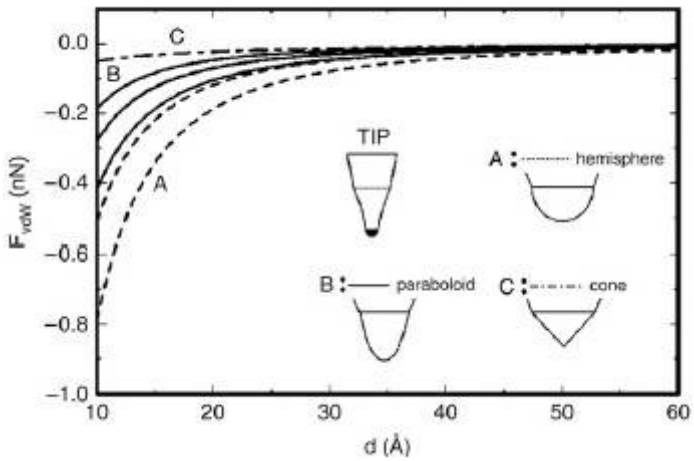

Fig. 5.21: Van der Waals force vs. tip-sample distance calculated for different tip shapes[56].

Capillary force

If the surface of the sample is exposed to the air, it is usually covered with water molecules in the form of clusters or film[67].

When the tip is approached to the surface covered with water film, water bridge (meniscus) is created between the tip and the surface. To detach the tip from the surface, the additional force has to be applied in comparison with no meniscus forms, so called capillary force. This force is usually more long-range than the vdW force under moderate humidity conditions[58].

Short-range forces

When the tip-sample distance is less than 1 nm, short-range forces become significant part of the total tip-sample interaction. These forces may originate from repulsion, chemical bonding, electrostatic and vdW interactions between atoms.

For static and dynamic AFM operating in ambient conditions, the tip-sample distance is far beyond the range of short-range forces because of the instability of soft cantilevers. Experimental use of short-range forces is restricted mostly to the ultra-high-vacuum environments, because the contributions from the long-range forces can be easily

identified[56]. Today, there is also the possibility of detection of the short-range forces in ambient atmosphere and high temperatures, more details are in the next chapter.

One of the short-range interactions, which act if the sample and the tip are both conductive, is the electrostatic force. For a spherical tip with radius R, separated from the surface by distance z, electrostatic force is given by equation[68]:

$$F_{electrostatic} = -\frac{\pi\varepsilon_0 R U^2}{z}. \tag{5-6}$$

The so-called chemical forces are more complicated, empirical models are the Morse potential:

$$V_{Morse} = -E_{bond}\left(2e^{-\kappa(z-\sigma)} - e^{-2\kappa(z-\sigma)}\right), \tag{5-7}$$

and Lenard-Jones potential:

$$V_{Lenard-Jones} = -E_{bond}\left(2\frac{\sigma^6}{z^6} - \frac{\sigma^{12}}{z^{12}}\right), \tag{5-8}$$

that describes the chemical bond between the tip and the sample with the bonding energy E_{bond} and equilibrium distance σ. The κ in the Morse potential is the interaction decay length[68].

Electrostatic forces in liquid

If the both the tip and the sample are immersed in a liquid, the capillary forces vanishes and the new type of forces, such as electrostatic, hydrophobic and steric forces, resp. come into the play. When the solid is put into the aqueous solution, the surface charges are developed and also the ions and the water molecules create a diffused layer in the proximity of the surface. Both together, surface charges and the diffused layer, create the *electrical double layer, EDL*[58].

When two surfaces (tip and the sample) approach each other in the solution, the electrostatic force is created due to the interaction of two electrical double layers. EDL forces may be long or short range, what depends on the concentration, ion type and the temperature of the solution, what allows control them by manipulating the pH and concentration of the buffer[69].

Tip load and pressure

For an AFM tip, the very end of the tip, the so-called tip apex, directly experiences the short-range force with the sample. Before the tip directly contacts the sample, the bulk of the tip, including the tip apex, experiences only long-range forces (e.g., the attractive vdW force and the capillary force) with the sample; however, after the tip is in stable

direct contact with the surface, the tip apex is pressed against the surface by the attractive (and stronger) long-range forces between the bulk tip and the sample[58].

One of the critical parameters for atomic resolution imaging, usually discussed in the literature, is the *tip load*, defined as the net normal force acting on the tip apex.

The tip pressure at the sample can be calculated as the tip load over the contact area between the tip and the sample. To have the idea how is the difference in pressures in case of the normal silica nitride tip with R = 50 nm, scanning the silica surface in contact mode and the sharp silica tip, these pressures are approximately 200 MPa and 5GPa, respectively[58,54]. At such a high tip pressures, the tip apex is not likely to deform elastically; thus, it will deform in-elastically to create a larger contact area until the tip pressure is reduced to a level at which the tip apex is stable[58].

Limitation of AFM-tip sample interactions

To achieve high-resolution topography with this technique, the tip needs to be in close proximity to the surface. There are several problems that complicate the scanning in high resolution, such as

a) jump into the contact due to the cantilever instability,

b) damage of the tip apex by the long-range interaction forces,

c) not monotonic increase of short range force with decreasing distance.

To achieve high resolution, all these problems have to be overcome somehow.

5.5.2 Atomic resolution

Atomic resolution of AFM is defined as the capability of AFM to resolve single or multiple atomic-scale entities separated by an atomic-scale distance[55]. The basic principles of achieving the atomic resolution and present fundamental results are summarized here.

Atomic resolution can be obtained using the cantilever, which spring constant is weaker than the equivalent spring between atoms and operating with the forces that are lower than the inter-atomic ones[52]. Inter-atomic spring constant between atoms with typical vibration frequencies of 10^{13} Hz or higher and atomic masses of approximately 10^{-25} kg are around 10 N/m[70]. Inter-atomic forces with one or several atoms in contact are in range of 20-100 pN; thus the atomic resolution can be achieved with a sharp tip on a flexible cantilever (spring constant about 1 N/m) at a net repulsive force of 100 pN or lower[53].

For the scanning in high lateral and vertical resolution at small forces (0.1 nN and lower), the cantilevers with extremely low spring constant (0.05-1 N/m) oscillating at high frequencies (10-100 kHz) are required[52].

Both the static (contact) and dynamic (non-contact) modes were used to scan in high/atomic resolution, but it was shown that only the frequency modulated AFM (FM-AFM) offers so called 'true atomic resolution'. Despite the first papers concerning the atomic resolution capability of AFM were operating in the contact mode[66], it was proved latter that the images were likely recorded at 'lattice resolution'[52, 58] instead of the atomic resolution.

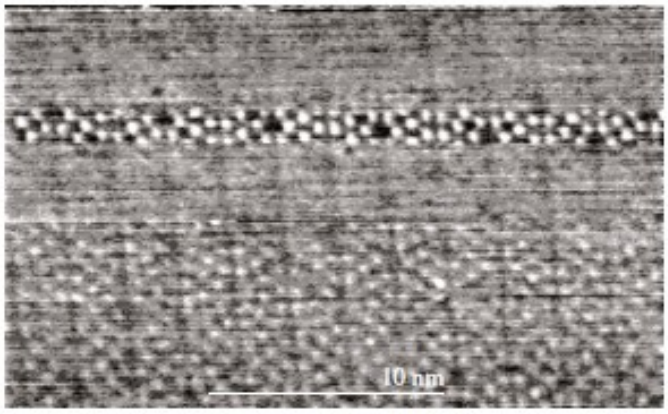

Fig. 5.22: The first image taken in true atomic resolution[68].

The first image in true atomic resolution was taken in 1994 by prof. Giessibl (Fig. 5.22) in frequency modulated non-contact AFM[68]. In FM-AFM, the feedback is switched off and only the changes in the cantilever oscillation frequency are measured. The initial experimental parameters that provided true atomic resolution of Si (111) surface were k=17 N/m, f=114 kHz, Q= 28000 (vacuum) and A=34 nm (surprisingly high value concerning the inter-atomic distances).

The images in true atomic resolution were usually taken in ultra high vacuum at low temperatures to avoid the thermal and mechanical fluctuations of the cantilever and to increase the noise/signal ratio. In the contact mode, the deflection is measured that is subject to noise especially at low frequencies (*1/f* noise)[52] and is given by eq. (5-4). On the contrary, vertical noise at FM-AFM is given by the ratio between the noise in the imaging signal and the slope of the image signal with respect to vertical displacement z:

$$\delta z = \frac{\delta \Delta f}{\frac{|\partial \Delta f|}{|\partial z|}} \quad . \tag{5-7}$$

The frequency noise, $\delta \Delta f$, is typically inversely proportional to the cantilever amplitude A[53].

In 1999, prof. Giessibl published theoretical prediction for values of parameters ideal for scanning in atomic resolution[71]. If the oscillation amplitude is of the same magnitude as the tip-sample correlation length, the signal/noise ratio increases 100 times. It means if the oscillation amplitude is in range of 0.1 nm, the required spring constant should be in order of 2000 N/m.

Today technologies allow obtaining atomic resolution not only in vacuum at low temperatures, but also at ambient atmosphere, in a liquid and at temperatures up to the 1083 K with small oscillation amplitude and extremely high frequencies (MHz) using special self-sensing cantilevers[72], (Fig. 5.23)

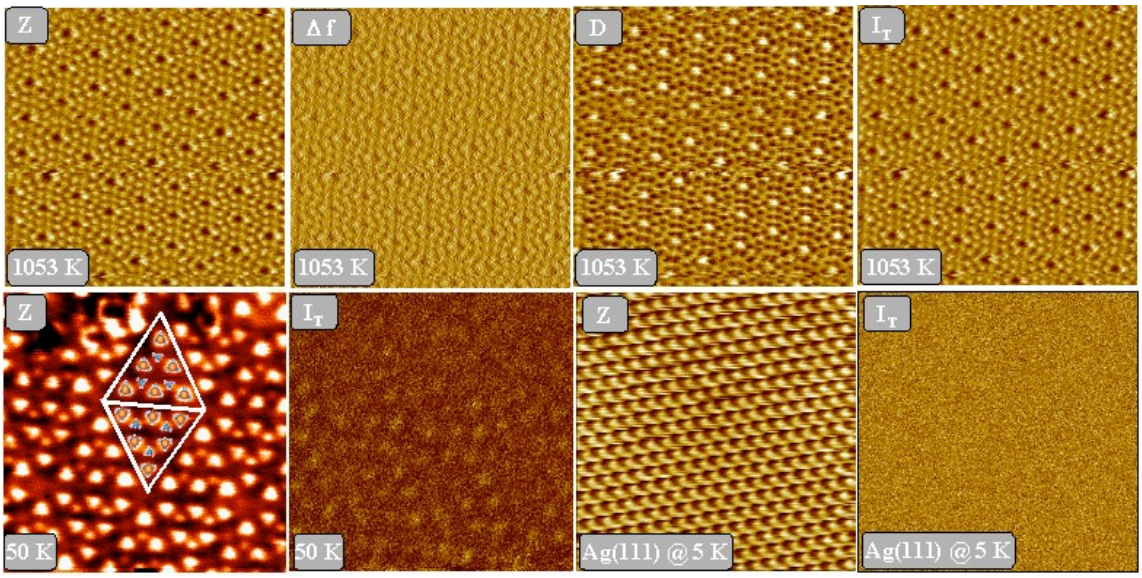

Fig. 5.23: Image of Si(111) surface in atomic resolution, taken with the q-plus scanner at 1053 K[72].

5.6 Image Artifacts

The basic problem when trying to recognize if the features on the images are real or not is to identify the possible image artefacts and to diminish them.

The artefacts can be classed into the three main categories:

1) ***Tip effects***- the various effects that can occur due to the interaction of the tip with the sample surface

   a) *Dirty (contamined) tips*

   b) *Blunt tips* – if the tip becomes worn out, the scanned features may have all the same shape. The reason is that the tip is not imaging the features on the surface but the features are imaging the tip itself (Fig. 5.24)

   c) *Double/multiple tip*- leads to the multiple images of the features on the surface, like in Fig. 5.25. The double tips are the most common.

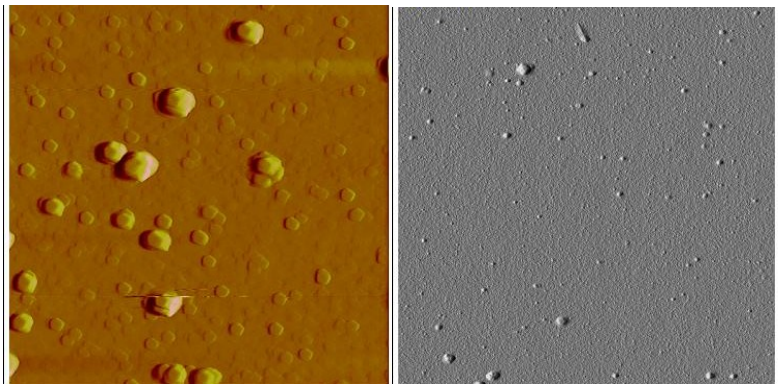

Fig. 5.24: Left: Surface scanned with the blunt tip. Right: Real surface scanned with the sharp tip (images were captured in our Laboratory at Co/SiO_2 thin films)

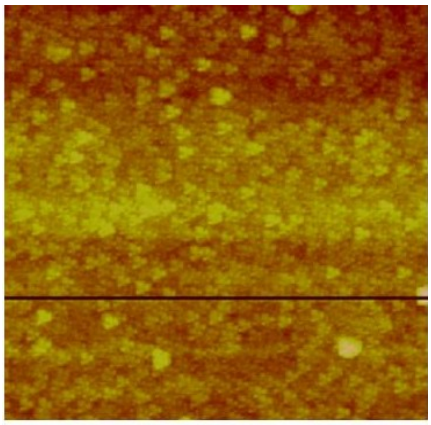

Fig. 5.25: Triple tip: features are imaged three times. Image was obtained in our laboratory at FeCoAlN thin film.

2) ***Scanner artefacts***- effects due to the peculiarities of the piezo scanner

a) Piezo Creep and Bow-leads to the distortion in the image

Creep is the drift of the piezo-displacement after a DC (dc?) offset voltage is applied to the piezo. This occurs with large changes in X and Y offsets (předtím bylo malé xy…), when the scanner travels over the scanning area. The piezo movement is divided into the two phases, when the scanner is moving fast near the desire position and then, during the scanning, the slow movement directly to the desired position follows-creep is the result of this slow movement[50].

Bow

Mechanical properties of the piezo scanner leads to its movement not on the lever but on the sphere. Scanning the large images, this second or third order of curvature captured in the image can be restored fitting the data to the sphere.

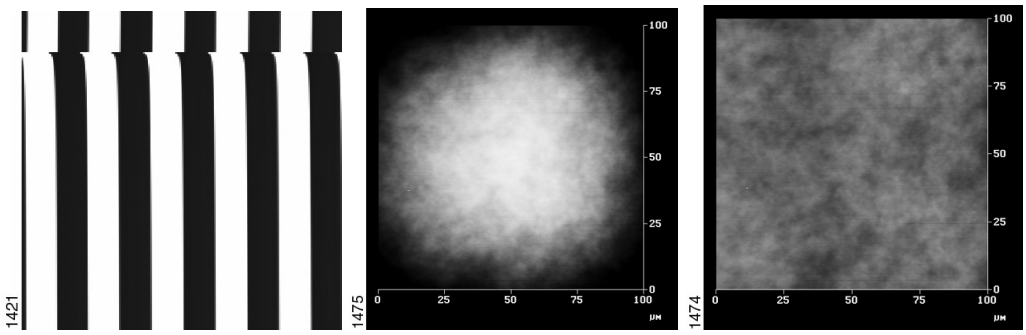

Fig. 5.26: Left: Creep. Middle: 2nd order bow. Right: flattened 2nd order bow (Veeco inc.).[54]

Piezo hysteresis – elongation of the features in the same direction

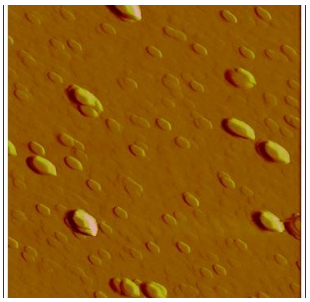

Fig. 5.27: Piezo hysteresis-features are elongated in the south-west direction (images were captured in our Laboratory at Co/SiO_2 thin films).

3) **Another effects**

a) *High resonance frequency* – in TM, when operating at high frequency side of the resonance peak, the rings appears around raised features (looks like surrounded by water). Decrease of the drive frequency eliminates the artefact.

b) *Sample drift* – causes distortion in the image.

c) *Laser interference patt*erns – leads to the stripes on the image.

d) *Flying tip*- stripes in the direction opposite to the cantilever movement, caused by the non-adequate feedback.

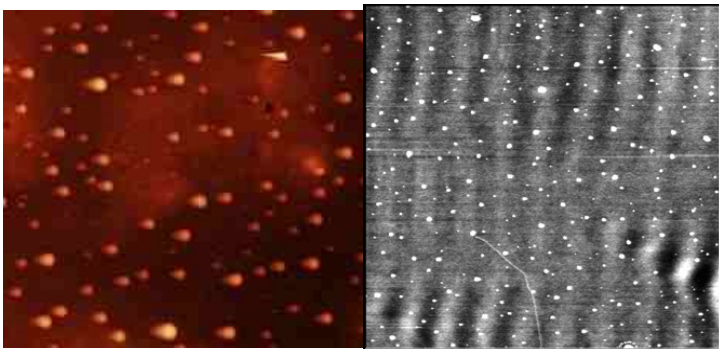

Fig. 5.28: Flying tip[54]

Fig.5.29: Laser interference pattern[54]

6 Magnetic force microscopy (MFM)

The magnetic force microscopy is the method derived from the Atomic Force Microscopy, widely used for visualization of magnetic domains. The method is based on the direct measurements of the tip-sample long- range magneto-static interactions, usually acting on the scale up to 100 nm. The main advantage of MFM against STM and AFM is the high sensitivity to the electronic properties of the surface[73].

6.1 The principle of capturing the data

The tip is passing the captured line two times. During the first pass, tip is scanning the surface like in classical Tapping Mode and the surface topography is obtained. In the second pass magnetized tip (could be consider as the magnetic dipole pointing in vertical direction) is kept in a constant distance from the surface (usually 10-100 nm), where ideally only the long-range magneto-static forces contribute. Depending on the domain's magnetization directions, the tip is attracted or repealed from the surface what leads to the creation of the image phase contrast. Repulsion between the tip and sample generates positive contrast and attraction the negative contrast. The principle of creating the image contrast is depicted in Fig. 6.1.

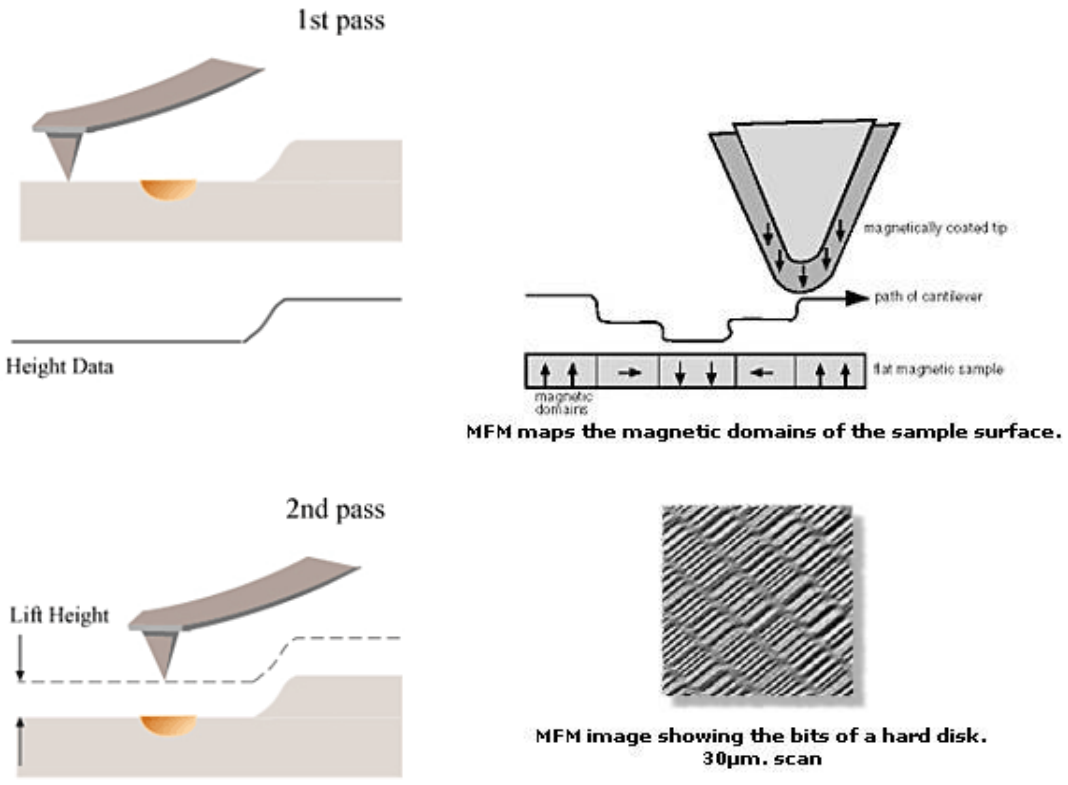

Fig. 6.1: Left: Principle of capturing the data. Right: creation of the contrast depending on the tip and the domain's magnetic moment orientation, image of hard disk (Veeco inc.).[54]

6.2 History

The most works using the method of MFM were concentrated on magnetic domain imaging in thin films of $La_{1-x}Ca_xMnO_3$[74-76].

One of the representative publication at these films was done by *Liebmann et al.*[74], in which the domain evaluation along the major hysteresis loop on $LaAlO_3$ thin film with induced out-of plain magnetization was captured (Fig. 6.2).

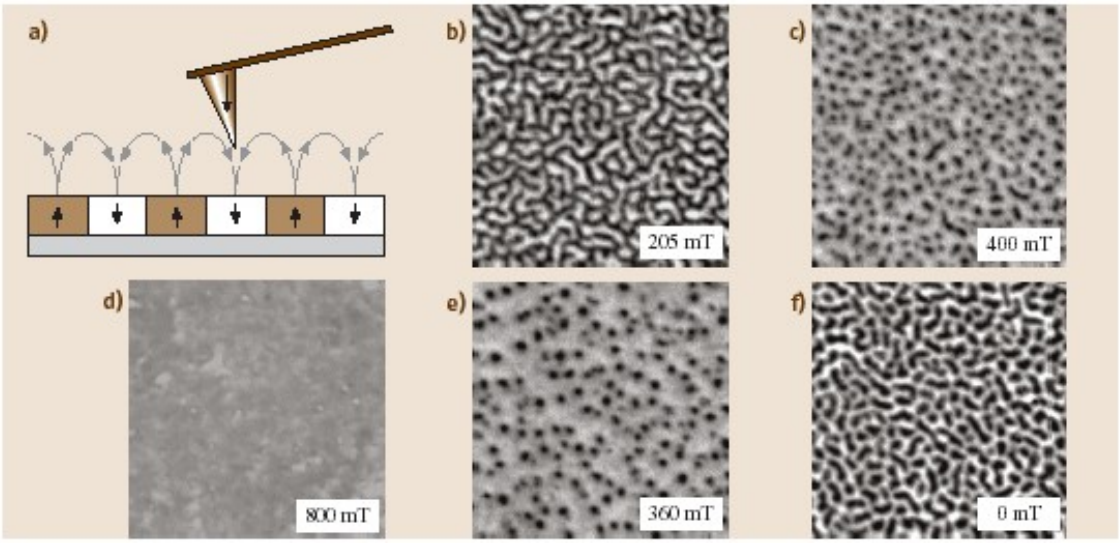

Fig. 6.2: Domain pattern evolution along the major hysteresis loop (from zero field to saturation and back to zero field). (a) Principle of MFM operation, (b)-(f) field dependent domain structure of a ferromagnetic thin film recorded at 5.2 K (FM-MFM). Sample was the $La_{0.7}Ca_{0.3}MnO_3/LaAlO_3$ system with substrate induced out-of-plane anisotropy; bright and dark areas correspond to the attractive and repulsive magnetostatic interaction.[74]

Also a lot of low-temperature MFM experiments have been performed, mainly on superconductors[77,78]. Imaging of vortices simply exhibited the dependence of the MFM[79] phase contrast on the scanned feature's magnetic moments orientation (Fig. 6.3).

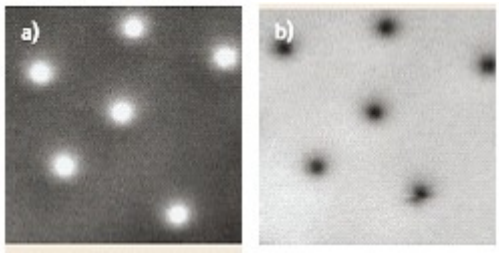

Fig. 6.3: MFM contrast reversal with the change of the magnetization direction. Vortices in niobium thin film were imaged: a) after field cooled at 0.5 mT and b) after field cooled in -0.5 mT.[79]

The results from recent years, concerning the imaging of magnetic nanoparticles, are discussed at the end of this chapter.

Even if the number of publications focused on the Magnetic Force Microscopy is growing so far, this method is still not very common and the limits of magnetic moment detection with respect to the instrumental parameters as well as the perturbations arising in another sources of long-range interaction (such as van der Waals forces) are widely discussed. As a result, this field seems to be still open to new development of experimental methods leading to the true imaging of magnetic structures in variety of materials.

Magnetic Exchange Force microscopy

This method is based on the detection of short-range magnetic interactions and allows not only obtain atomically resolved images of the sample surface, but also it is sensitive to the direction of atomic magnetic moments.

In the system of magnetic tip and the sample, the interaction detected by NC-AFM is composed of the long-range magneto-static interaction and the short-range exchange interaction. The short-range interaction energy depends on the electron spin states of the atoms on the tip's apex and the sample surface[73]. Energy difference between the spin alignment is referred as the exchange interaction energy and creates the magnetic contrast on atomic scale.

Huge number of works is dealing with the experimental and theoretical studies of antiferromagnetic NiO(001) surface[80-84], but one of the most impressive results in this area from recent years, concerning the magnetically sensitive atomic resolution imaging, have been done by *Kaiser et al*.[85]

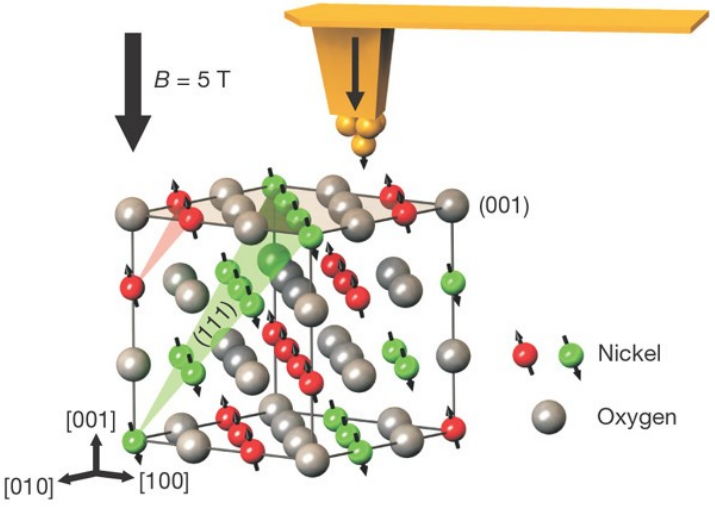

Fig. 6.4: Schematic of experiment: The magnetic tip was aligned in external magnetic field to scan the moments on Ni(001) surface.[85]

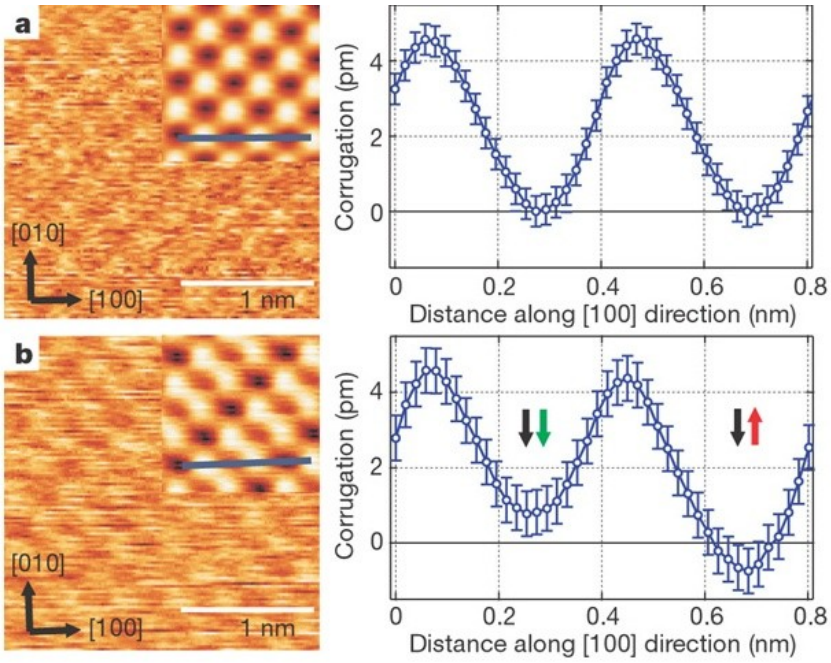

Fig. 6.5: (a) Chemical contrast obtained at Ni(001) surface (b) magnetic contrast at Ni(001) surface. The black arrows indicate the position of Ni atomic centres at chemical contrast image cross-section, the green and red ones indicates the positions of Ni atoms with spins pointing down and up, respectively.[85]

In Kaiser's experiment, NiO(001) surface was scanned in small external magnetic field (necessary to to align the magnetic polarization at the tip apex to maximize the exchange interactions with surface spins) with a ferromagnetic tip in frequency modulated non-contact mode, keeping the tip-sample distance less than 0.5 nm. The atomic resolution of the surface with differently oriented magnetic moments has been obtained. Fig. 6.5 (a) and (b) show the chemical and magnetic contrast, respectively. The bright spots belong to the oxygen, the dark one to the nickel. The less and more dark spots at magnetic-contrast image (b) indicate the Ni atoms with the magnetic moments pointing up or down. It is nice example how to distinguish the direction of atomic spin.

6.3 Probe-domain resolution issue

For visualisation of magnetic domains by Scanning Probe Microscopy, different ferromagnetic probes are offered. The measurement performance of MFM is the compromise between the sensitivity, resolution and sample disturbance. High sensitivity to magnetic signal requires high magnetic moment of the tip; however, it may disturb sample magnetic domain structure. Usually the lateral resolution drops with increasing magnetic moment of the tip. If the high lateral resolution is required, sharp tips with high aspect ratio and the thin magnetic coating are needed, but the sensitivity is decreased by lowering the tip magnetic moment arising from the thin coating. Magnetic domains of low coercivity samples can be “wiped out” by hard magnetic tips, domains of such a sample can be visualized only by the low coercivity probes. Otherwise, the

low coercivity probes may change their magnetization direction under the influence the sample with higher coercivity.

To obtain optimal results in magnetic domain visualization, one has to choose properties of magnetic tip carefully in accordance with the material under investigation. The value of maximum resolution of single domain with commercial tips is around 20 nm. Fig. 6.6 demonstrates the comparison of lateral resolution of magnetic domains scanned with different MFM tips. It is obvious from this picture that the super-sharp tip enables to visualize features with lateral resolution less than 32 nm.

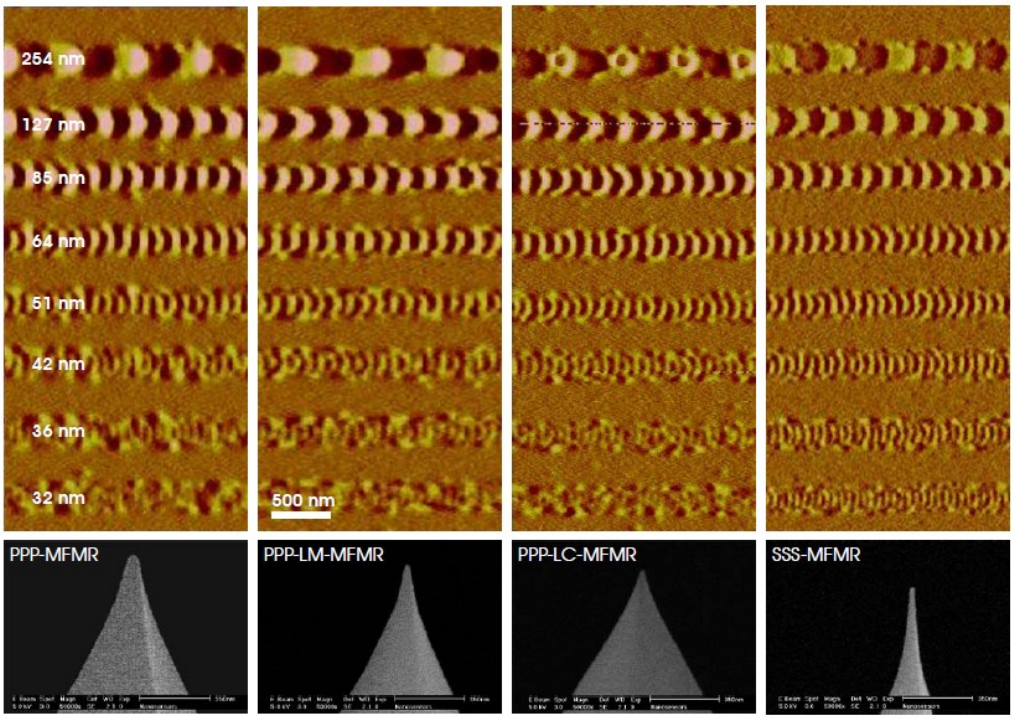

Fig. 6.6: From the left: classical magnetic tip (H_C 300 Oe, M_r 300emu/cm^3, M 10^{-13} emu, radius of curvature (r) <50nm, resolution (res) >50nm), tip with low magnetization (H_C 250 Oe, M_r 150 emu/cm^3, M 0.5 10^{-13} emu, r <30nm, res >35nm), low coercivity tip (H_C 0.75 Oe, M_r 225 emu/cm^3, M 0.75 10^{-13} emu, r<30nm, res > 35 nm) and super-sharp tip (H_C 125 Oe, M_r 80 emu/cm^3, M 0.25 10^{-13} emu, r < 15nm, res > 25 nm).[57]

6.4 Imaging of Nanoparticles

Imaging of superparamagnetic nanoparticles was told to be the challenge and only few researcher teams are working in this area so far; however, MFM was demonstrated to be suitable enough for visualisation of magnetic islands and quantum dots[86,87].

In 2008, *Agarwal et al.*[87] demonstrated the ability to detect, localize and directly calculate magnetic moment of a single magnetic nanoparticle. They claimed that the capability of MFM to detect a signal from nanoscale superparamagnetic particles has not been fully explored[89]. There have been some reports on the possible uses of MFM for detection of such particles occurring naturally in biological systems, that include detection of iron compounds in neurological disorders[90], magnetic domains in

magnetotactic bacteria[91], and iron deposits in Hepatitis B-diseased livers[92]. Limited studies also exist on localizing and detecting magnetic nanoparticles in vitro[93] or in cell-based systems[94], but the systematic and quantitative study of the applicability of MFM for characterizing superparamagnetic nanoparticles (SPNs) in ambient air is still lacking.

Agarwal et al. used magnetite nanoparticles in their experiments, the size of magnetite core of individual nanoparticle was estimated to 10 nm with appropriate magnetic moment 2.5×10^{-19} Am^2.

The MFM phase images of nanoparticles showed the contrast only in presence of the external magnetic field and for the lift heights higher than 20 nm. When the magnetic field was shielded, the contrast obtained with magnetic tip was negligible. Testing scans with non-magnetic tip failed in lift heights higher than 10 nm, what affirms that the contrast is mainly created by the long-range magnetostatic forces and the perturbation from vdW forces is negligible. The numerical simulation of probe-tip agreed with the experiment.

The sample was simulated as the single nanoparticle with diameter d and magnetic moment μ_s, the probe magnet was considered as uniformly magnetized hollow shell with saturated magnetization M_s, outer and inner radius of magnetic coating, R (typically 70 nm) and R_1 (typically 10 nm). The separation distance, s, is the sum of the lift scan height and the amplitude of oscillation (taken to be 10 nm). The phase shift φ resulting from the dipolar probe-sample interaction can be expressed as:

$$\delta\varphi = \frac{\mu_0}{4\pi} \frac{12\pi Q}{k(\frac{d}{2} + R + c + s)^5} m_p m_s \frac{180}{\pi}, \qquad (6\text{-}1)$$

where k is the spring constant of the MFM cantilever, Q is its quality factor, μ_0 is the permeability of a vacuum, and m_p is the probe magnetic moment, given as:

$$m_p = \frac{4}{3}\pi(R^3 - R_1^{\,3})M_s . \qquad (6\text{-}2)$$

The detectability of the contrast arising from the magnetic nanoparticle was also proved by magnetizing the sample in plain, leading to the opposite contrast depending on the external magnetic field direction. Some of the particles detectable on AFM did not shown any MFM phase contrast, suggesting these particles have nonmagnetic nature.

Authors showed that the visualized objects were not the single nanoparticles themselves, but the whole aggregates; the lift scan height ideal for detection of such objects seemed to be 20-40 nm. In lower lift scan heights the contribution from additional tip-sample interactions (like Van der Waals or electrostatic forces) may contribute to the resulting phase shift.

Mironov et al.[95] simulated the contrast induced by low-coercitive ferromagnetic and superparamagnetic nanoparticles and checked their theoretical results experimentally. The calculations were performed in dipole-dipole approximation; resulting magnetic contrast displayed the same symmetry as that for the contrast caused by Van der Waals forces in Taping Mode imaging. The interesting and practical result of this publication is the formula for estimation the external magnetic field H^* essential for stabilization of the nanoparticle's magnetic moment (stabilization to the state in which its magnetic moment is detectable and creates the appropriate contrast):

$$H^* = \alpha^* \frac{kT}{M_p V_p}, \tag{6-3}$$

where α^* is the argument of Langevin function and M_pV_p is the particle magnetic moment in saturation. Based on this criterion; it is possible to estimate scanning height parameter that will realize effective MFM contrast formation for superparamagnetic particle. Field created by the MFM probe, H_t, should be higher than the stabilizing field H^* and leads to the following criteria for estimation of scanning height parameter, h:

$$\frac{d_p + d_t}{2} < h < d_p d_t \sqrt[3]{\frac{\pi^2 M_p M_t}{\alpha^* 18kT}}, \tag{6-4}$$

where, d_p and d_t are the particle and the probe diameter, respectively, M_p and M_t are the particle and probe magnetic moments.

The dependence of stabilizing field value on the particle diameter is represented in Fig. 6.7.

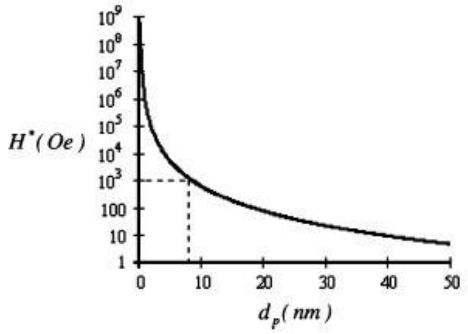

Fig. 6.7: Dependence of stabilizing field on particle diameter.[95]

Fig. 6.7 demonstrates that in Mironov model, stabilization of the magnetic moment in a field of 0.1 T (characteristic value of magnetic fields for *in situ* MFM measurements) is possible only for SP particles with diameters greater than 8 nm. To stabilize particles with $d < 8$ nm, high magnetic fields (more than 0.1 T) should be used or measurements have to be performed at low temperature.

7 Selected methods of sample preparation and characterization

7.1 Preparation of samples

7.1.1 General strategies for preparation of nanoparticles

Precipitation from solution

One of the easiest methods of preparation of the nanoparticles of transitive metal oxides is the precipitation from the liquid solution[96]. The Fig. 7.1 represents different mechanism of homogenous precipitation that leads to the creation of uniform particles in the best case.

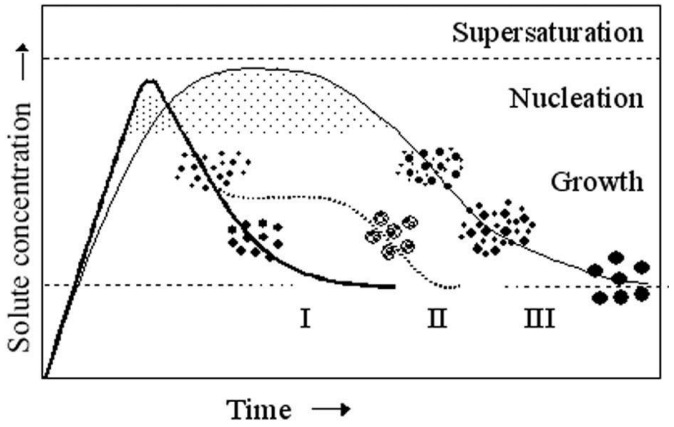

Fig. 7.1: Mechanism of formation of uniform particles in solution: curve I: single nucleation and uniform growth by diffusion; curve II: nucleation, growth and aggregation of smaller units; curve III: multiple nucleation events and Ostwald ripening growth[96].

The mechanism of homogenous precipitation could be divided into the four basic steps: supersaturation, nucleation, diffusion and growth.

When the concentration of constituents in the solution reaches the critical supersaturation, the nuclei of nanoparticles start to precipitate. These nuclei are allowed to growth by diffusion of solutes to their surface until the final crystallite size is attained. After the crystallites growth is finished, these start to agglomerate (the so-called secondary nucleation occurs). To achieve monodispersity, the stages of the first and secondary nucleation must be separated. Curve I. in Fig. 7.1 represents classical process of crystallite growth by diffusion, as was described above. Curve II. illustrates partial agglomeration of primary nuclei that also finally leads to growth of uniform particles. Curve III. displays process called the 'Ostwald ripening', in which the large crystallites growth to the detriment of the small ones. This spontaneous process occurs because larger crystals are energetically more favorable than the smaller ones that act as their 'nutrients'.

High-temperature decomposition of organic precursors

The decomposition of organo-metallic precursors in the presence of organic surfactants creates the samples of magnetic nanoparticles through good size control, with narrow size distribution and good crystallinity. The organic surfactants act as the 'reactors' inside which the reaction proceeds and the homogenous particles are grown. A variety of metal oxide nanoparticles can be prepared by this method, but the efficiency is generally lower in comparison with coprecipitation.

7.1.2 Preparation of $CoFe_2O_4$ nanoparticles

The samples were prepared in Instituto de Ciencia de Materiales de Madrid under assistance of Dr. Alechandro Roca and Dr. Maria Puerto Morales.

The preparation methods of pure $CoFe_2O_4$ nanoparticles sometimes lead to the creation of samples containing iron and cobalt oxides separately. The first assumption to prepare spinel structure is to keep the ratio of Co and Fe atoms in the metal precursors at 1:2, the second to keep pH at least above 8. Our samples have been prepared by 2 different methods of preparation- co-precipitation and decomposition of metal-organic precursor.

Coprecipitation

We have performed several reactions to prepare the mono-domain nanoparticles with the size bellow 40 nm. The particle size was mediated through the different pH values of solution; thus the coprecipitation reactions were performed for 3 times under different conditions (pH, temperature) and with different metal salt precursors. The size distribution was not mediated during the preparation, but prepared particles were finally centrifuged and stored in liquid and powder fractions, respectively. These cobalt-ferrite nanoparticles prepared by coprecipitation were labelled as CFC1 (**C**obalt **F**errite **C**oprecipitation no.**1**), CFC2 and CFC3, respectively, where the numbers qualify the reaction order.

CFC1

85mM $FeSO_4.7H_2O$ and 42.5 mM $CoSO_4.6H_2O$ was dissolved in 40 ml of water containing 15 mM KNO_3. Preheated solution was dropped into the 400 ml of 0.5 M NaOH and heated up to 90 ºC under the continuous purging of nitrogen gas to prevent the atmospheric oxidation of ferric compounds. The blue precipitate appeared, reaction took for 2 hours. Particles were washed with water for 5 times and magnetically separated from the liquid afterwards. The sample was divided into two fractions. The liquid fraction was stored in de-ionized water, powder of nanoparticles was obtained after drying the sample by nitrogen gas.

CFC2

2M $CoCl_2.6H_2O$ was dissolved in 5 ml of H_2O containing 3 drops of 37 % HCl, 0.5 M $Fe(NO_3)_3.9H_2O$ was dissolved in 40 ml of H_2O. Precursors were preheated to the 50°C and added into the 200 ml of boiling 1 M NaOH. Particles were washed with water for 5 times and magnetically separated afterwards. The liquid fraction was stored in de-ionized water and the powder was obtained by drying the sample in the flow of nitrogen gas.

CFC3

2M $CoCl_2.6H_2O$ was dissolved in 9 ml of H_2O containing 1 ml of 37 % HCl, 0.5 M $FeCl_3.9H_2O$ was dissolved in 80 ml of H_2O. Precursors were preheated to the 50ºC and added into the 400 ml of boiling 1 M NaOH. Particles were magnetically separated and washed for 5 times.

Surface treatment:

To stabilize the liquid fraction of nanoparticles and prevent them from aggregating, the solution containing particles was diluted in 100 ml of water (pH = 2) and 4 g of citric acid (CFC1)/sodium citrate (CFC2, CFC3) were added. Solution was heated up to 70°C. Final product was washed with water for 5 times and magnetically separated.

Thermal decomposition of organic precursor

The sample prepared by decomposition of organo-metalic precursor was labelled as CFD2

CFD2

4.6 g of $Fe(acac)_3$, 2.35 g of $Co(acac)_3$, 18.66 g of oleic acid and 22.3 g of dodecandiol were mixed in 200 ml of benzyl-ether. After 3 min of nitrogen gas purging, solution was heated at 200°C for 2 hours, the N_2 flow was cut afterwards and solution was boiling at 300°C for another 3 hours. Particles were washed in ethanol, magnetically separated and liquid fraction was stored in hexane. The powder fraction was prepared by drying the sample under the flow of nitrogen gas.

7.1.3 Preparation of SiO_2_Co(x)_Si(111) thin films

The SiO_2_Co(x)_Si(111) thin films were prepared by the method of magnetron sputtering in UHV at room temperature by Dr. Lancok in The Czech Academy of Science. The *x* in the shortcut represents the thickness of the cobalt layer in nm and brackets represents the multilayer in which the Co/SiO_2 layer is repeating 10 times. The same shortcut without brackets symbolise the single cobalt layer of thickness *x* covered only by one layer of SiO_2.

7.2 Characterization of compound and structure

We have used the method of inductively coupled plasma (ICP) for the compound studies and X-ray reflectivity (XRR), powder X-ray diffraction (PXRD) and transmission electron microscopy (TEM) for further characterization of the samples structure. Because the PXRD and TEM are well known and discussed methods, only the basic principles and the general information are emphasized here. More information can be found in the literature[97,98]. Principles of X-ray reflectivity measurements are included in the theoretical part; some technical details are depicted in this section.

7.2.1 Inductively coupled plasma (ICP)

This method is based on the atomic spectrometry and allows detection mainly of metal atoms. The result is the precious ratio of metal elements in the sample. The detail description of method is in Handbook by Nelms[99].

7.2.2 X-ray reflectivity

The X-ray reflectivity measurements were performed using high resolution X-Ray diffractometer (X'Pert Pro MRD)[100] parallel beam configuration, using the Cu K_α source. The reflected intensity was monochromatized by the channel-cut graphite monocrystal and the mirror. Both the refracted and incident beams were collimated by the slits of 0.01 and 0.04 mm, respectively; the diameter of the incident beam aperture was 0.1×1 cm. The reflectivity curves (dependence reflected intensity on the angle of incidence) were recorded in the parallel beam configuration with ω-2θ scan in step of 0.01° within 0-1.2° range.

To obtain accurate reflectivity curve, the sample was precisely aligned to the centre of the X-ray beam and the half of the intensity of incident beam was detected by the photo-detector. The sample was mounted on the highly precious goniometer (resolution 0.001 degree in our measurements).

Reflectivity curves simulation

The reflectivity curves were simulated and then refined in the X'Pert Reflectivity software. At first, the critical angle was determined from the maximum slope of the first fringe (from its first derivation). Then the three parameters such as the layer thickness, density and the roughness of the inter-layers were set up, step by step. Changing the parameters manually at first, the current position of the Bragg peaks of the simulated curves with respect to the measured ones was obtained and the final software refinement was done. The roughness of the upper layer was estimated from the AFM measurements. In case of the multilayers, the density was set up to be periodically decreasing with increasing number of the layer. It was not possible to cover up the

spatial and density imperfections on the boundaries, because the software is calculating only with values in the direction normal to the film plane.

7.2.3 Powder X-Ray diffraction

The PXRD was used for determination of the material composition and the size of the crystallites in the samples CFC1, CFC2, CFC3 and CFD2 respectively. X-ray diffraction is based on the incident beam diffraction at oriented lattice plain of individual crystallites; the conditions for diffraction are given by famous Bragg equation[97].

Rietveld refinement

The profile analysis of PXRD pattern covers qualitative (geometry of crystal lattice, distortions and strain) and quantitative (precious structure, texture) information about the samples. The broadness of the peaks, which is the convolution of the crystallite size and the instrumental function, serves as the starting point for calculating the crystallite size using the well-known Debye-Sherrer formula[97].

The refinement of PXRD pattern has been done in FullProf program[101] in which the Rietveld refinement method is included. This method is based on the least square method in which the simulated and the measured data are brought closer to each other by progressive refinement of fitted parameters. The peak positions are calculated from the space group symmetry and the lattice parameters, the peak intensities give information about atomic positions and the peak profiles are approximated by the simple Pseudo-Voight function[102]. To obtain real size of the crystallites, the automatic de-convolution of the known (measured) instrumental function was done in our case. Further details of the procedure can be found in the FullProf manual[101] .

Experimental setup

The X-ray diffraction patterns were recorded in parafocusing Brag-Brentano geometry (Bruker XRD diffractometer[103]) using Cu K_α radiation at room temperature. The intensity vs. 2θ scans were taken with the step of 0.05° within 20°-140° range with the 10 s duration per point.

The diffraction patterns were analysed with respect to the expected structure and the lattice parameters together with the crystallite sizes were refined in the FullProf programme.

7.2.4 Transmition electron microscopy-TEM

This method uses the interaction of the electron, described by the wave function, with the matter and allows either direct observation of the material under investigation or the electron diffraction which is the analogy to the XRD (the main advantage is that the

electron diffraction provides much bigger part of the reciprocal space than the XRD technique, because of its wavelength).

The TEM images of cobalt-ferrite nanoparticles were done in ICMM Madrid using a 200-keV JEOL-2000 FXII microscope. The samples were prepared by dropping one drop of the diluted solution of nanoparticles on the carbon coated copper grid and the solvent was allowed to evaporate at room temperature. The ImageJ software was used for statistical treatment of particles sizes.
The TEM images of SiO_2_Co_Si(111) thin films were done by Dr. Mariana Klementova, Inst.of Inorganic Chemistry at the HRTEM JEOL JEM 3010 in the Czech Academy of Science.

7.3 Magnetic measurements

The great accent was taken to the measurements of magnetic properties of nanoparticles and granular thin films, respectively. The magnetic properties of nanoparticles were measured by MPMS7XL device (working with SQUID detection coils); those of the thin films were measured by PPMS9 and PPMS14 devices, all by Quantum Design[104-105]. Declared error of the temperature measurement and values of the measured magnetic moment are less than 1%. Only the information that is essential for understanding of results of experiments is summarized here, more details can be found in the proper manuals. Only some technical details of less convenient techniques, such as VSM and torque magnetometry are presented.

7.3.1 Temperature dependence of magnetization and magnetization isotherms

In the so-called dc measurements, the static magnetic field (produced by the superconducting coil) is applied to the sample and the absolute value of the sample's magnetic moment is measured. In our case, the zero field cooled (ZFC) and field cooled curves (FC) were measured in temperature range of 2-350 K (400 K) using the following measuring protocol: the samples of nanoparticles in powder form were put into a gelatine capsule (the same one as are used for drug delivery). To avoid particle moving during the measurement, the samples were fixed by peaces of polystyrene (measurements at temperature up to 350 K) or by the glue (experiments up to 400 K). Then the samples were cooled down to 2 K in zero field, magnetic field of 20 mT was applied and the temperature dependence of magnetization was measured (ZFC curve). In the second step, sample was cooled down again holding the external magnetic field unchanged and the FC measurement of temperature dependence of magnetization was performed.

Magnetization isotherms were measured at selected temperatures (in temperature range 2-400 K) in the field ranging up to 7 T in both polarities. The evolution of coercivity, H_C at low temperatures was examined and calculations of the average particle magnetic

moment were performed (by extrapolating the magnetization isotherms without any hysteresis by Langevin function).

7.3.2 Ac susceptibility measurements

Another option to study dynamics of granular nanoparticles systems is the ac susceptibility measurement. This technique allows measurements of the susceptibility in very small alternating magnetic field of amplitude $H_A \sin\omega t$ (under a small external dc magnetic field)

The magnetic susceptibility is given by the two components; χ' in-phase (also noted as real part, magnitude of the susceptibility χ) and χ'', out-of phase component (imaginary part, phase shift relative to the drive signal).

The real component of the susceptibility, χ' indicates dissipative processes in the sample. Relaxation and irreversibility in interacting systems (such as spin-glasses) give non-zero χ''. In ferromagnets, non-zero χ'' indicates the domain wall motion. The cusp at the χ' vs. T curve can be attributed to the blocking temperature in SPM and freezing temperature in SSG systems.

Both the temperature dependence of real and imaginary parts of susceptibility, resp. was measured in zero and nonzero (20 mT) external dc magnetic field, respectively. The experiments were performed with amplitude of alternating field 0.3 mT, in frequency range of 10 Hz-10 kHz (pokud na PPMS, tak ano, jinak jen 1 kHz).

7.3.3 Vibrating sample magnetometer – VSM

VSM is the technique in which the vibrating sample induces the current I in the detection coils. The sample is vibrating with oscillation frequency 40 Hz, amplitude of oscillation is 1-3 mm. The sensitivity of detection circuit reaches the value of 10^{-6} emu. Classical VSM method allows measurement in temperature range of 2-350 K. It is also possible to use VSM+oven setup in which the sample heater allows reach temperatures up to 1000 K.

Bboth methods were used in measurements of magnetic properties of SiO_2_Co_Si(111) thin films. In the temperature range of ?2 - 350 K, the temperature dependence of magnetization and magnetization isotherms were measured in parallel and perpendicular orientation to the applied field. Magnetic properties of some samples were also examined in oven regime in orientation parallel to the applied field. Because the small samples (0.5 x 0.5 mm) exhibit small magnetic moment (10^{-5} emu) and they were mounted on a plastic stick or were stabilized by the cement (oven regime), the strong diamagnetic contribution in the most of the measured data has appeared.

7.3.4 Torque magnetometry

Torque magnetometry allows performing angular-dependent measurements of the magnetic torque $\tau = m \times B$ which is experienced by a sample of magnetic moment m in an applied magnetic field B. When the torque of the sample is measured, the magnetic moment of the sample can be determined. The method allows measurements of temperature dependence of magnetization in temperature range of 2 - 350 K.
The sample is mounted on the torque lever chip that is twisting under the influence of applied magnetic field. The torque is directly measured by the piezoelectric circuit with the crystals mounted inside the chip pins. The whole chip with the sample is mounted in the rotator, which is responsible for positioning the sample in range from 0 to 365 degrees with respect to the field applied in vertical direction.

Fig. 7.2 illustrates the basic set-up of the experiment: magnetic sample mounted on a chip in presence of the external magnetic field. Because the magnetization component perpendicular to the external magnetic field is measured, it is accurate to use the samples with ? high anisotropy such as crystals and thin films.
The preparation of the sample for the measurement is quite tricky because the samples are required to be lighter than 10 mg with dimension 1.5 mm × 1.5 mm × 0.5 mm and the torque of 5.10^{-5} N.m should damage the chip. The upper and lower values of reachable signal are 10^{-5} and 10^{-8} Nm, respectively.
Three basic experiments have been performed: angular dependence of torque that gives information about direction of easy axis of magnetization, convenient temperature dependence of magnetization and magnetisation isotherms measurements (from which the MAE can be determined), both at constant angle.

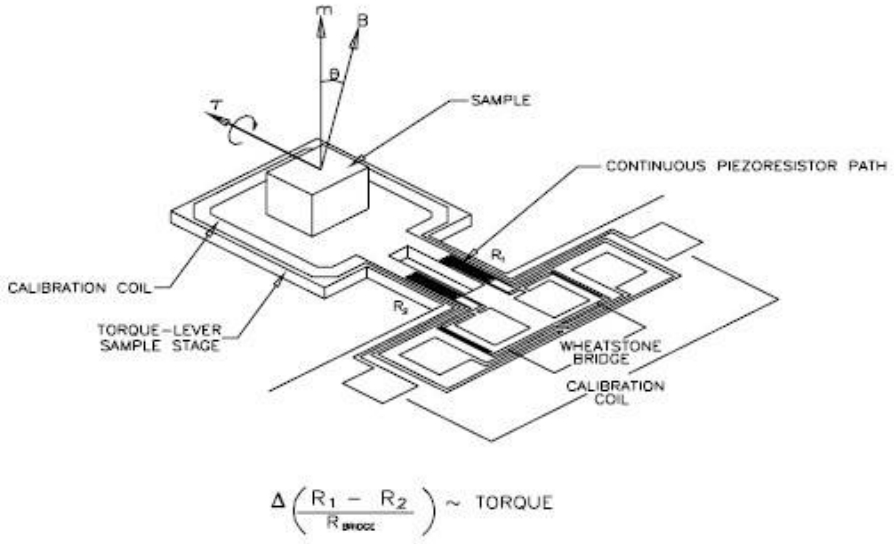

Fig.7.2: Illustration of the torque acting in the magnetic sample mounted on the torque lever chip, the approach of determining the torque by the piezoelectric circuit[104] .

7.4 Scanning probe microscopy

All details of experiments that were performed with the SPM MultimodeV (Veeco) are described together with the results and appropriate comments in the following chapters. It is also not the case to mention here the details about the setting of the sample, probe, laser, photodetector, the electronics and the scanning parameters, because either the process is known for the users or the general strategies are summarised in manuals by Veeco and finally, the scanning parameters are changing with each individual captured image.

7.4.1 Details of the AFM and MFM experiments

The following samples were examined: CFD2 nanoparticles and SiO_2_Co(x)_Si(111) thin films, both by the AFM (to obtain topography of the samples) and the MFM (to gain information about magnetic structure). The SNL-10 A, RFESP and MESP(H) probes were used namely in contact mode imaging, tapping mode imaging and for magnetic force microscopy. The parameters of these probes are summarised in Table 7.1.

In AFM experiments, the height and deflection in case of CM and the height, amplitude and amplitude error in case of TM were captured. The images were processed in Nanoscope software 7.3[106], using the 1st to 3rd order of flattening procedure and the cross section analysis. The grain boundaries were highlighted using ImageJ and Gwiddion software.

Performing MFM experiments, two approaches in capturing the magnetic phase images were used. In the first one the vertical magnetic field generated by the permanent magnet built in the JV scanner holder was used, mounting the samples directly to the scanner head. The field of the scanner holder was said to be 0.2 T[88]. In the second approach, samples were mounted on the metal stab before attaching it to the scanner head. It was shown that metal stub reduced the field acting on the sample from 0.2 T down to 0.005 T[88].

MFM experiments were recorded by interleaving the topographic scan to the Lift Mode scan, where the free oscillating cantilever was brought to the distances 15 - 100 nm above the topographical height of the surface at each point and the phase image scan was captured. This method should sufficiently restrict the contribution of the topography to the magnetic phase image.

The thin films were examined at first in contact mode to get the information about topography and emphasize the LSH, which prevents the tip from damaging but is sufficient to obtain magnetic phase image. The MFM experiments were performed for several times with magnetic tip, magnetizing the sample in different orientations of applied external magnetic field.

The cobalt ferrite nanoparticles were visualised at first in the tapping mode. Then the MFM experiments with the MESP and MESPHM probes in different LSH were performed. The nanoparticles were also tested in nonmagnetic regime (with nonmagnetic tip) with the same scanning parameters as in the MFM regime, to identify possible contribution of the topography to the magnetic phase image, if there were any. The phase contrast for individual nanoparticles was measured using the section analysis in Nanoscope 7.3. software.

probe	k (N/m)	f_0 (kHz)	M (emu)	H_C (Oe)
SNL-10 A	0.58	60	-	-
MESP	2.8	75	1×10^{-13}	400
MESP-HM	2.8	75	$>3\times10^{-13}$	400

7.4.2 Preparation of nanoparticles for measurement

The nanoparticles stored in the liquid solutions were used for the preparation of the samples for the AFM/MFM measurements.

CFC3

Magnetic fluid (MF) was diluted in the ration 1:100 in de-ionized water and was stirring for 10 s. Then the solution was diluted for the second time 1:10 with the de-ionized water and stirred for 10 s again. 5µl of 1:1000 diluted MF was dropped on the freshly cleaved mica (rinsed with de-ionized water and dried in air for 30 min afterwards) and dried at room temperature for 10 min. The mica substrate covered with nanoparticles was stabilized by heating in air at 55^{o}C for 10 min.

CFD2

The sample was prepared by the same method as in the previous case only with one modification - use of the hexane instead of de-ionized water.

7.4.3 Calibration of cantilever's spring constant, *k*

To know preciously the value of the probe's spring constant is necessary for further calculations such as determination of the cantilever sensitivity and probe's amplitude of oscillation in metric units and also all the information allowing further analysis of the captured images. The spring constant of cantilever given by the manufacturer can differ from the real one even in 50 %. Because of that, the calibration of the probe has to be done. There are many approaches for cantilever calibration. In general, the methods are different for the probes with $k < 1$ N/m and $k > 1$ N/m.

For the probes with $k < 1$; one of the easiest and the most accurate method is the so called 'thermal tuning method'[107] which is based on the cantilever's mechanical response to the thermal noise. The MultimodeV Veeco hardware is able to measure cantilever's fluctuation as a function of time and then fit frequency spectrum of the mechanical response by the Lorenzian function. Knowing the sensitivity of the cantilever (the dependence of deflection on the applied voltage) the spring constant can be calculated.

For calibrations of the cantilevers with $k > 1$ N/m, the Sader's method[108] based on the analytical approach of slightly damped cantilever can be used. The technique is appropriate in the first approach only for rectangular cantilevers and requires their plan view dimensions, resonance frequency, quality factor (Q), and the density and viscosity of the fluid in which these are measured (typically air). In case of the V-shape cantilevers, which usually have the spring constant $k > 1$ N/m the method can be slightly modified. If we have both the rectangular and V-shape cantilevers on one chip, it is sufficient to calibrate the rectangular cantilever at first and then, with use of simple calculations, determine the spring constant of the V-shaped one. The detailed mathematical approach on Sader's method is described in ref. [108].
All used cantilevers were calibrated by one of these methods. The cantilever sensitivity was determined at first, measuring the elastic response of the tip (deflection-applied voltage curves) on the surface made of the stiff material (mica). Appropriate spring constant values are written under the SPM images in the experimental part of the thesis. All the scanning parameters, given originally in the Voltage units, were recalculated to the metric ones, using the determined sensitivity values.

8 Magnetic force imaging- the first successful results obtained in our lab

We present here the magnetic gradient images that were taken in our laboratory, as the result of the first experiments done in MFM mode with Multimode V microscope (Veeco) with the samples that were already measured elsewhere (we tested the samples from Barcelona). It is important to show here that if it is possible, we are able to visualise magnetic structure in a sufficient resolution and these magnetic gradient images are of the same nature as those that were already published[110].

We have investigated the two types of magnetic tips; the commonly used tips with an average magnetization (MESP) and the tips with high magnetization (MESPHM). It will be shown that the MESP tips are useless at imaging the structures with very low magnetization pointing in the direction perpendicular to the plain.

Recording of the scanning parameters is useful (sometimes necessary) for interpretation of the observed images, further repeating of the experiments at the same conditions and also for better understanding of the material nature. By the scanning parameters we mean the general parameters as the scanning mode, type of the scanner and the tip which were used, the scan rate and the parameters connected with the cantilevers such as the force constant k, oscillation frequency f_0, the Q factor (represents the damping) and the amplitude of the free oscillation A (amplitude setpoint). The k and f_0 are given by the manufacturer, but the values are not much precious and it is better to calibrate each cantilever separately. Knowing these quantities, it is possible to determine the sensitivity of the cantilever and then calculate the deflection or the oscillation amplitude of cantilever (that are commonly measured in volts). We have calibrated the cantilevers by the Thermal Tuning and then used the Saader's approach on the force constant evaluation. The observed values are discrepant from those given by manufacturer in less than 20%.

5.1. Recording tape

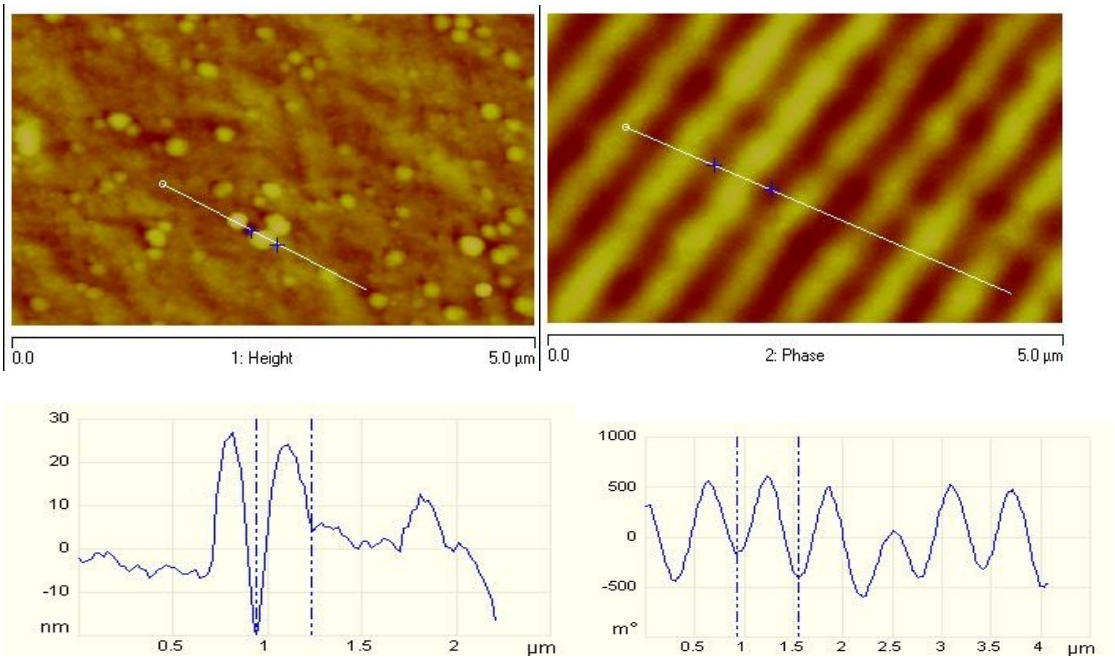

Fig. 8.1: The recording tape images taken in a TM mode. Scanning parameters: f_0 = 82.6 kHz, k = 4.33 N/m, setpoint amplitude A = 420 mV (23 nm), lift scan height= 50 nm. Left: Topography image, the cross section bellow. Right: Magnetic phase image, the cross section bellow.

The classical recording tape was stick on the mica surface and scanned in a tapping mode with a fresh magnetic tip (MESP by Veeco). The Fig. 8.1 shows the topography (left) and the magnetic phase (right) images. The bright and dark stripes on the phase image represent the oppositely magnetised areas (let say the domains) of the tape. It is obvious that there is no contribution from the topography to the phase image. The maximum height of the features on the surface reached 30 nm, we have scanned the surface in a lift scan height of 50 nm with the amplitude of oscillation close to 23 nm. During the scanning in the lift mode (to obtain phase image), microscope copies the trace of the topography image, keeping the tip in a distance (the lift scan height) given by the user. If this trace would not be followed, the contact with the highest features would occur. Because there is not any visible contribution of topography to the phase image, there is no direct contact between the tip and sample or the contribution of another long range forces.

5.2. Permalloy film

We also examined the domain structure of the permalloy film. The same scanning parameters as in case of the recording tape were used. The topographical image exhibits the low roughness of the surface (less than 2 nm). The striped pattern in magnetic phase image was observed. The curved shape of this stripes and the decreasing intensity is not the artefact of the measurement, but the real magnetic structure of this material (the original images are not available, but we claim they are of the same nature). The ellipse encloses the area in which the domains shift its orientation.

It is important to remark that even if the patterned structure is observed, the maximum value of phase reaches 0.3 degree and the contrast between the areas of (probably) opposite orientation is sufficient. This shows us that the intensity of the noise (thermal or mechanical) is far under the tenths of degrees.

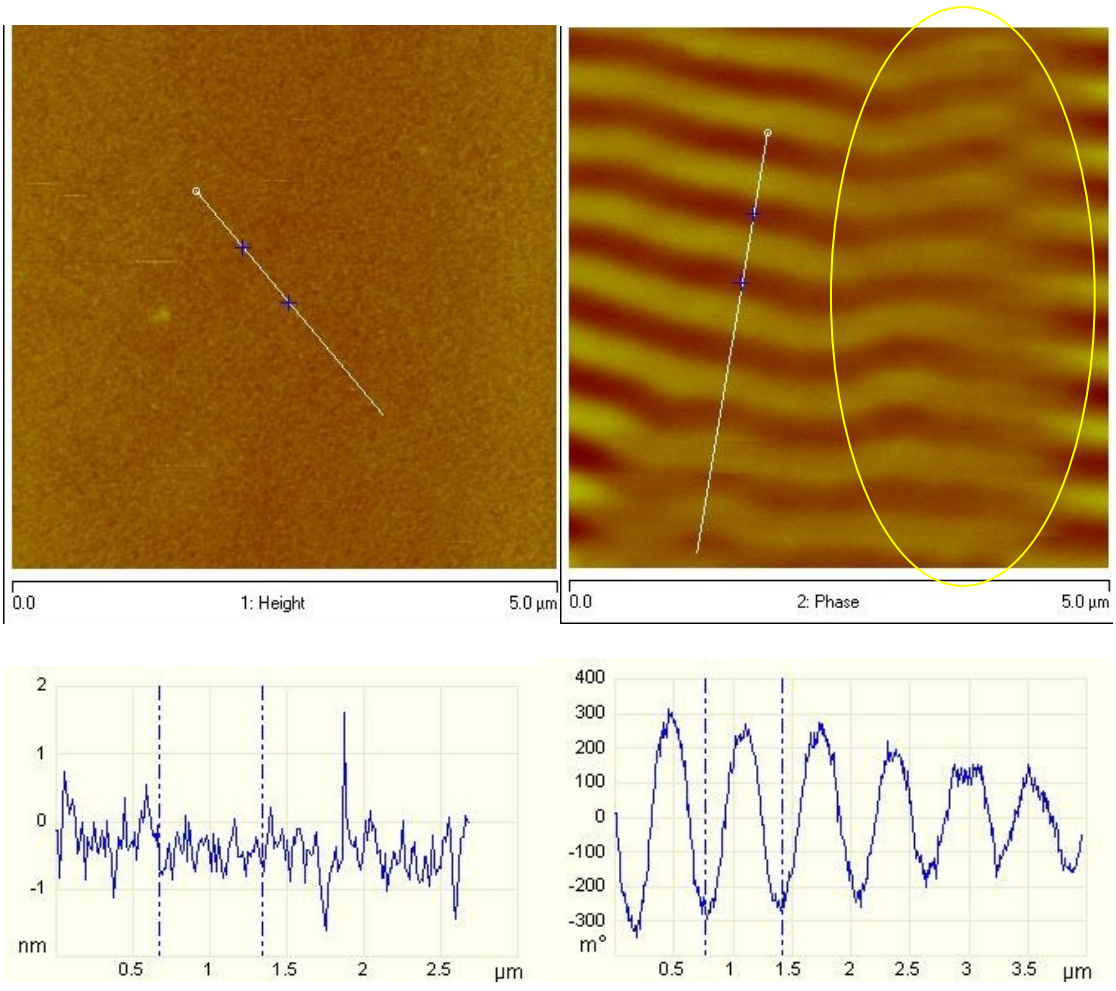

Fig. 8.2: The permalloy film images taken in a TM mode. Scanning parameters: f_0=82.6 kHz, k = 4.33 N/m, drive amplitude 1000 mV (53.19 nm), LSH = 50 nm. Left: Topography image, the cross section bellow. Right: Magnetic phase image, the cross section bellow.

5.3. $CoFe_2O_4$–$BiFeO_3$ columns

The CFO-BFO columns were measured in a field of 0.2 T (the original field of the magnetic sample holder). The original paper demonstrates that if the field of 2 T is applied, more than 80% of columns are magnetized in its direction; thus magnetizing the sample in field of 0.2 T should switch the magnetization of some columns to the direction perpendicular to the plain [110].

The Fig.8.3 exhibits magnetic phase images of CFO-BFO samples magnetized in 2 T taken from the original paper (3a).

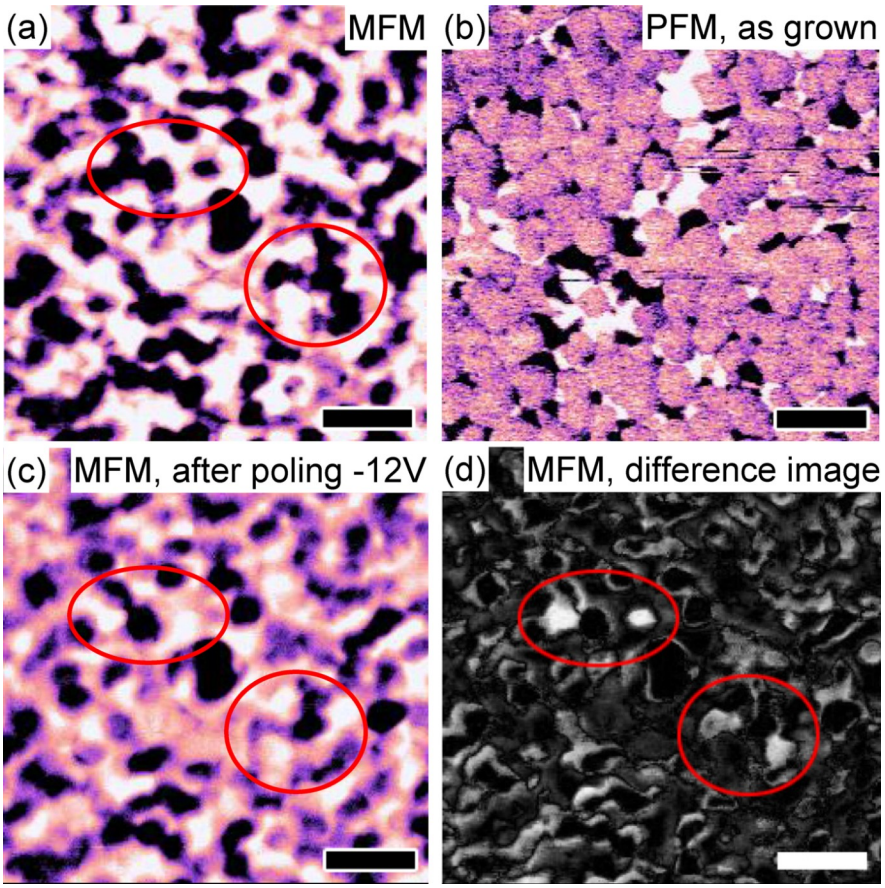

Fig. 8.3: Magnetic phase image (a), topography (b), magnetic phase image after switching the magnetization by electric field (c), the difference of (a) and (c), (d). Adapted from the paper by N. Dix (Dix et al. 2009)[110] .

In our experiment, we have scanned the sample in a TM with the MESP and MESPHM tips, respectively. The magnetic phase image was captured in a lift scan height of 50 nm (MESP) and 70 nm (MESPH). Phase contrast images taken with the low magnetized tip (MESP) exhibit extremely little contrast and we can only wonder if it is caused by differently oriented magnetic moments in columns or it is some artefact. The use of the highly magnetized tip (MESPHM) significantly improves the quality of the magnetic phase image, similar to those from the original paper. The bright and dark areas are the groups of columns with magnetization pointing up and down, respectively. Despite this

magnetic contrast, the grain boundaries structure has appeared on the magnetic phase image scan. It is probably the consequence of the topography influence (long range Van der Waals forces), but the explanation is not still clear.

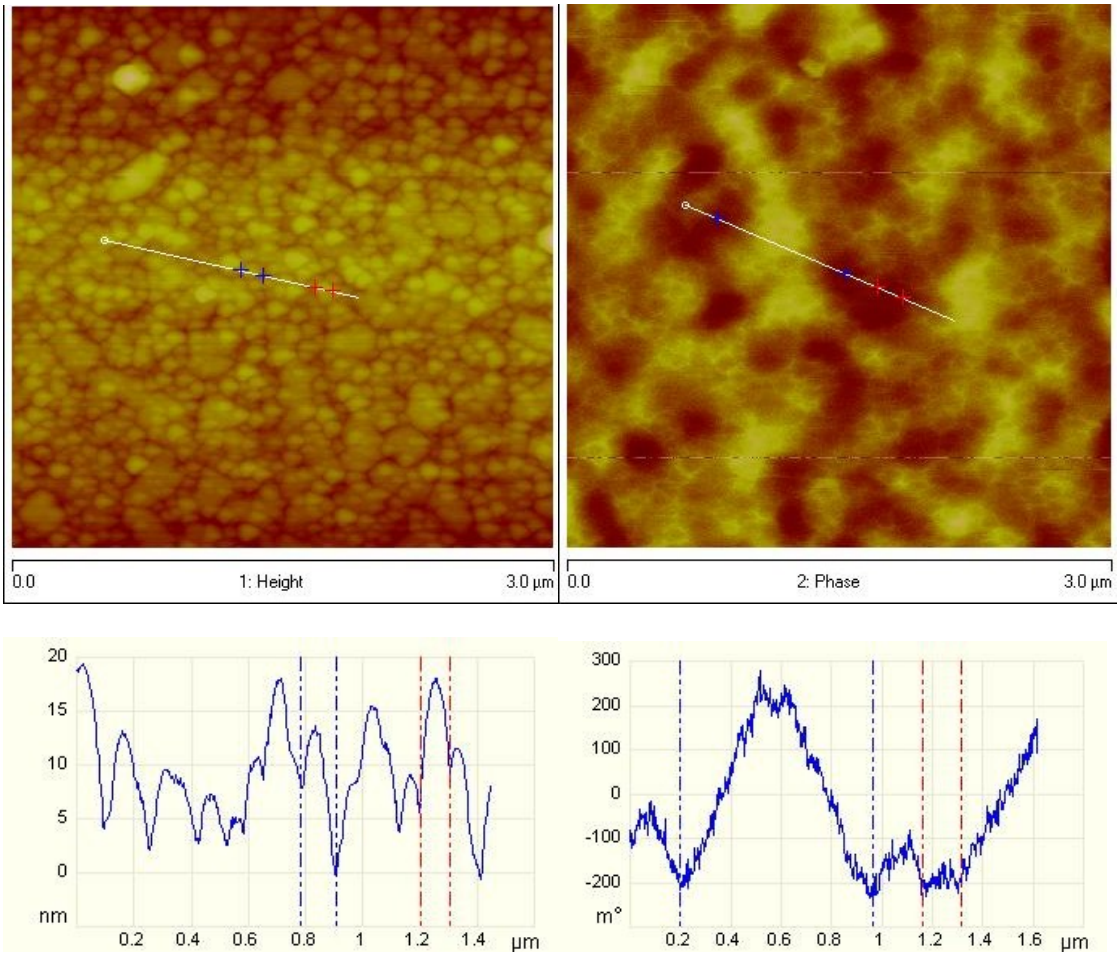

Fig. 8.3: First row: Topography and phase image of CFO-BFO sample. f_0=83 kHz, amplitude setpoint AS 1450 mV, scan rate 0.8 Hz, Q factor 338, LSH 50 nm. Second row: MESPHM tip, f_0=87.79 kHz, AS 1320 mV, scan rate 0.5 Hz, LSH 70 nm. The cross sections belong to the second row images

9 $CoFe_2O_4$ nanoparticles

9.1 Elemental composition

To work out if our samples contain $CoFe_2O_4$ nanoparticles, the chemical analysis in case of particles prepared by coprecipitation was done by the ICP method. Using this method, the ratio of heavy elements presented in the sample was obtained. Considering that our samples were composed of pure cobalt-ferrite, the Fe : Co ratio should be equal to 2 : 1. The resulting attendance of elements in CFC1 and CFC2 samples was 33 % of Co and 66 % of Fe and 32 % of Co and 64 % Fe for CFC3 sample suggesting, that the samples contain pure cobalt-ferrite (this fact can be easily proven by further magnetic measurements, because the magnetic properties of $CoFe_2O_4$ in comparison to the iron and cobalt oxides are significantly different).

9.2 Shape, size and structure characterization

9.2.1 TEM

The TEM was used for direct observation of the nanoparticles. Comparing the TEM images of individual samples, it is obvious that the particles prepared by the coprecipitation exhibit irregularity of shapes and high distribution of particle size whereas the particles prepared by the decomposition have uniform both size and shape.

The mean value of particle size was analyzed using the ImageJ software in which the diameter of more than 200 particles in each TEM image was determined.

CFC1

Regarding the TEM images, this sample seems to be inappropriate for further magnetic studies at all because of the large particle size – these nanoparticles probably do not obey the claim to be single domain. The critical size of single domain $CoFe_2O_4$ nanoparticle was experimentally suggested to be about 40 nm, the theoretical prediction gives 70 nm[96].

Looking at Fig. 9.1, it is obvious that there is significant particle size distribution-particle diameters are ranging from 30 up to 160 nm. The mean particle diameter (determined from the Log-normal distribution) is equal to 76 nm.

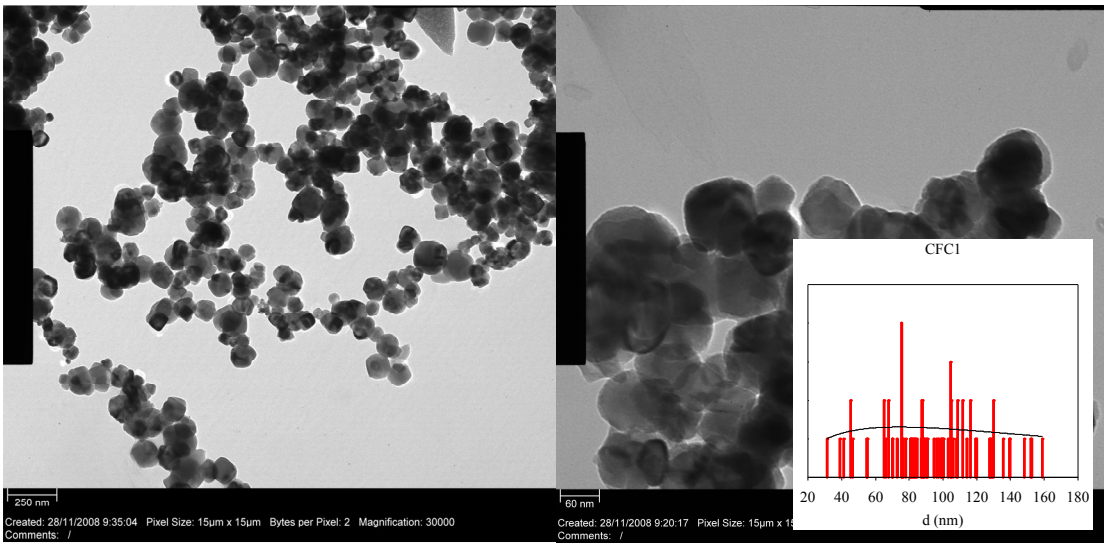

Fig. 9.1: TEM images of the CFC1 sample, the distribution of particle diameters together with the fit of log-normal distribution.

CFC2 and CFC3

The samples labelled as CFC2 and CFC3 exhibits almost similar particle size and shape, as is obvious from the TEM images and its statistical analysis of particle diameters.

The particles diameters are ranging from 7 to 40 nm (CFC2) and 6 to 44 nm (CFC3), mean values determined from fits of log-normal distribution are 16 nm and 15 nm for the CFC2 and CFC3 sample, respectively.

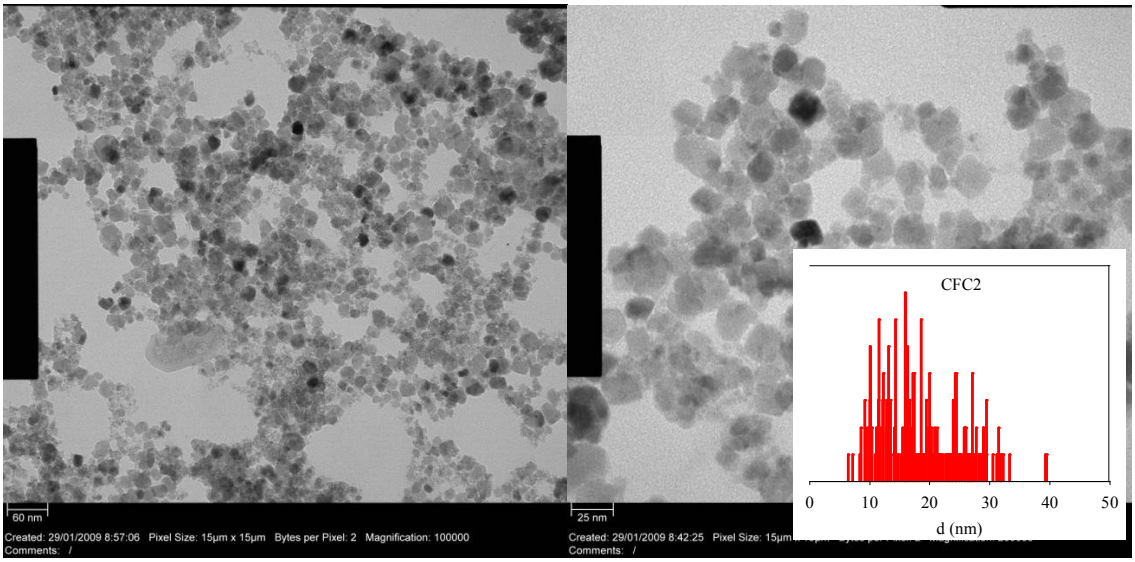

Fig. 9.2: CFC2 sample, TEM images and the distribution of particle diameters.

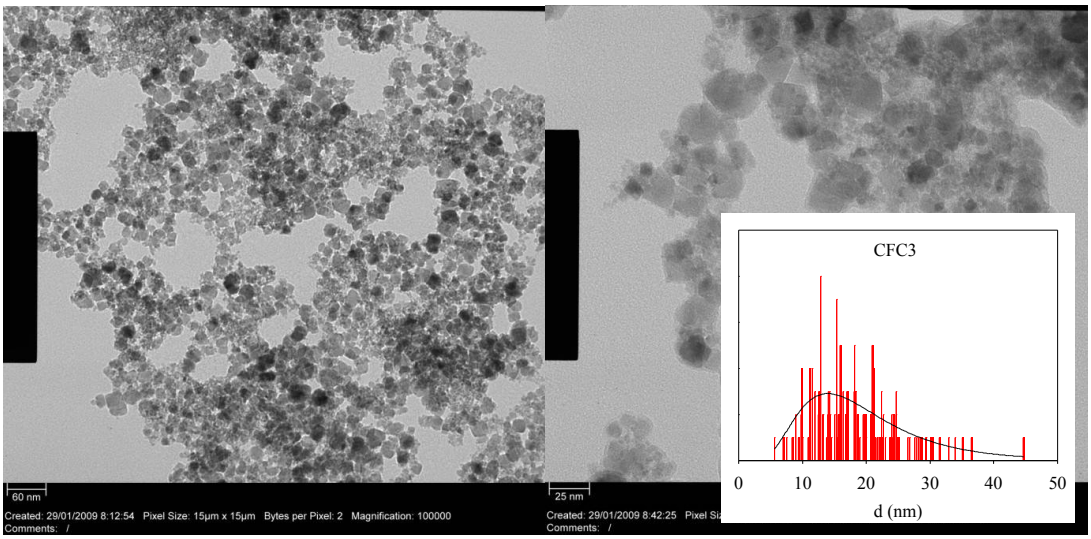

Fig. 9.3: CFC3 sample, TEM images and the distribution of particle diameters together with the fit of log-normal distribution of particles.

The CFD2 sample exhibit more symmetric shape and low particle size distribution in comparison with samples made by the coprecipitation. The particle diameters lie in the interval 2-18 nm, but the largest fraction of them has diameters ranging from 5 to 12 nm. The mean value determined from the Log-normal distribution gives 7.8 nm.

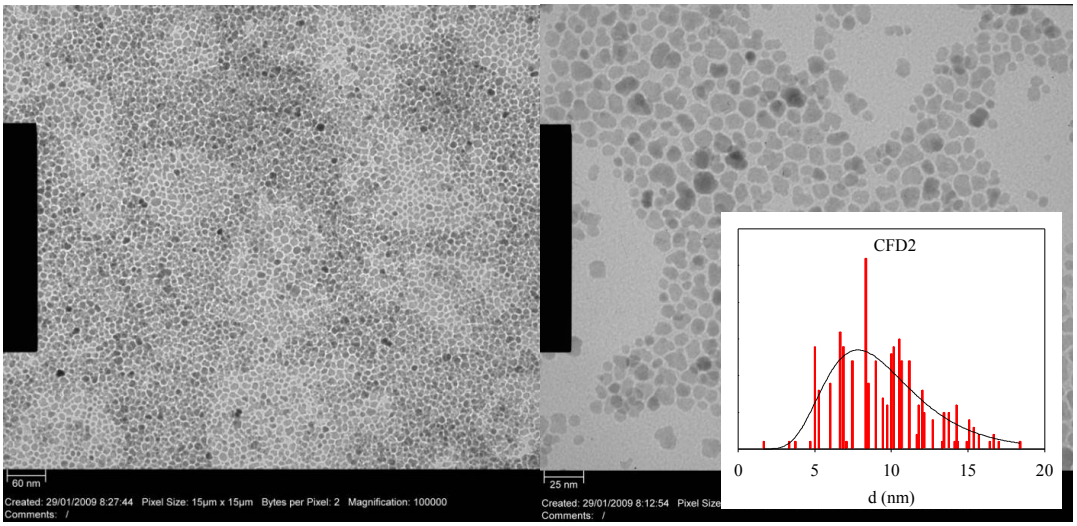

Fig. 9.4: CFD2 sample, TEM images and the distribution of particle diameters interpolated by Log-normal distribution.

9.2.2 The powder XRD diffraction (PXRD)

The particle structure was determined using the powder X-ray diffraction and further profile analysis in the FullProf software.

The PXRD patterns reveal that all peaks positions correspond to those of the cubic inverse spinel structure of $CoFe_2O_4$ (space group Fd-3m). The data have been evaluated by the Rietveld fitting procedure; the precious values of lattice parameter and size of the

crystallites have been determined. Particles were considered to be spherical, the shape anisotropy and the anisotropic strain were not involved in the fitting procedure. Because the broadness of the peaks is given both by the particle diameter and the resolution function, the deconvolution with use of the measured instrumental function have been done in the FullProf.

Considering the nanoparticles, crystallinity of the particle strongly depends on the method of preparation. It is misleading to assume the whole particle is single-crystalline. In reality, we can imagine that the nanoparticle obeys the so-called core-shell structure in which the particle core acts as a crystallite and the shell structure is somewhere between a polycrystalline and an amorphous phase; thus only the core part significantly contributes to the diffraction pattern. That is the reason why the particles sizes refined from the XRD measurements are smaller than those determined from the TEM images, especially in the case of CFC1 particles that are extremely big and simply polycrystalline.

PXRD patterns of individual samples together with the refined structure are presented in Fig. 9.5. The particle diameter and the lattice parameter *a* are summarized in Table 9.1.

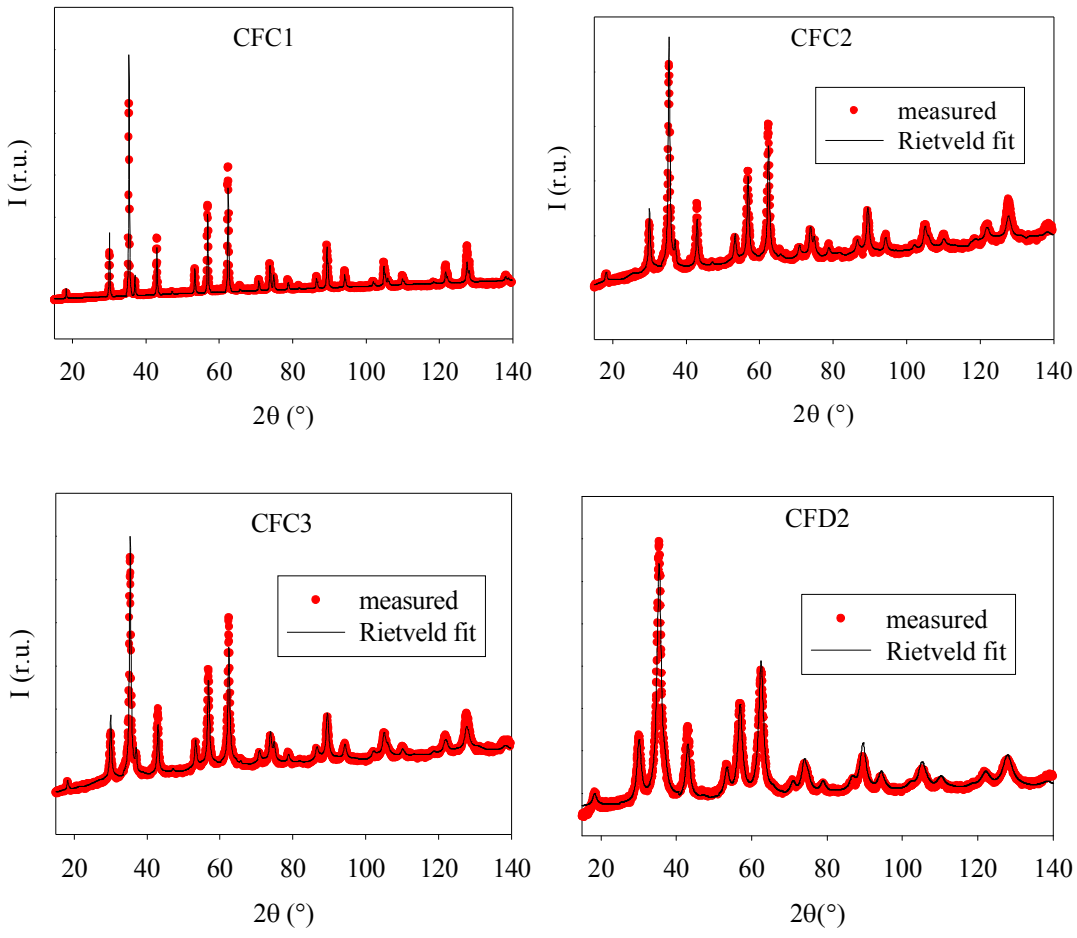

Fig. 9.5: PXRD patterns (red) with the curve obtained in Rietveld refinement method (black line).

Table 9.1: Particle size and structure. The particle diameter *d* wasobtained by TEM and XRD, *a* is the lattice parameter.

sample	method	d_{XRD}(nm)	d_{TEM}(nm)	a (A)
CFC1	coprecipitation	42	76	8.411
CFC2	coprecipitation	12	16	8.413
CFC3	coprecipitation	13	15	8.411
CFD2	decomposition	5	8	8.365

9.3 Magnetic measurements

9.3.1 Temperature dependence of magnetization

The temperature dependence of magnetization was measured for all samples in small fields (20 and 50 mT) up to 400 K. The maximum of the ZFC curve, T_{MAX} and the coinciding point of the ZFC-FC curve, T_{DIFF} do not meet each another in one point as is expected in ideal case (Appendix A) that suggests the significant particle size distribution in the samples. Thus the temperature T_{MAX} can be approximately attributed to the blocking temperature T_B of the major fraction of the particles, whereas the T_{DIFF} is the temperature where the moments of the largest particles freeze.

CFC2 and CFC3

The ZFC-FC curves coincide at 400 K and also the T_{MAX} reaches 390 K, thus the main fraction of the particles is in the blocked state in the whole temperature range. The saturation of the low temperature part of the FC curve is a consequence of the interparticle interactions, probably of dipolar origin. As was explained in the theoretical part, the strength of the interparticle interactions determines the nature of the system. Even if the strength of the interactions is not known exactly, it is highly probable that the interactions are strong because of the direct contact between magnetic nanoparticles, even within a single prticles; thus the samples are assumed to exhibit collective phenomena (such as in the SSG) and the T_{MAX} and T_{DIFF} should be affirmed as the freezing temperatures, T_f, of the mean and largest fractions of nanoparticles, respectively.

Because of the particle irregular shape and size these are not suitable for further MFM studies.

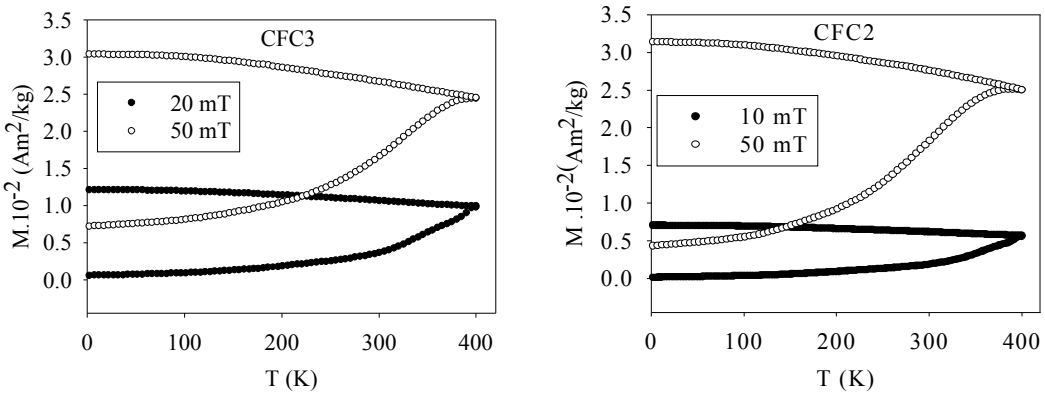

Fig. 9.6: The ZFC-FC curves of CFC3 and CFC2 samples, measured in field of 20 and 50 mT, respectively.

CFD2 sample

The Fig. 9.7 shows the ZFC-FC curves for the CFD2 sample, measured in 50 mT. The values of T_{MAX} and T_{DIFF} are lower than in case of the CFCx series. This corresponds well with the increase of the blocking (or freezing) temperature with increasing particle size, because the magnetocrystalline energy is higher for larger particles (considering the similar effective anisotropy constant, K_{eff}) and the thermal fluctuations overcome the barrier at higher temperatures.

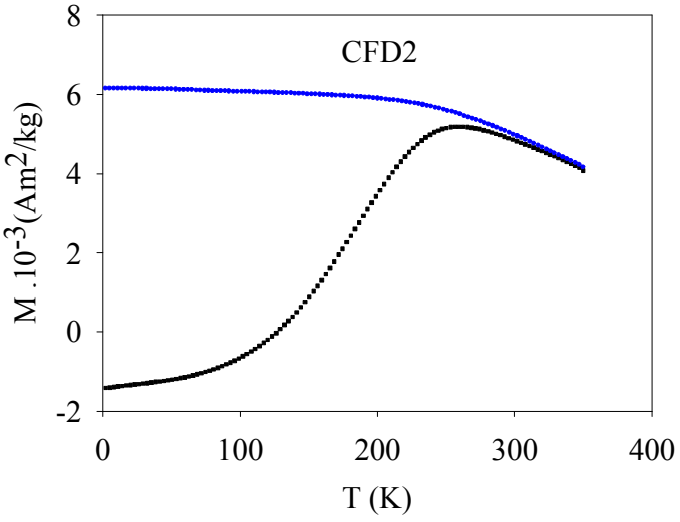

Fig. 9.7: ZFC (black) and FC (blue) curves of the CFD2 sample, measured in field of 50 mT.

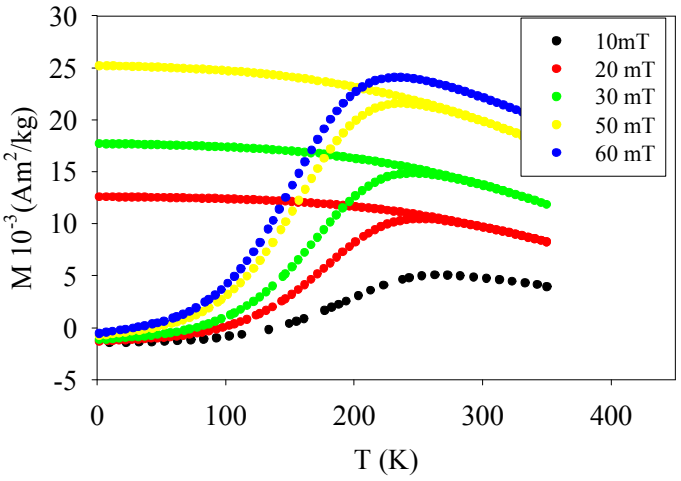

Fig. 9.8: ZFC-FC magnetization curves with increasing magnetic field demonstrating the shift of the T_{MAX} and T_{DIF} in CFD2 sample.

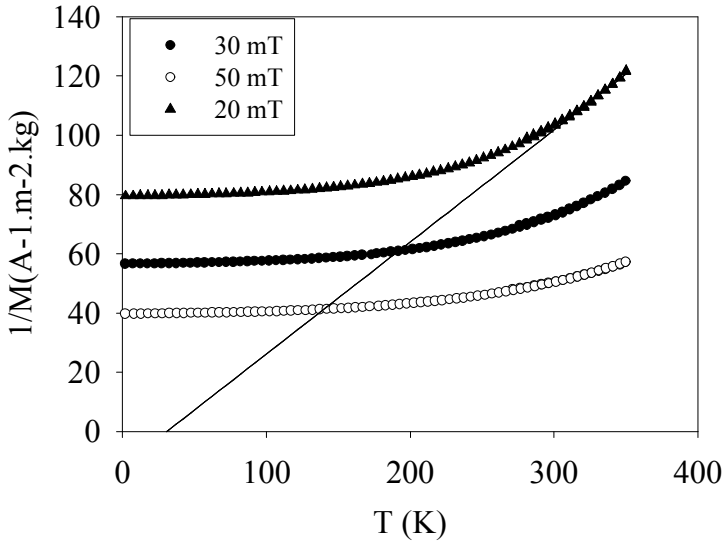

Fig. 9.9: The temperature dependence of the inverse magnetization in different magnetic fields, together with the linear fit above blocking temperature, T_{MAX}, for the CFD2 sample.

As is demonstrated in Fig. 9.8, the T_{MAX} is shifting to the lower values with increasing magnetic field that is expected in systems of nanoparticles, because the potential barrier of a single particle is decreased. In order to estimate the nature of interparticle interactions, the fit of the CW law was applied to the data above T_B (Fig. 9.9). However; such a procedure is not appropriate because it is necessary to use the data measured far above the T_B. Thus temperature dependence of inversed magnetization is not linear above blocking temperature (Fig.9.9), as is expected for SPM systems. But despite the previously mentioned remark about the TB, this nonlinearity could be also caused either by the strong interparticle interactions or the particle size distribution, respectively. The values of T_{MAX} and T_{DIFF} measured in different fields are summarized in Table 9.2.

Table 9.2: Evolution of the blocking temperatures (T_{MAX} and T_{DIFF}) for the CFD2 sample in different magnetic fields.

B (mT)	T_{MAX}	T_{DIFF}
10	263	350
20	251	300
30	246	290
50	236	296
60	233	-

9.3.2 Magnetization isotherms

CFC2, CFC3 and CFD2 samples

The magnetization isotherms of all samples were measured at 2 K, 150 K and 300 K in the magnetic field varying up to 7 T in both polarities (Fig. 9.10-.18, figures in Appendix B). The hysteresis was observed for isotherms measured under the blocking temperature, as expected. The coercivity exhibits symmetric values for both polarities of the applied field. The unhysteretic curves in Langevin scaling were fitted by Langevin function and the average magnetic moment per particle has been determined (Table 9.3). Further measurements of magnetization loops at low temperatures (up to 70 K) has been done and the evolution of coercivity has been examined by the relation valid for non-interacting and randomly oriented systems of particles

$H=H_{c0}(1-(T/T_B)^{1/2})$.

The extrapolated values of H_{c0} and T_B are summarised in Table 9.3. The values of coercivity H_{c0} are almost the same as those measured at 2 K. The values of the T_B are smaller than those obtained from dc and ac susceptibility measurements (T_{MAX}). In general, the maximum of the ZFC curve measured in small field does not correspond to the real blocking temperature, T_B. Otherwise, the particle size distribution causes deviation of the H_c vs $T^{1/2}$ from linear dependence and the real T_B is different than the measured one.

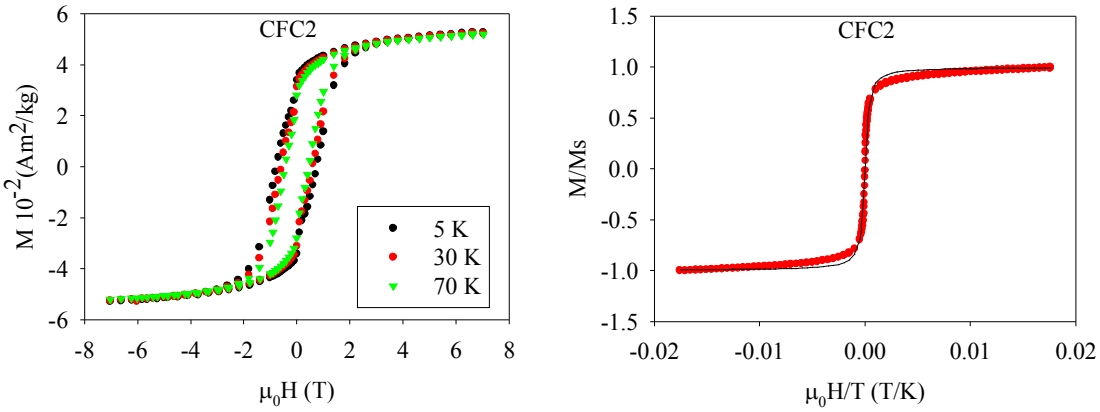

Fig 9.10: CFC3 sample. Left: Magnetization isotherms measured at 5, 30 and 70K up to 7 T, respectively. Right: magnetization isotherm measured at 400 K (red dots) together with the Langevin fit (line).

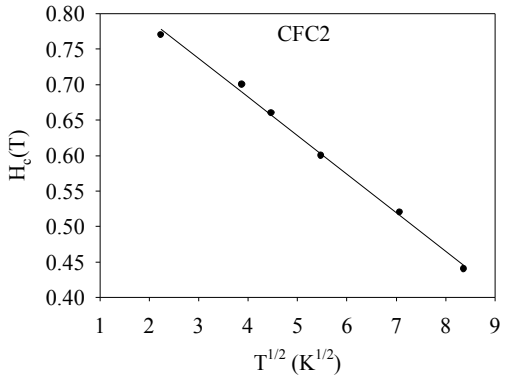

Fig. 9.11: Temperature dependence of the coercivity fields appreciably below the T_B (*Hc* vs. $T^{1/2}$ representation) for the CFC2 sample.

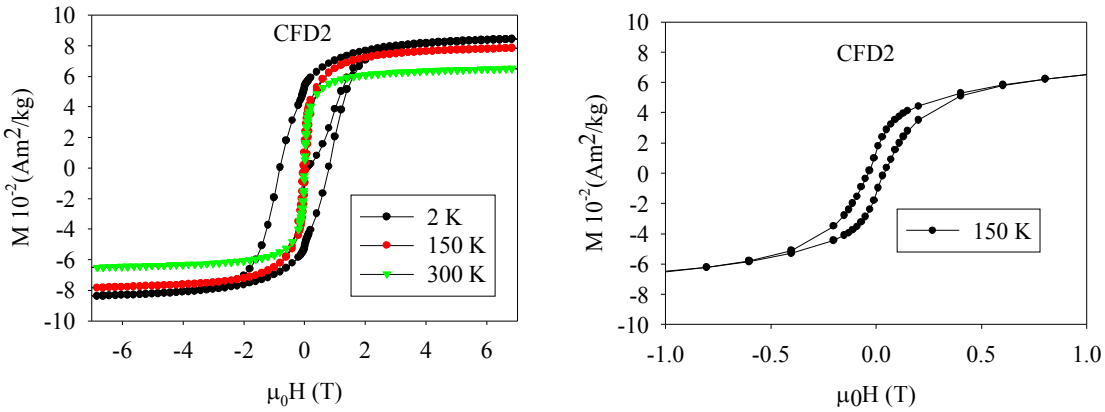

Fig. 9.12: Magnetization isotherms of the CFD2 sample. Left: measured at 2, 150 and 300K up to 7 T, respectively. Right: detail of the magnetization isotherm measured at 150 K.

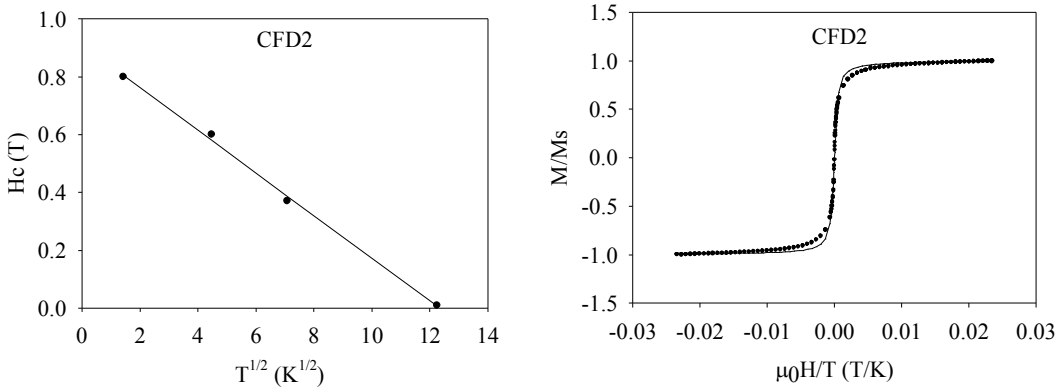

Fig. 9.13: CFD2 sample. Left: the temperature dependence of the coercivity field appreciably below T_B (*Hc* vs.$T^{1/2}$ representation). Right: fit of the Langevin curve (line) to the magnetization isotherm measured at 300 K.

Table 9.3: Summary of the blocking temperatures (T_{MAX} and T_{DIFF}), coercivity values (H_C), saturated magnetization (M_S) and average magnetic moment (μ).

sample	T_{MAX} (K)	T_{DIFF}(K)	T_B^{Hc} (K)	H_C^{2K}(T)	H_C^{300K}(T)	H_{C0}(T)	Ms^{300K} (Am^2/kg)	$\mu\times10^3(\mu_B)$
CFC2	390 (50mT)	400 (50mT)	275	1	-	0.9	-	9.4(400 K)
CFC3	390 (50mT)	400 (50mT)	329	1	0.090	1.1	0.097	8.8(400 K)
CFD2	236 (50mT)	296	152	0.8	0.005	0.91	0.065	6.8(300 K)

9.3.3 Ac susceptibility

Because of the evidence of the interparticle interactions in the samples, the CFD2 sample has been examined by the measurements of the real and imaginary part of ac susceptibility, both in zero and nonzero external magnetic field.

The ac susceptibility in presence of zero external magnetic field was measured at first, the dependence of the frequency logarithm on the inverse T_B determined as the temperature of the cups at the real susceptibility curves was plotted. The data were fitted by the Vogel-Fulcher law, which can be use for evaluation of relaxation phenomena in weakly interacting systems. It has to be remarked that fitting the equation containing three unknown variables doesn't lead to physically interpretational situation so the value of anisotropy constant have been taken from the literature at first and just the T_0 and τ_0 parameters were refined.

We have taken several values of the K_{eff} typical either for bulk cobalt-ferrite or for the nanoparticles of almost similar size in comparison with our particles. Using the bulk value of the anisotropy constant $K_{eff} = 3.5 \times 10^{-2}$ J/m^3, the following parameters were obtained: $\tau_0 = 1.7 \times 10^{-9}$s, $T_0 = 230$ K.

Roca[110] emphasized the effective anisotropy constant for the $CoFe_2O_4$ nanoparticles prepared by decomposition as 2.5 x 10^{-1} J/m^3. This value is not appropriate, because even if the samples were measured in the powder form, the interparticle interactions were neglected when calculating the value from the experimental data. Applying this value in fitting our sample, the resulting values of the fit were $\tau_0 = 6$ x 10^{-22} s (the value approaching the relaxation times of the single spins), $T_0 = 134$ K, which is much lower that the blocking temperature obtained in dc susceptibility measurement.

When the all three parameters were interpolated together, one of the best fits gave the values from which the effective anisotropy constant was calculated as K_{eff}=5.6 x 10^{-2} J/m^3. The value is in the perfect agreement with the values obtained by[111] Naiden et al. for the 11 nm $CoFe_2O_4$ nanoparticles that were obtained by mechanicall alloying. The results are summarized in Table 9.4.

The all values of characteristic variables determined from the fits arising from different approaches are summarized in Table 9.4 but also the question which one is the most real has arisen. Applying the Vogel-Fulcher approach to our sample, a wide interval of effective anisotropy constant values gives the values of relaxation times typical for systems of nanoparticles, which are the same for non-interacting superparamagnets as for the weakly interacting systems. Even if we have strongly interacting system such as super-spin glass, the resulting relaxation times should lie in the same interval and this approach of measuring the ac susceptibility in nonzero field (as shown further) does not give us the information about the interaction strength. The only information is the estimation of the anisotropy constant value.

Keeping the problem from the opposite side, assuming to have strongly interacting system (what would be proved by further measurements), the right values are considered those leading to the slowest relaxation times. Thus the effective anisotropy constant is similar to those for the bulk material (Table 9.4) and demonstrates that the surface effects such as spin canting (where the surface spins are tilted with respect to those in the core and the superspin of the particle is decreased) do not play a significant role.

Table 9.4: Results of the Vogel Fulcher fit for the CFD2 sample. The red rows were obtained by fitting all the 3 parameters and are supposed to represent real physical situation in our sample. The reference to K_{eff} values, used in the 2-parameter fit depicted in the note column.

τ_0	T_0	$K_{eff}.10^{-2}$(J/m^3)	note
1.7 10^{-9}	234	3.5	Bulk value
6.2 10^{-22}	143	25	Roca 2010[110]
7.4 10^{-16}	188	12	Chitasamny[112]
6.2 10^{-11}	224	5	-
5.9 10^{-10}	231	4	-
1.6 10^{-11}	223	5.7	Naiden[111]

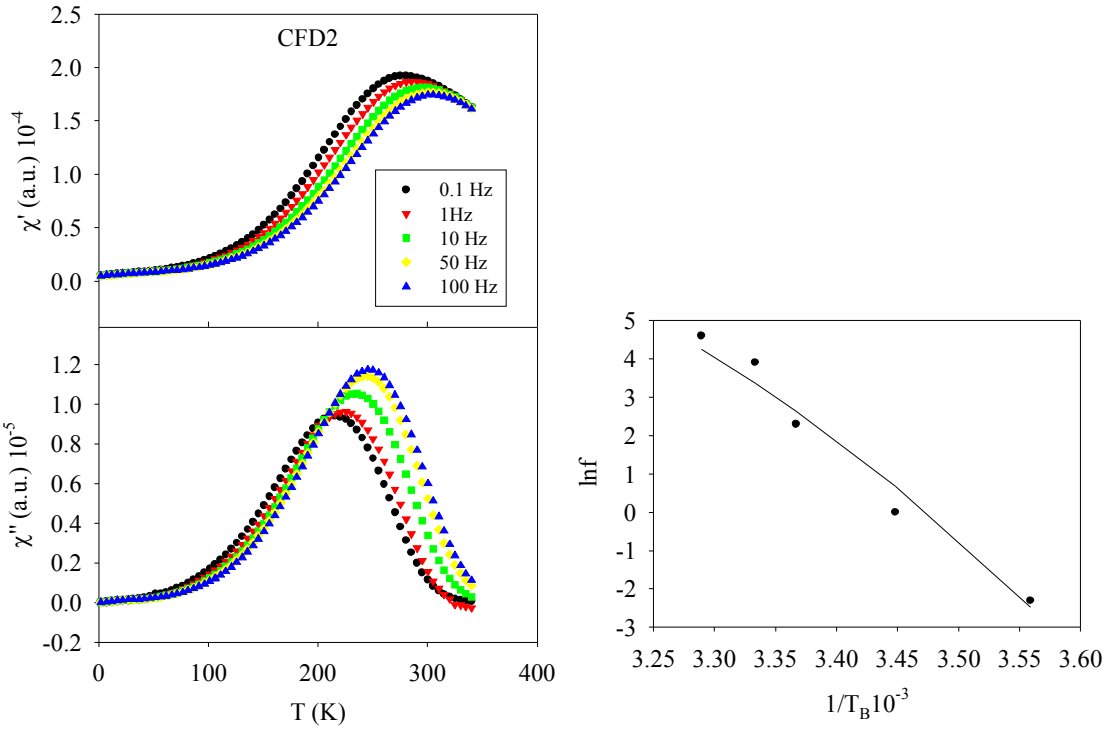

Fig. 9.14: Left: the real and imaginary part of ac susceptibility measured in zero external field. Right: the ln$f$ dependence at inverse blocking temperature, the line is the fit of the Vogel-Fulcher law (last raw in Table 9.4).

To prove that the system behaves as a SSG or SSG-like system, the ac susceptibility curves measured in nonzero magnetic field (Fig. 9.14) were examined. The evolution of the ac susceptibility curve's cusps was investigated using the equation describing the critical phenomena (eq. 2-10). Measuring the susceptibility at constant frequency in different external field (Fig. 9.15), the substituent suppression of the phase transition was observed in field of 0.1 T, as was expected. The resulting values derived from the eq. (2-9) are $T_g = 275$ K, $zv = 5$ and $\tau_0 = 5.6\ 10^{-8}$s; the same as those typical for the super spin glass (or SSG-like) systems (Fig. 9.16).

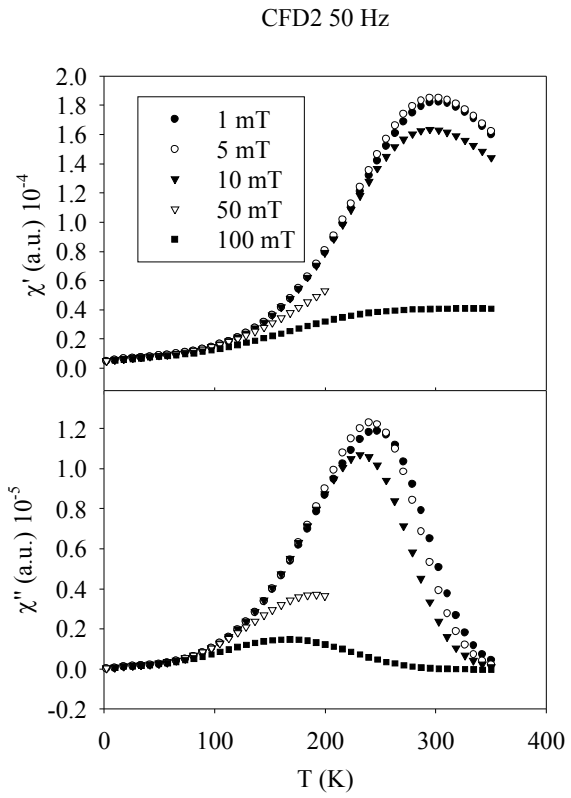

Fig. 9.15: The real and imaginary part of the ac susceptibility measured at 50 Hz in different external magnetic fields.

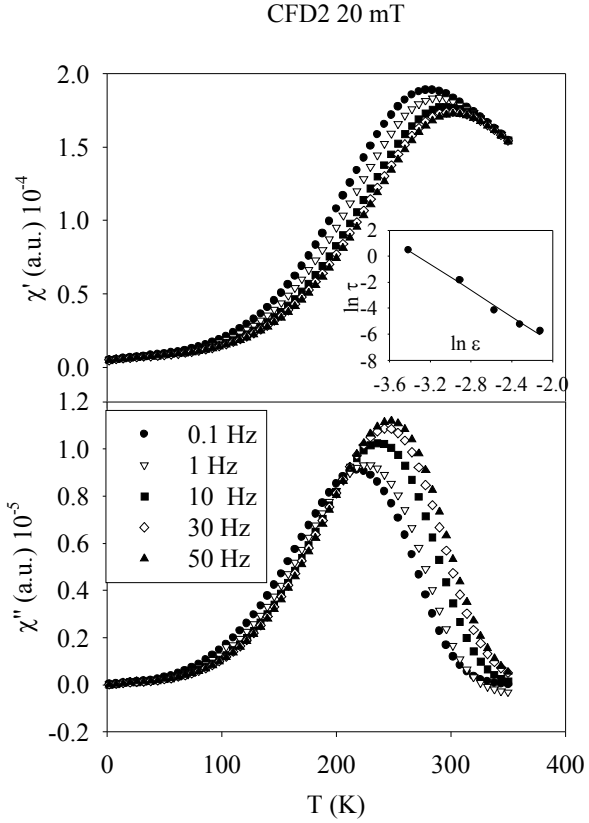

Fig. 9.16: The real and imaginary part of the ac susceptibility measured in 20 mT at different frequencies, the $\ln\tau$ vs. $\ln\varepsilon$ in the inset are fitted by the eq. (2-10).

9.3.4 Aging and memory effects

The last step to have an evidence if the CFC2 sample behaves like the SSG, is to explore the memory and aging effects.

The classical aging experiment has been measured following the so-called thermoremanent protocol. The FC magnetization was measured in field of 10 mT down to 10 K with the 1 hour stops at 150, 80 and 20 K. In each waiting point, the decrease of the magnetization was observed, as expected. Such a decrease follows the Néel-Arrhenius law and is typical for all systems of nanoparticles with interactions. Even in the rather weakly interacting systems, the memory effects are observable at the waiting temperature at continuous reheating, when the step at the magnetization is also observable. This is the case of our sample (Fig. 9.17, red curve).

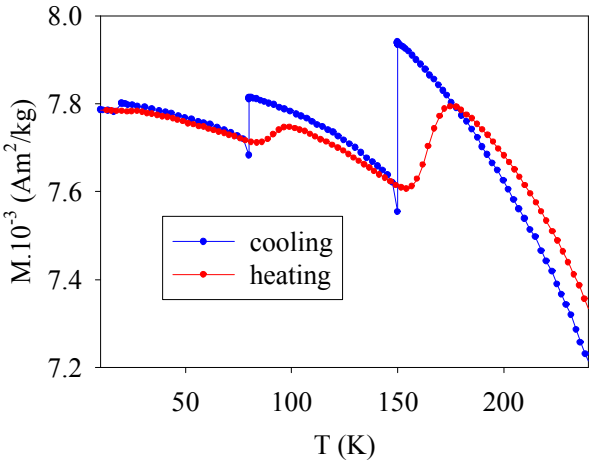

Fig. 9.17: Thermoremanent experiment on the CFD2 sample.

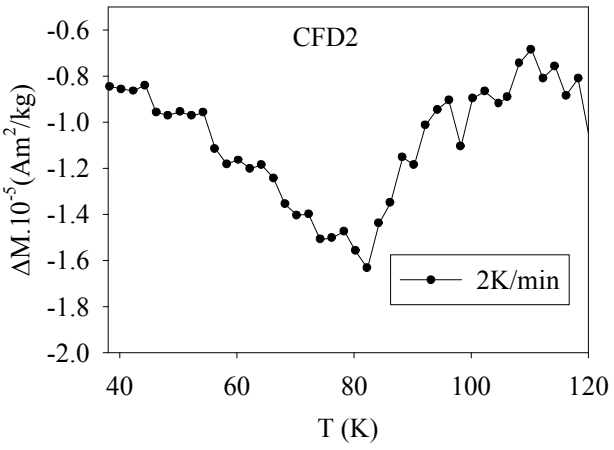

Fig. 9.18: Aging effect for the CFD2 sample.

The typical memory experiment protocol has been done in field of 10 mT. The ZFC curve was measured at first and consequently the sample was cooled down again with the 6 hour stop at 80 K. After subtracting both curves, the cusp at the waiting

temperature has appeared (Fig. 9.18). This is the typical behavior only in the SSG systems, so this experiment gives the final evidence that the system is strongly interacting super-spin glass. The strong interparticle interaction and tendency to create clusters/aggregates complicates the dispersing of the particles and hence the preparation of monolayer of single particles for the MFM imaging.

9.4 Scanning probe microscopy

The several experiments, classical AFM and advanced MFM imaging, were performed with the CFD2 nanoparticles dispersed on the mica substrate. The experiments on the CFC3 nanoparticles has failed, because the attachment to the mice substrate was not sufficient

The topography images captured in TM showed that particles create huge islands of aggregates, but several individual particles are dispersed in between (Fig 9.19, 20). The measurements were complicated many times by moving of individual particles or their sticking on the tip apex.

MFM imaging in lift mode was done in three different configurations to emphasize if there is any detectable magnetic contrast: with non-magnetic probe, magnetic probe on unpolarized sample (sample mounted on the metal stub) and magnetic probe on polarized sample (sample mounted directly on the scanner magnetic holder). Using eq. (6-5), it was estimated from the known values of the particle diameter and magnetic moment together with the values of the tip apex curvature and the tip magnetic moment (determined by the producer), that the field of the holder (0.2 T) is sufficient for stabilizing of magnetic moments of the at least 10 nm nanoparticles.

Phase contrast of captured images has been analysed (in cross-sectional analysis) with respect to the lift scan height (LSH) and the nature of the probe. The phase images were tried to measure in LSH 20, 40, 50, 80 and 100 nm in each configuration, but in many cases, the tip-sample interaction was either strong or the tip had been attached by aggregates and became dirty; thus the representative phase contrast at each LSH for all three configurations has not been obtained. Despite that, it will be shown further that the magnetic probe (at non-magnetized sample) exhibit slightly higher phase contrast than the nonmagnetic probe, for LSH higher than 40 nm. It will be also demonstrated that phase contrast of magnetic probe on magnetized sample (at LSH 80 nm) is significantly higher than that of nonmagnetic probe (LSH = 80 nm) and magnetic probe on non-magnetized sample (LSH 40 and 60 nm). To confirm that we are able to detect magnetic contrast in our MFM experiments, the quantitative analysis of phase contrast has been done.

9.4.1 Nonmagnetic tip

The sample was examined in TM with non-magnetic tip on un-magnetized sample.

The measurements of the negative phase contrast were done in LSH 50, 80 and 100 nm. The analyses of several particles at each image was done, the particle heights and diameters together with the value of the phase contrast are summarized in Table D.1 and shown in Appendix D. The little measurable phase contrast was observed in the LSH = 80 nm for 16 nm particles. Even if the absolute value of the particle diameter is convolution of the real particle size and the curvature of the tip, the phase contrast arising from the long range Van der Waals interactions depends on the tip-surface distance, i.e. the particle heights. Thus there should be no difference of the phase contrast of images arising form the tip curvature (it means that even scanning with the blunt tit does not change the values of phase contrast with respect to the images taken with the sharp tip).

The comparison of the phase images taken with the nonmagnetic and magnetic probes on polarized samples, in the same LSH is demonstrated in Fig 9.24.

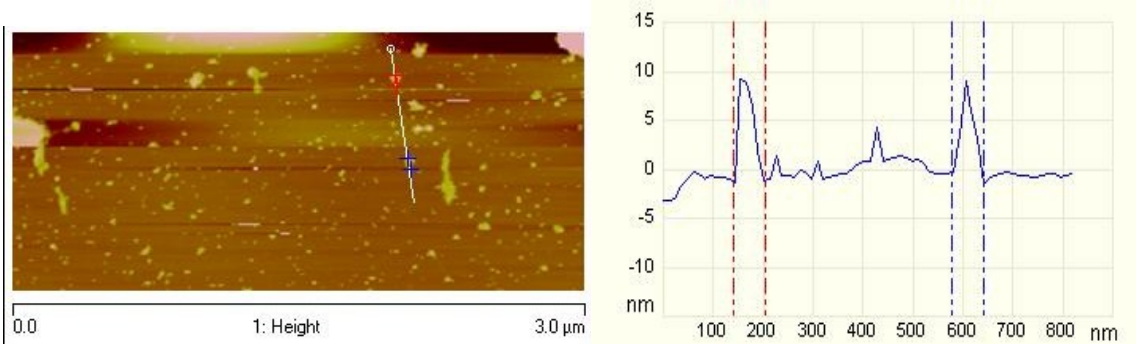

Fig. 9.19: Image of CFD2 sample in TM. Left: topography of the surface. Right: the cross section (represents the line on the topography image). The image was taken with RFESP tip, in TM.

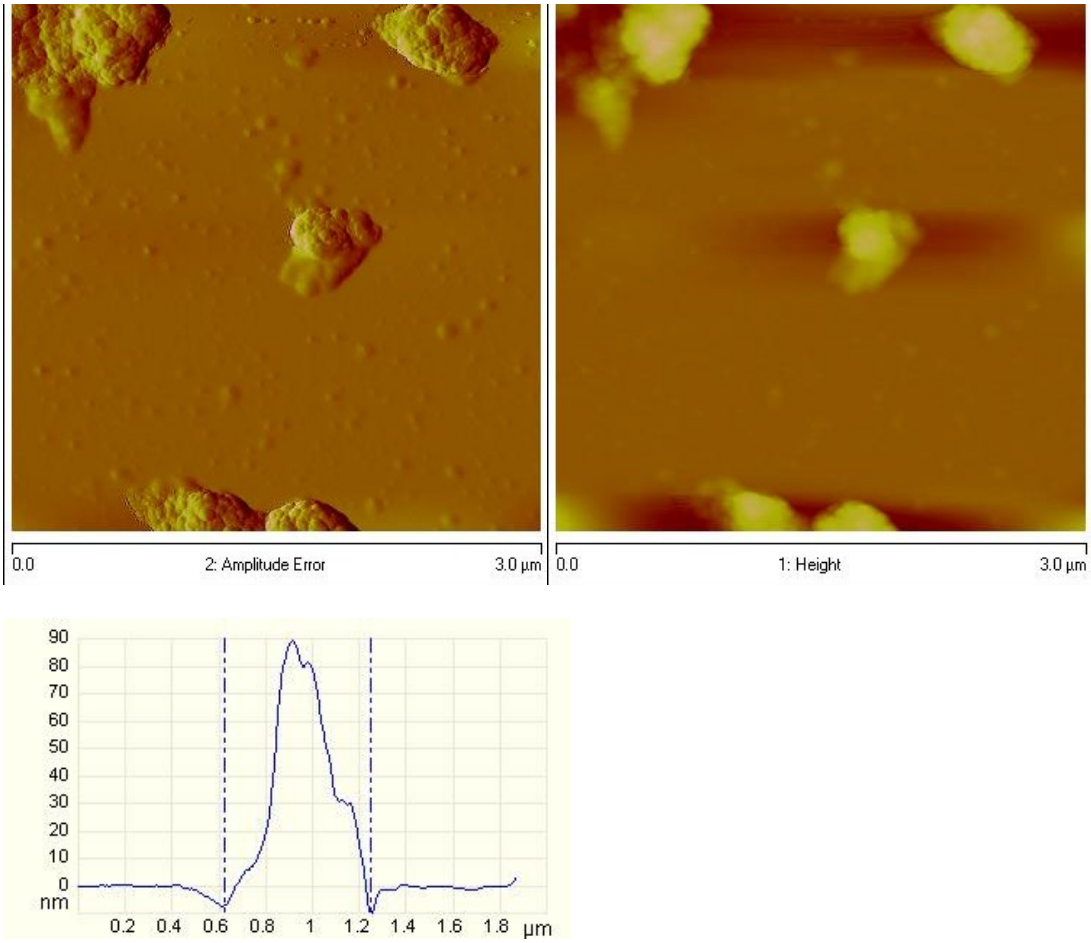

Fig. 9.20: Aggregates of the CFD2 nanoparticles. First row: topography of the sample, amplitude error and the height images. Second row: the cross section of the aggregate. Images were taken with MESP tip in TM.

9.4.2 Magnetic tip on un-magnetized particles (without any external field)

The images were taken with magnetic tip on un-magnetized samples at LSH 20, 40 and 60 nm, results of the quantitative analyses of selected particles are summarized in Table D.1. Comparing the phase contrasts of 6 - 9 nm particles obtained in LSH equal to 40 and 60 nm, respectively, with that of the non-magnetized tip signalise that there is not any significant change in the phase contrast value. Thus it seems that scanning the non-polarized sample with magnetic probe does not lead to the measurable magnetic phase contrast at LSH higher than 40 nm, as was assumed. The example of images taken on un-magnetized sample is depicted in Fig. 9.21.

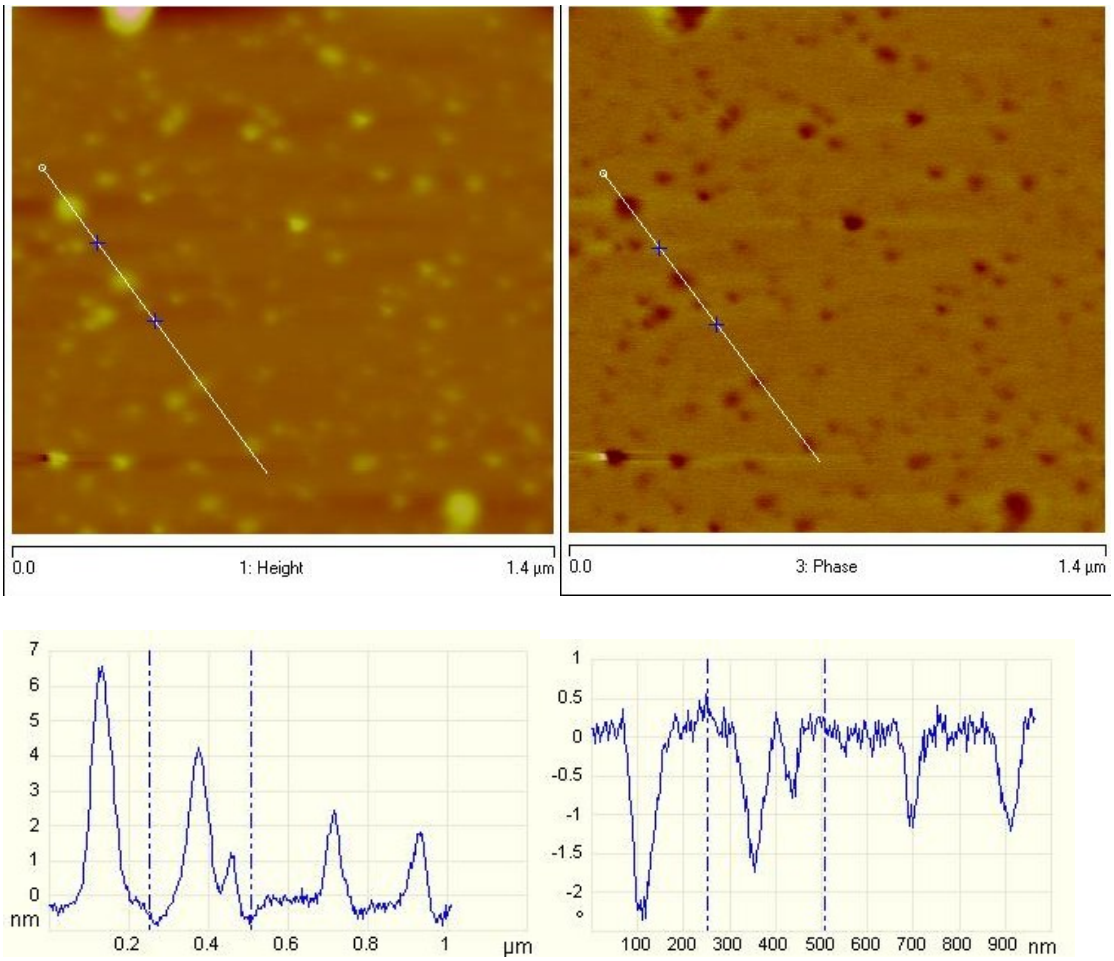

Fig. 9.21: Topography and the magnetic phase image of un-magnetized sample taken in LSH = 20 nm with magnetic tip (MESP). The cross sections (second row) represent the white lines on the images.

9.4.3 Magnetic tip on magnetized particles (external field of 0.2 T)

Only representative image of polarized particles have been taken in LSH= 80 nm (Fig. 9.24). Despite that, comparing the measured phase contrast of particles 6 and 8 nm height with that of 9 nm height taken with non-magnetic tip, the measurable phase contrast which can be attributed to the magnetostatic interaction between tip and the sample has been observed. To prove this, the measurements at lower LSH are required because of the stronger interactions, thus the difference between phase contrast measured with non-magnetized and magnetized probes would be more significant.

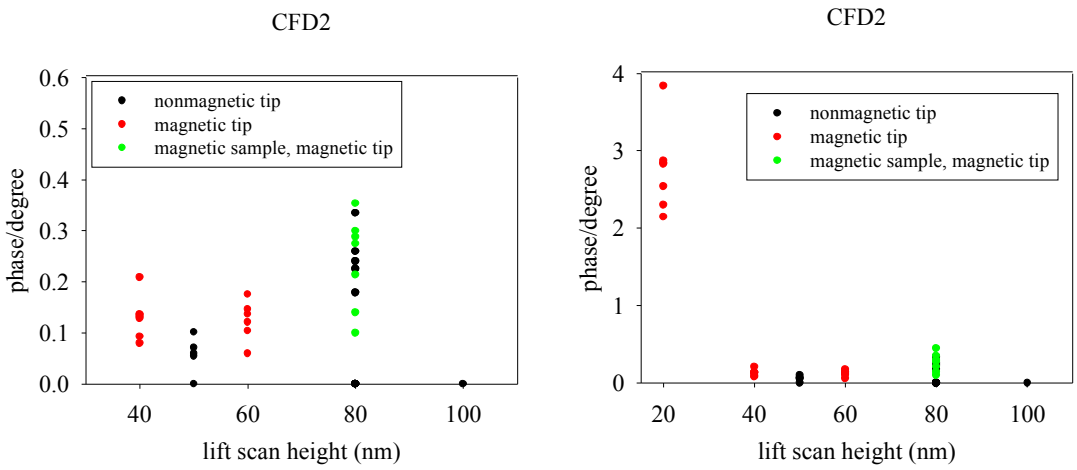

Fig. 9.22: Phase contrast measured with magnetic and non-magnetic tip on polarised and unpolarised particles of different heights in LSH 40, 50, 60, 80 and 100 nm, respectively. The values of the particle heights and phase contrast are summarised in Table D.1.

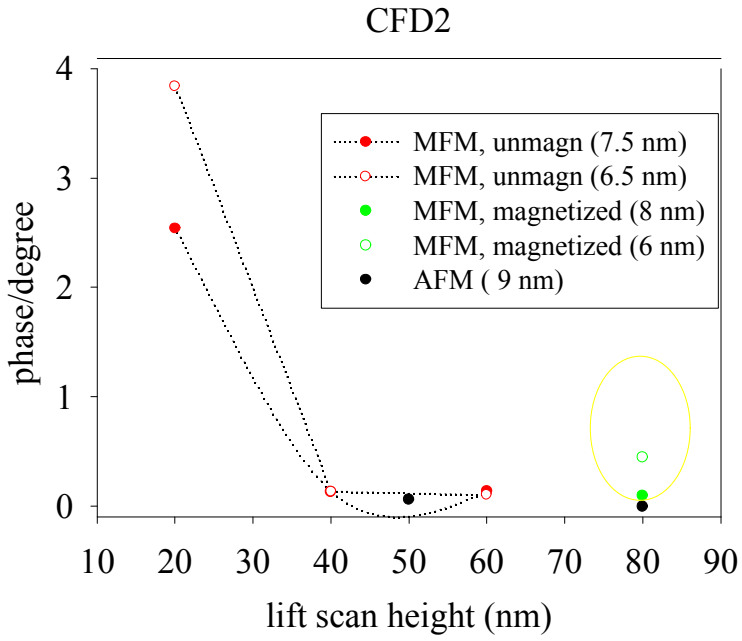

Fig. 9.23: The phase contrast for particles of almost similar heights, taken with magnetic (labelled as MFM) and non-magnetic (AFM) probes. The red spots belong to the magnetized sample, the green ones to the magnetized one. The yellow ellipse highlights the measurable phase contrast for the magnetized sample taken in the MFM mode.

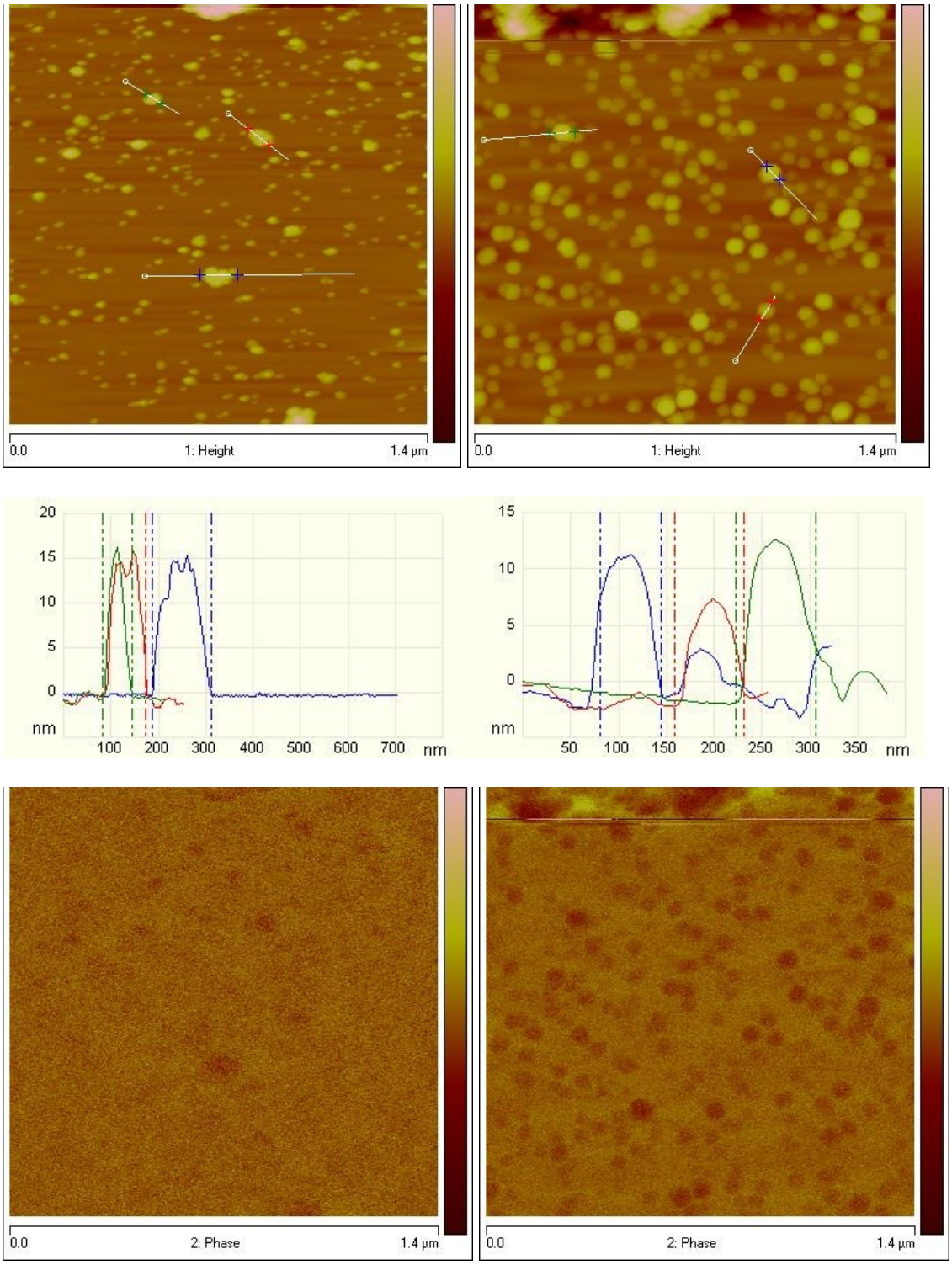

Fig. 9.24: TM height and phase images of CFD2 nanoparticles, obtained in lift-mode with the non-magnetic probe (left) and magnetic probe (right) with presence of external vertically applied magnetic field (0.2 T) together with the cross sections, represented by the line on the topography images, bellow.

9.5 $CoFe_2O_4$ nanoparticles - summary

Four samples of the cobalt-ferrite nanoparticles were prepared by two different methods of preparation, coprecipitation and decomoposition, respectively. The structural properties of particles were mediated through different conditions of preparation, such as the temperature, pH and variety of used metal salts. The elemental composition analysis, PXRD and value of coercivity at low temperature proved together that the samples are really composed of the cobalt-ferrites, not of other iron oxides (with the same, spinel structure). Also the further characterization of particle structure showed that except one sample (CFC1), nanoparticles of all samples are single-crystalline. However, only sample prepared by decomposition exhibit well defined both particle size (8 nm) and shape, respectively. The magnetic properties were studied in term of SPM behavior, the strong interparticles interactions were observed. Thus the CFD2 sample have been examined properly and the evidence of super-spin-glass behavior have been given (with freezing temperature of main fraction of nanoparicles T_f = 235 K, glassy temperature T_g = 275 K, effective anisotropy constant close to the bulk value K_{eff} = 4-5.7×10^{-2} J/m^3 and particle average magnetic moment 6.8 × 10^3 μ_B).

The CFD2 sample was also examined by the AFM and the MFM, with the magnetic and non-magnetic tips, respectively. It has been shown that there is a measurable contrast from the magnetosatic interaction between the tip and the sample, but further precious studies are required. It is necessary to observed increased contrast of the magnetic probe with respect to the non-magnetic probe and to separate contributions of the magnetosatic contrast from the images, however; there is still remaining long way to calculate the value of particle magnetic moment from direct measurement of the magnetostatic interactions, as has been suggested by Agarwal[88].

10 SiO_2_Co(x)_Si(111) thin films and multilayers

10.1 Characterization of the structure

10.1.1 TEM

Two types of the samples were investigated. The first one were the Co layers of various thickness (3, 5 and 10 nm) sputtered on Si(111) surface and covered by 10 nm of SiO_2. The second type was the sandwich layer structure sputtered on Si(111) surface, composed of 10 bi-layers of cobalt and SiO_2. The illustration of both types of the films is depicted in Fig. 10.1. The real structure of selected samples is demonstrated in Fig. 10.2.

It is important to remark that the internal structure of the layers in not compact, such as in the case of the epitaxial or the polycrystalline layers, but is composed of the granules (grains). This statement will be confirmed by further measurements within the thesis, but it has been also observed recently by the HRTEM experiments.

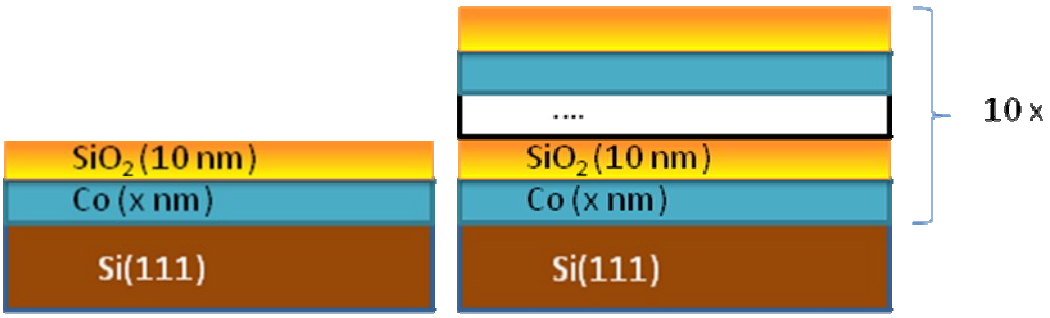

Fig. 10.1: Illustration of the samples; the Co monolayer covered by SiO_2 layer (left) and the sandwich layer composed of 10 Co/SiO_2 double-layers (right). The x represents thickness of the Co layer- 3, 5 and 10 nm.

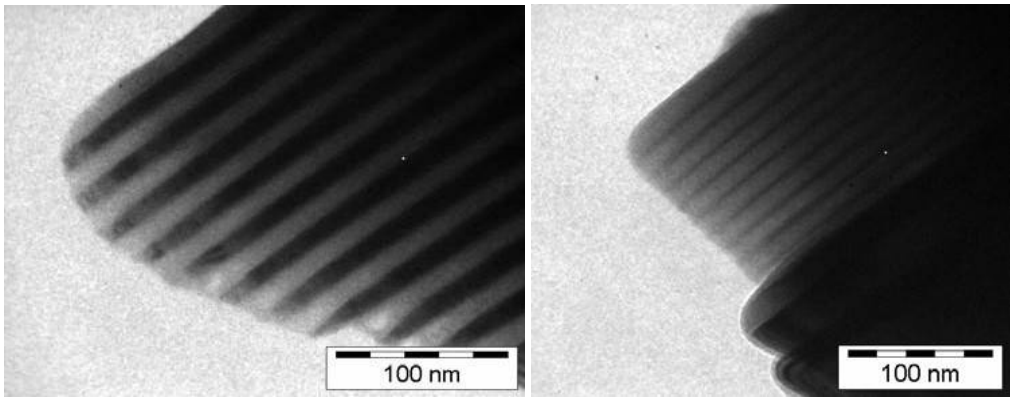

Fig. 10.2: TEM images of the Co(10) (left) and Co(3) (right) samples.

7.1.2. X-ray diffraction

The amount of the crystalline cobalt in the film layers was so small that no diffraction from the cobalt structure was observed. The diffraction experiments in the parallel beam

configuration confirmed only the presence of amorphous SiO_2. Measuring the sample in the Bragg-Brentano geometry configuration, only the peak belonging to the Si (111) has appeared.

However, the HRTEM experiments approved the presence of crystalline *hcp* Co and also the amorphous SiO_2, respectively.

10.1.2 X ray reflectivity

The dependence of the reflected intensity on the angle of incidence was measured for all samples. The critical angle was estimated as the maximal slope of the first oscillation (Table 10.1). The reflectivity of two samples (Co3 and Co5) decreased rapidly as a result of the extremely intensive scattering of incident beam because of the high surface roughness.

The Bragg maxima were present in all reflectivity curves up to 1 degree, but the small oscillations between the Bragg peaks, the Kissing fringes, were not clearly observed. This could be caused by the imperfections in the layer such as non-preciously defined boundaries between them.

The reflectivity curves has been simulated in X'Pert Reflectivity program and compared with the measured curves. The parameters such as thickness, density and roughness of the layers were varied. It has been experimentally observed that the thickness and the density of the first few layers significantly affect the position of the Bragg peaks of the simulated spectra. Increasing the roughness of such a layer, only modulation (minimizing and shifts) of the intensity value was observed. The best simulations of the multilayers leaded to the variance of thickness with respect to that declared by the film grower with discrepancy of 30 - 40 %. This variance could be attributed to systematically varying layer thickness and grain crystallinity of each layer formed during the magnetron sputtering, which cause the systematic error in determination of the layer thickness. In the simulated multilayer's curves, the refined density of layers decreased approaching from the substrate to the surface and was lower than that of the bulk material (example is given in Appendix C). It is not surprising because the granules from which the layers are composed do not fill the space homogenously and completely.

It is obvious that varying of a lot of fitting parameters give us several simulated spectra that fit to the measured data very well (with the same error). Such examples are presented in Appendix C, together with the evolution of the simulated spectra with increasing number of fitting parameters.

In this chapter, only the results obtained from the simulations of the reflectivity curves (Fig. 10.3- 10.5) that seem to be the most physically relevant are presented. The discrepancies in simulated and measured reflectivity curves are probably given by lack of possibility to simulate the imperfections on the boundaries and the huge number of

fitted parameters. There is also, highly probably, some degree of diffusion of the one (Co) layer to another (SiO_2) layer, which was recently suggested by HRTEM experiments.

Table 10.1: Parameters of the reflectivity curves. t_{Co} is the nominal thickness of the Co layer, r_{AFM} is the roughness of the SiO_2 layer measured by AFM, α_c is the critical angle, t_{SiO2}^{1} and t_{Co}^{1} thickness of the first SiO_2 and Cobalt layers, r_{SiO2}^{1} is the roughness of the first (capping SiO_2) layer.

sample	t_{Co} (nm)	r_{AFM} (nm)	α_c (°)	t_{SiO2}^{1} (nm)	t_{Co}^{1} (nm)	r_{SiO2}^{1} (nm)
Co3	3	0.405	0.27	13.48	3.36	1.47
Co5	5	0.424	-	-	-	-
Co10	10	0.752	-	-	-	-
Co(3)	3 (10x)	1.020	0.25	9.7	3.6	1.9
Co(5)	5 (10x)	1.450	0.25	12.2	5.9	1.34
Co(10)	10 (10x)	1.490	0.26	11.4	11.9	1.10

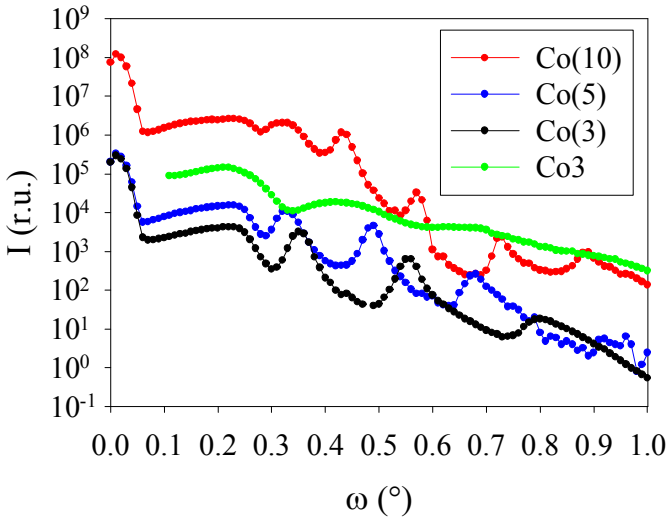

Fig. 10.3: Measured reflectivity curves (the dependence of the relative intensity on the angle of incidence).

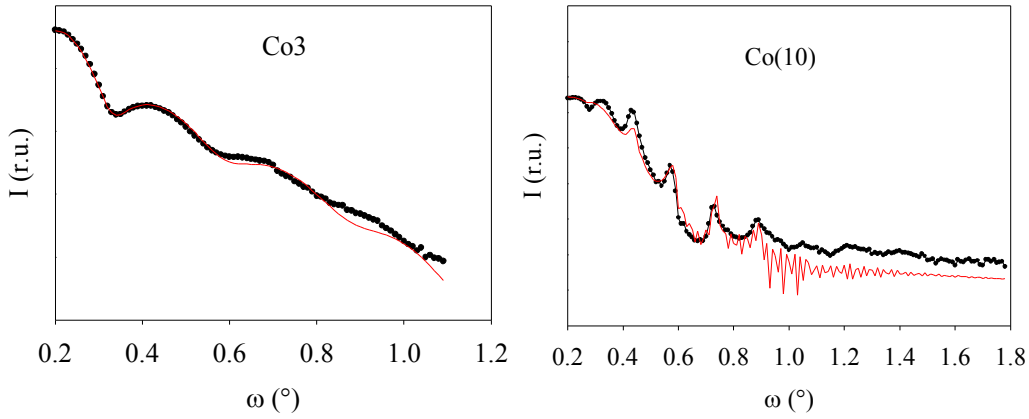

Fig. 10.4 and 10.5: The measured (black) and simulated reflectivity curves (red line) for the Co3 and Co(10) samples, respectively.

10.2 In-plain magnetic measurements

The magnetic properties of samples were measured in three in-plain film orientations. The applied field was either parallel with the edges of the film (labeled as x, y axis) or with the diagonal of the film (labelled as cross). Because the films are thin, it has been assumed at first that the easy axis of magnetization lies in plain. This can be proved by measuring the magnetic properties in different film orientations with respect to the applied field.

Because the films are supposed to have granular structure, the behavior such as in the case of interacting nanoparticles is expected; thus all experiments are comment similar to the description common for such a system.

10.2.1 Temperature dependence of magnetization up to 350 K

Temperature dependence of magnetization was measured in small fields up to 350 K. The applied field was not the same in all cases because the intensity of the signal was low and the external field had to be increased to obtain values of magnetization within a detectable limit. The ZFC-FC magnetization curves exhibit the similar features for the all three orientations in which the films were magnetized, as is demonstrated in Fig. 10.6 and in Appendix D. This kind of behavior is expected and could be explained as follows: the magnetic moments of the granules (nanoparticles) lying in film plain rotate coherently in applied external magnetic field. This rotation does not depend on the direction of the film easy axis of magnetization with respect to the easy axis of the particle, but only on an orientation in which the films are magnetized. This behavior is consistent with the presumption that the negligible texture of the film causes that there is no unique easy axis of magnetization.

The temperatures of coinciding points of both curves, labelled as T_{DIFF}, are summarized in Table 10.2. All samples exhibit almost the same features; there is no significant the evolution of the T_{DIFF}. The only exception could be the Co3 film, in which the T_{DIFF} is at

least of 100 K lower than that for the rest of the films. This behavior could be explained either as a consequence of different grain structure arising from its thickness (because the Co3 sample is the thinnest one) or just the artefact of the measurement (high scatter of the measured data).

Because the shape of the ZFC curves do not indicates presence of any maximum, which is expected if the main part of the particles is in the blocked state, and also the T_{DIFF} are close to the maximal temperature reached in the experiment, it could be assumed that the real blocking temperature lies at higher temperature than is the value observed in this experiment. The explanation of this presumption is following: if the ZFC-FC curves are measured in the temperature range under the real blocking temperature, the unrealistic T_{DIFF} is observed at (or close to) the maximal temperature reached in the experiment. To obtain the real temperature of bifurcation, T_{DIFF}, the FC curve has to be measured after heating the sample above this temperature. Thus it is required to perform the experiment at higher temperatures.

Table 10.2: The blocking temperature of samples heated up to 350 and 500 K, respectively.

sample	T_{DIFF} (K)	T_{DIFF}^{500K} (K)
Co3	245 (20mT)	450 (20 mT)
Co5	340(50mT)	-
Co10	350(20mT)	400 (10 mT)
Co(3)	335 (20mT)	-
Co(5)	340 (20mT)	-
Co(10)	310 (50mT)	460 (50 mT)

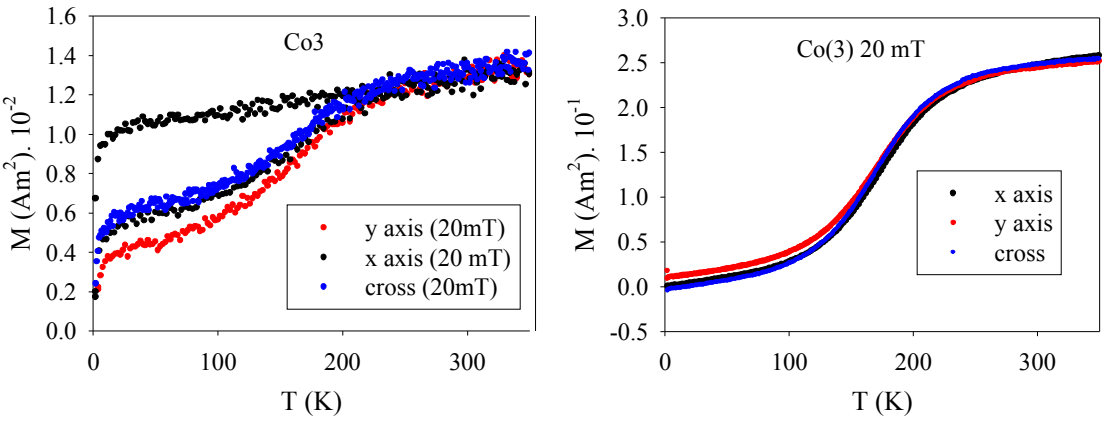

Fig. 10.6: The ZFC-FC curves measured in different orientations of the Co3 and Co(3) samples.

10.2.2 Temperature dependence of magnetization up to high temperatures

The high temperature magnetization measurements were performed on Co3, Co10 and Co(3) samples. Heating the samples up to 500 K, the temperature of bifurcation, T_{DIFF} is shifted to the higher values (Table 10.2) and the maximum on the ZFC curve appears (the curves measured bellow 350 K have increasing tendency with no significant maximum).

Because of the presence of the maximum at the ZFC curves, one can guess that the measured temperature of bifurcation is the real one, which can be proved by measuring the magnetization isotherms above the T_{DIFF} (that are supposed to be un-hysteretic).

If the T_{DIFF} is not the real temperature of bifurcation, its shifting to the higher values can be explain by following idea. It is well known that the blocking temperature of (non)-interacting nanoparticles increases with increasing particle size, because the energy barrier of a single nanoparticle (given by E_A) is also increased and it is more difficult to be overcome by the thermal fluctuations. That is the reason why the increase of T_{DIFF} after measuring the samples in higher temperatures could be explained by the irreversible change of the cobalt layer structure due to particle aggregation/sintering.

The last consideration arises from the possibility that the real temperature of bifurcation still lies at temperatures higher than 500 K, thus the ZFC-FC curves have to be measured up to even higher temperatures.

To evaluate the real T_{DIFF} and to demonstrate the sintering mechanism by heating the sample up to the higher temperatures, temperature dependence of magnetization in Co10 and Co(10) samples were measured up to 700 K and 600 K, respectively. In both ZFC curves (Fig. 10.7, 8) the second maximum, which can be attributed to the already sintered granules, has appeared. As a consequence, the T_{DIFF} was shifted above 600 K. The conclusion arising from this experiment could be following: if the real T_{DIFF} lies above 500 K, it is not possible to measure it because by heating of the film at least at the 600 K, the sintering of granules comes into the play and the T_{DIFF} of virgin (unheated and non-magnetized) samples shifts up to higher values. The Co3 and Co10 samples were also examined with respect to the evolution of T_{DIFF} with applied field. Measurements of the temperature dependences of magnetization in different applied fields (Fig. 10.8, Table 10.3) demonstrate the shift of the T_{DIFF} to the lower values with increasing external field, as expected in the system of SPM-like nanoparticles.

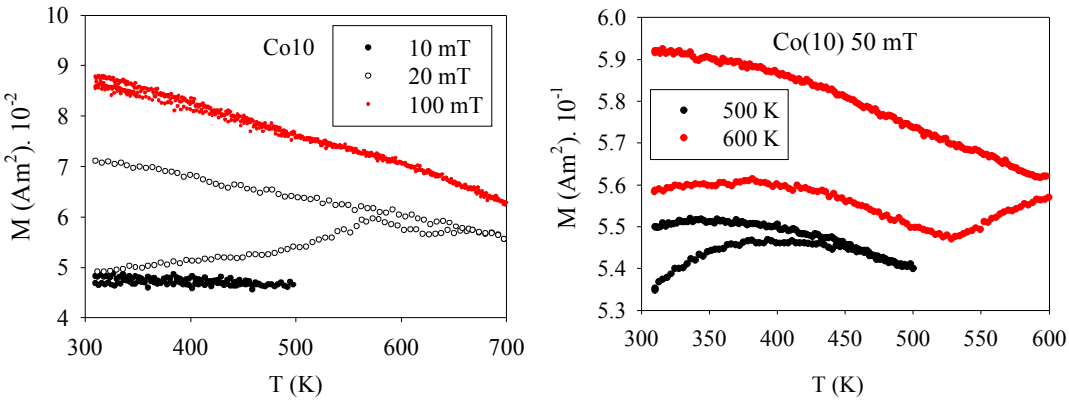

Fig. 10.7: The ZFC-FC curves for Co10 sample measured up to 500 and 700 K.

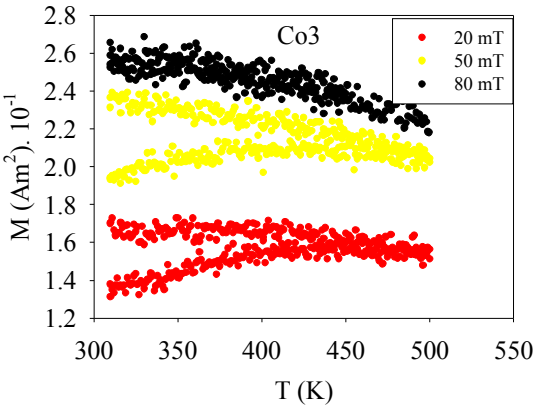

Fig. 10.8: Shift of the T_{DIFF} in different fields, Co3 sample.

Table 10.3: Nominal values of the T_{DIFF} for the ZFC-FC curves measured in different fields (Co3 sample).

B (mT)	T_{DIFF} (K) (heated up to 500K)
20	500
50	450
80	330

10.2.3 Magnetization isotherms

The raw magnetization curves exhibit the presence of the diamagnetic contribution (shown in Appendix D), especially at very low temperatures. This diamagnetic contribution was interpolated by the liner function and subtracted finally from the magnetization loops.

Measuring the magnetization isotherms under the temperature T_{DIFF}, the hysteresis was observed (at 2, 10, 50, 150 and 200 K, respectively). The coercivity shows symmetric values for both polarities of the applied field. The values of coercivity for all samples measured at different temperatures are summarized in Table 10.4. As well as in the paper by Li and Wang[47], the coercivity decreases with increasing thickness of the layer, both for single and multi-layer films (Table 10.4, low temperature measurements).

Even if it was already demonstrated by measuring the temperature dependencies of the magnetization, the films probably do not exhibit the uniaxial easy axis of the magnetization; both the shape of the magnetization isotherms and the coercivity values are slightly changing depending on the direction in which the films are magnetized. The orientation of the field during the magnetron sputtering was either parallel to x or y axis, thus one of the film 'easy axis' of magnetization also lies in one of these directions. This can be emphasized from the shape of the magnetization isotherms, because especially those isotherms measured in x and y directions do not fit together, suggesting one of them is closer to the characteristic easy axis (Fig. 10.9, Appendix D). Also comparing separately the data for each sample measured in different in-plain orientations, the absolute value of coercivity measured at constant temperature does not change very much (Table 10.4).

The value of coercivity for loops measured at room temperature (300 K) is very little (from 1 to 8 mT), the films are magnetically soft. This is undesired in case of magnetic storage media in which the high resistance against an applied external field is required, but excellent for the low hysteresis loss devices (such as GHz resonators). The magnetization loops were also measured above temperature of diffurcation, after measuring the ZFC-FC curves up to 500 K. Such curves should be unhysteretic, but the coercivity values of our magnetization isotherms increases in comparison with those measured at 300 K. It has been assumed in the previous paragraph that the T_{DIFF} determined from the ZFC-FC curves measured up to 500 K is either the real temperature of bifurcation, $T_{DIFF;}$ belonging to the sintered particles or such as in the case of the ZFC-FC curves measured up to 350, lying above the 500 K. If the sintering occurs, the coercivity values rises with respect to the values obtained in the virgin samples and also the size of the particles in heated films should be higher than that of the virgin samples. Thus we can conclude, regarding our results, that the partial sintering of the particles after heating the samples up to 500 K has happened (Table 10.4).

The size of the particles can be calculated from their magnetic moment, which can be determined by the fitting of the unhysteretic magnetization isotherms. It is not relevant to use this solution for our samples, because all measured magnetization loops exhibit hysteresis.

Magnetization isotherms of Co10 sample were measured after heating the sample up to 700 K, coercivity values of loops measured at different temperatures are summarized in

Table 10.5. The coercivity at 600 K is the same as that of 500 K, 18 mT, suggesting further sintering of particles after heating up to 600 K (that has been also demonstrated by the ZFC-FC measurements).

Table 10.4: Coercivity of loops measured at 2, 10, 300 and 500 K in different orientations of sample, respectively.

	$H_c^{2\,K}$ (mT)			$H_c^{10\,K}$ (mT)			$H_c^{300\,K}$ (mT)			$H_c^{500\,K}$ (mT)
sample	X axis	Y axis	cross	X axis	Y axis	cross	X axis	Y axis	cross	
Co3	175	170	150	-	-	-	35	3.0	1.0	13
Co5	-	-	-	38	-	-	8	-	-	-
Co10	45	49	57	-	-	-	6	7.0	5.5	18
Co(3)	129	133	133	-	-	-	1	6.5	5.0	-
Co(5)	-	120	115	100	100	100	4	4.0	4.0	-
Co(10)	90	86	98	-	-	80	8	8.0	7.5	6

Table 10.5: The values of coercivity for magnetization loops of Co(10) sample, measured at different temperature after heating up to 500 (rows 1-3) and 700 K (row 4).

T (K)	H_c (mT)
380	34
400	30
500	18
600	18

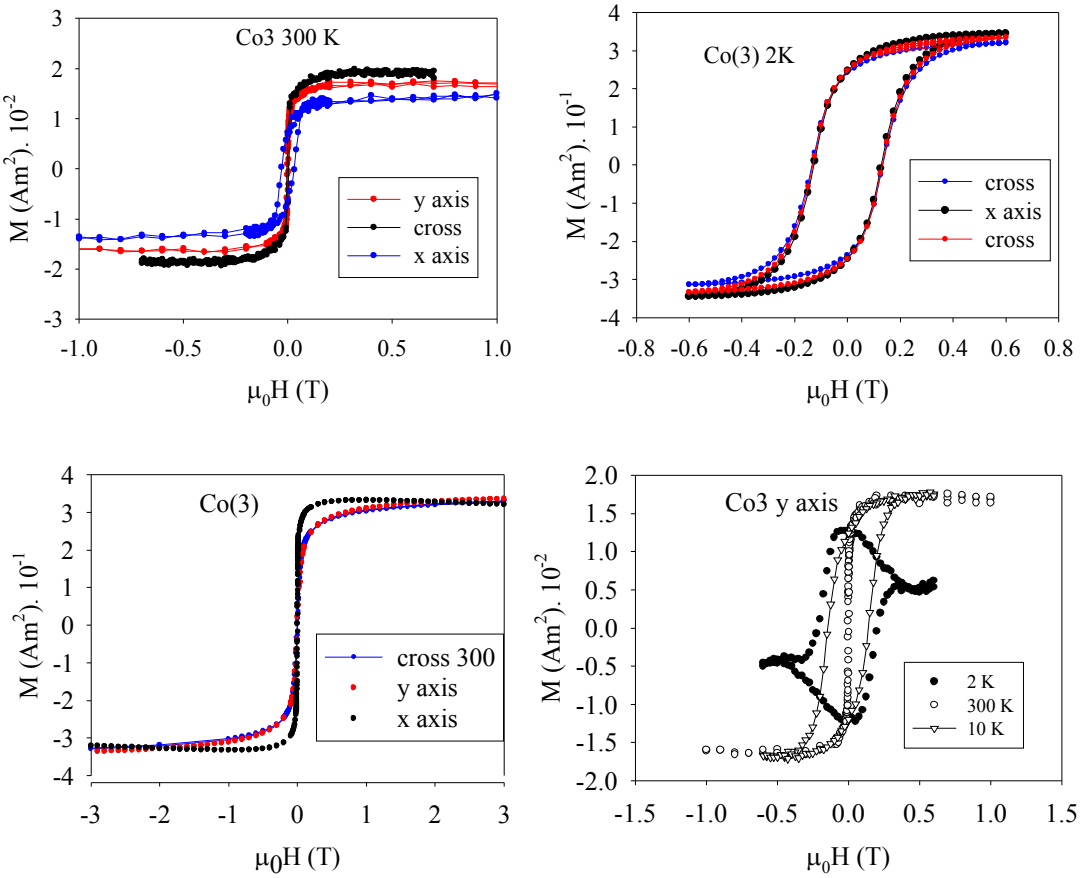

Fig. 10.9: Magnetization isotherms of the Co3 and Co(3) samples, measured in different sample orientations at different temperatures.

10.2.4 Calculation of the granules size from the magnetic measurements data

Because the measurement of the XRD data failed, which would give us the estimation of the individual size of the crystallites in films, the particle diameters were estimated from the values of the average magnetic moments. As was already mentioned, applying the Langevin function to our data is not relevant because of the little hysteresis at magnetization isotherms. Despite that, the procedure was used to emphasize the particle magnetic moment because of reason to have the estimation of the order of magnitude, at least. The mean values of magnetic moment per particle (approximately 10^4 μ_B) calculated from magnetizations curves measured at 300 and 500 K are summarized in Table 10.5. The information which is needed for calculation of particle diameter are the value of magnetic moment per cobalt atom in bulk, μ_{Co}, volume of the unit cell V_{uc} and number of cobalt atoms per unit cell, A_{uc}. Now if the value of magnetic moment per particle μ is known, it is easy to calculate the number of atoms in particle N_p, $N_p = \mu / \mu_{Co}$ and number of unit cell N_{uc}, $N_{uc}=N_p/A_{uc}$. Finally, the particle volume V_p, is given as $V_p=N_{uc}.V_{uc}$ (for a simplicity assuming the spherical shape of particles). The particle diameters obtained from this calculation are summarized in Table 10.5, but still keeping in mind that the result is roughly estimative.

Since the estimation of the particle size is available, the values of effective anisotropy energy constant, K_{eff} can be estimated from the blocking temperatures, $T_{DIFF.}$ The use of the formula valid for non-interacting systems of nanoparticles (eq. (2-3)) gives the values of K_{eff} in interval 4.2 - 9.6×10^2 J/m^3. Taking the results from the literature, values of anisotropy constant for Co clusters (4 - 15 layers of cobalt) lies in interval 1×10^2 - 1×10^3 J/m[112]. The bulk value is approximately (2.7×10^5 J/cm^3)[112].

Even if the calculations were not based on the 100 % relevant data, we still expect that at least, the order of the magnitude of calculated diameters and effective anisotropy constants is still right; thus it could be said that there is the discrepancy between calculated and the bulk values of effective anisotropy constant which still signalises the presence of strong surface contribution to magnetocrystalline anisotropy of a single particle (grain). This conclusion seems to be logic, because if the layers are composed of particles that are touching each other, a significant inter-particle interaction is expected (as in the case of densely packed nanoparticles, Chap. 9). So if there is some inter-particle interaction, the surface anisotropy constant is decreased that is consistent with the rough estimations of anisotropy constant values (for effects of the interparticle interactions on the effective anisotropy of the particle, look at Chap. 2).

Table 10.5: The calculated magnetic moments μ at 300 K and 500 K, particle diameter *d*, effective anisotropy constant calculated from the blocking temperature.

sample	$\mu\times10^3$ (μ_B) at 300 K	d (nm)	$K_{eff}^{TB}\times10^2$ (J/m^3)	$\mu\times10^3$ (μ_B) at 500 K
Co3	**65**	**69**	**5.02**	**44**
Co5	**108**	**81**	**4.20**	**-**
Co10	**85**	**75**	**5.49**	**48**
Co(3)	**75**	**72**	**5.95**	**-**
Co(5)	**47**	**61**	**9.64**	**-**
Co(10)	**54**	**64**	**7.65**	**63 (450 K)**

10.3 Perpendicular magnetization measurements

The magnetic properties of some of the thin films were also measured in orientation perpendicular to the film plane. The evolution of the temperature and field dependence of magnetization curves signalises that the easy axis our films lies in plain, as expected.

10.3.1 Temperature dependence of magnetization

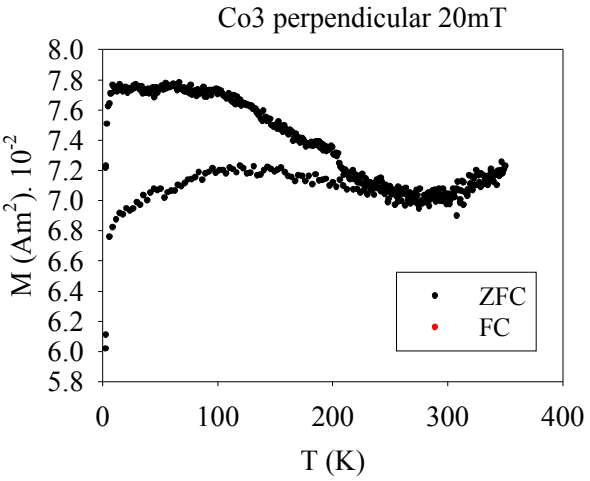

Fig. 10.10: The ZFC-FC curves for the Co3 sample measured in perpendicular orientation.

The shift of T_{DIFF} with respect to the values measured in parallel film orientation is around 10 K (up to higher values). This behavior can be attributed to the demagnetising field arising from the shape of the sample. If the film plane is parallel to the applied field, the demagnetising factor is zero and the effective field acting on the sample is almost the same as the applied one. If the film is placed perpendicularly to the external field, the demagnetising factor rises and the effective field acting on the sample is much lower, which causes the shift of apparent blocking temperature up to higher values.

There could be also another contribution leading to shifting of the T_{DIFF} to higher values, which has an origin in the non-spherical particle shape. The explanation of such a case is following: the increase of the blocking temperature is the consequence of the increase of particle energy barrier (given by particle anisotropy energy E_A). If the particles have non-spherical shape, symmetry of particle anisotropy energy usually follows the shape symmetry of the particle, so the easy and hard axis of magnetization for ellipsoidal particle would be parallel and perpendicular to the longer axis, respectively. Magnetizing the sample, which is composed of aligned particles, in a direction of their hard axis of magnetization, will increase the blocking temperature in comparison with the experiment in which the particles are magnetized in a direction of easy axis. Following these considerations, if there is such a contribution, we can guess that our particles are elongated in the direction of film plane and have ellipsoidal or plate symmetry.

The example of the ZFC-FC curve for sample measured in perpendicular orientation is demonstrated in Fig. 10.10, the other results could be found in the Appendix D.

10.3.2 Magnetization isotherms

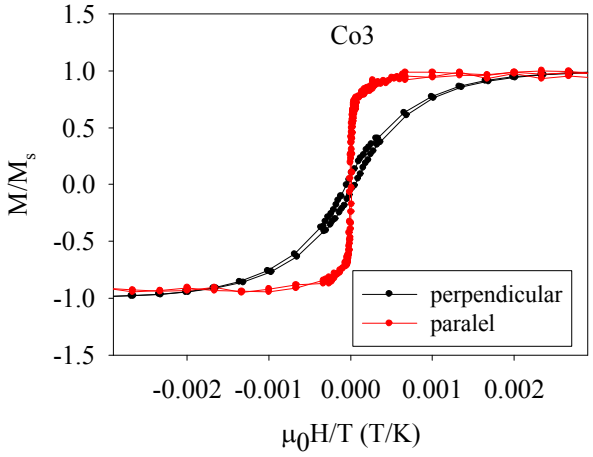

Fig. 10.11: Magnetization isotherms for the Co3 sample, measured in perpendicular and parallel orientations.

The field dependence of magnetization was measured at 2, 10 and 300 K, respectively. The coercivity values are higher than those measured at the same temperature in parallel film orientation and are symmetric for both polarities of applied field (Table 10.6). Such an increase in coercivity arises again in the demagnetising field which decreases the effective magnetic field acting on the sample in comparison with that of the parallel film orientation. The inclination of measured data (as is demonstrated in Fig. 10.11) from the typical course of M(B) curve measured along hardy axis of magnetization (linear function crossing zero) is probably caused by the superposition of additional paramagnetic-like contribution

Table 10.6: Coercivity, H_C and the blocking temperature, T_B of selected films measured in perpendicular orientation at different temperature.

sample	T_B (K)	$H_c^{10\,K}$ (mT)	H_c^{300K} (mT)
Co3	230	190	15
Co(3)	>350	201	0.6
Co(5)	>350	30	14
Co(10)	>350	-	25

10.4 Torsion magnetometry

The torsion magnetometry definitely confirmed the assumption that the easy axis of the magnetization lies in film plane.

The experiments with the two characteristic samples, multilayer Co(10) sample and single layer Co10 sample, were done. The dependence of the torque on the angular displacement from the direction of the applied field was measured. The films with the perpendicular easy axis of magnetization reach the maximum (or minimum, depending on the absolute value of magnetization) of the signal when the easy axis is oriented perpendicular to the applied field; thus the film plane is parallel to the external field direction (displacement of 45 and 135 degrees); whereas the in plain magnetized films reaches the maximal (minimal) magnetization at 0, 180 and 360 degrees.

Co10 thin film

Both the dependence of the torque at the angle of displacement in zero and nonzero applied field were measured. Because the signal reached lower edge of the magnetometer sensitivity, the curve measured in zero field was subtracted from that one measured in field, to get rid of the gravitational force contribution acting on the sample during rotation.

It is clear (Fig. 10.12) that the maximum and minima of the curve, respectively, are slightly distorted from those significant for the film with in plain easy axis of magnetization. There are two reasons of such a behavior: either the easy axis of magnetization is slightly tilted from the film plain to the perpendicular direction (to the film plane) or the film plane is not parallel with the substrate/sample holder.

The non-symmetric shape of the curve is an artefact caused by the sample holder-there is not the same mechanical reaction of both piezoelectric pins to the same torsion.

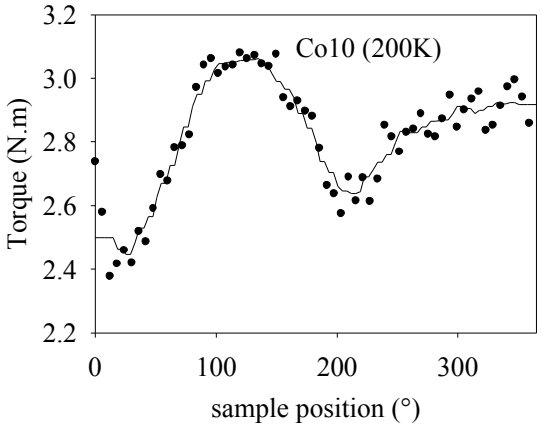

Fig. 10.12: The dependence of torque on the sample position for the Co10 sample. Minimum of the curve lies at 20 and 214 K, maximum is at 125 and 310 K. The black line is the median of the measured data.

Co(10)

The angular dependence of the torque of this sample (Fig. 10.13) is a nice demonstration of the film with the in plain anisotropy (regardless the small distortion of the easy axis from the film plane). It is obvious that the torque value depends on the strength of the applied field. The non-symmetric shape is cause by non-homogenous reaction of the chip.

The magnetization isotherms were measured at 167 º and 92º at 300 and 200 K, respectively in the field up to 1, 2, and 3 T. The nature of those ones measured at 1 T follows the typical magnetization curves of the hard and easy axis of magnetization, respectively (Fig 10.14), regardless the contribution of demagnetising factor. Those ones measured up to 2 and 3 T, respectively, posses the strong diamagnetic (linear) contribution (Appendix C). As has been claimed in Chap.3, magnetocrystalline anisotropy of the thin film is proportional to the area enclosed by the curves measured along the easy and hard axis, respectively. The second crucial requirement is to measure the curves far above the T_C or T_B (Chap. 3). This was not fulfilled in this case, because as was already explained, the T_B lies at higher temperature than is the maximum temperature reached in the experiment. Thus the MAE has not been calculated.

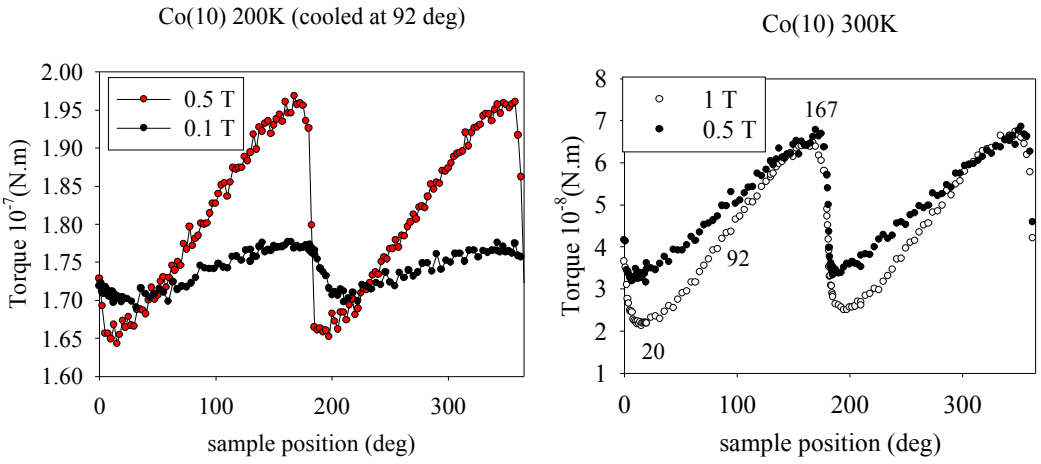

Fig. 10.13: The dependence of torque at the sample position measured at 200 K (left) and 300 K (right).

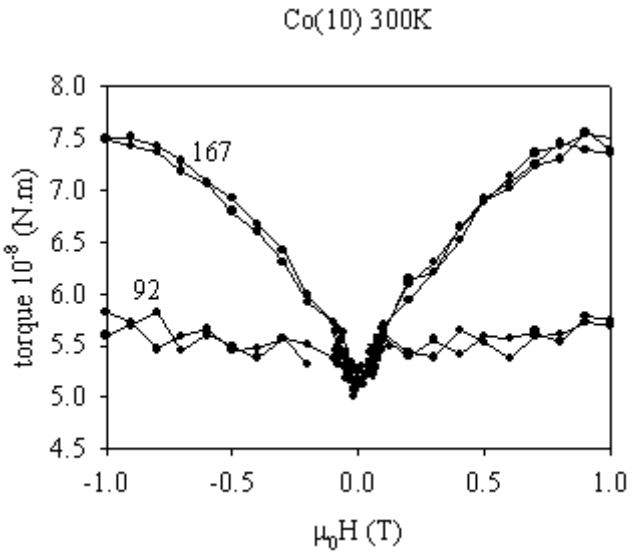

Fig. 10.14: The magnetisation isotherms measured at 300 K in sample positions at 92 and 167 degrees, corresponding to the directions of the hard and easy axis of magnetization, respectively.

10.5 Scanning probe microscopy

The topography of all samples was obtained in the contact mode. The mean roughness of the surface, which does not agree well with results calculated from the reflectivity curve simulation (Tab. 9.1), was determined. The example of the layer topography is depicted in Fig. 10.15. The images of the other samples are summarized in Appendix E.

The height of the features on the surface was the crucial parameter for setting the lift scan height (LSH) parameter in MFM imaging. Because the magnetic Co layer is isolated by 10 nm of SiO_2, theoretically the signal arising from the magneto-static interaction between the tip and the sample is decreased with respect to the sample without any diamagnetic cover (assuming the scanning parameters are same in both case). The mean height of features on the surface is more or less constant, bellow 5 nm.

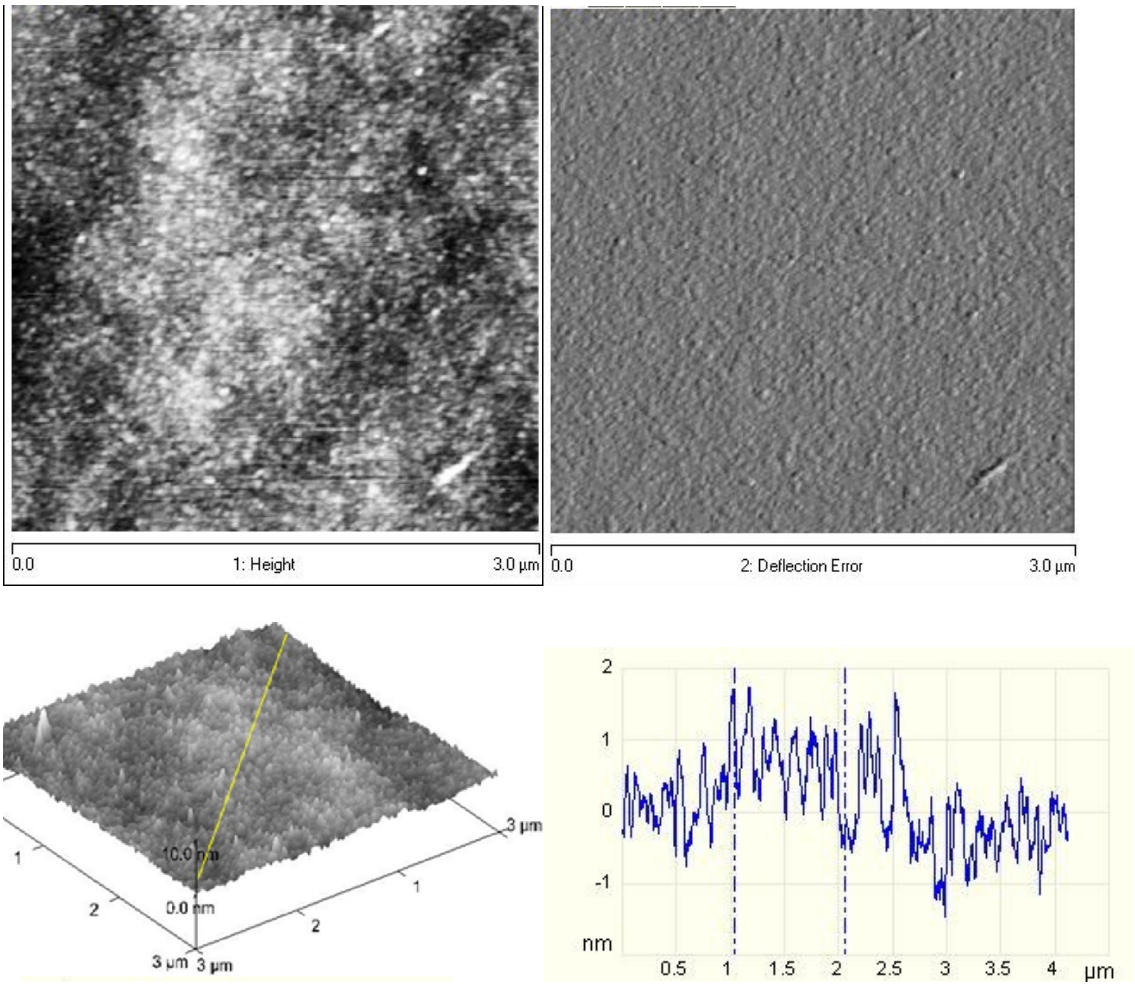

Fig. 10.15: The images of the Co5 sample, taken with the SNL-10 tip in TM. From the left: height, deflection error, 3D topography image and its cross section (represented by the yellow line on the 3D image).

10.6 MFM

As was shown in the previous chapters, the easy axis of magnetization lies in the film plain. The size of the domain in such in-plain magnetized films reaches hundreds of microns so it is clear that without a fortune, the boundary of two domains will not lie in the scanning area (approximately tens of microns) and observation of some internal domain magnetic structure could be possible.

10.6.1 The first experiments with magnetizing the samples

The magnetization measurements have shown that the samples (except the Co3) are in the blocked state at room temperature. Looking at the magnetization curves measured in parallel and perpendicular orientation (with subtracted diamagnetic contribution), the field of 1 T is sufficient in both cases to reach the saturated magnetization.

The samples were mounted directly on the scanner JV holder (with estimated magnetic field of 0.2 T) before the measurement. To orient at least few of the nanoparticles magnetic moments to the direction perpendicular to the film plane, the Co10 sample

was magnetized in 1 T magnet (the gradient of magnetic field was applied in a hand permanent magnet perpendicular to the film plane) before. Fig. 10.16 demonstrates the topography and the magnetic phase image of the Co10 sample, magnetized in the perpendicular direction. The image was taken in lift scan height (LSH) = 30 nm, bright and dark spots supposed to be the areas oriented in the directions opposite and parallel to the surface, respectively.

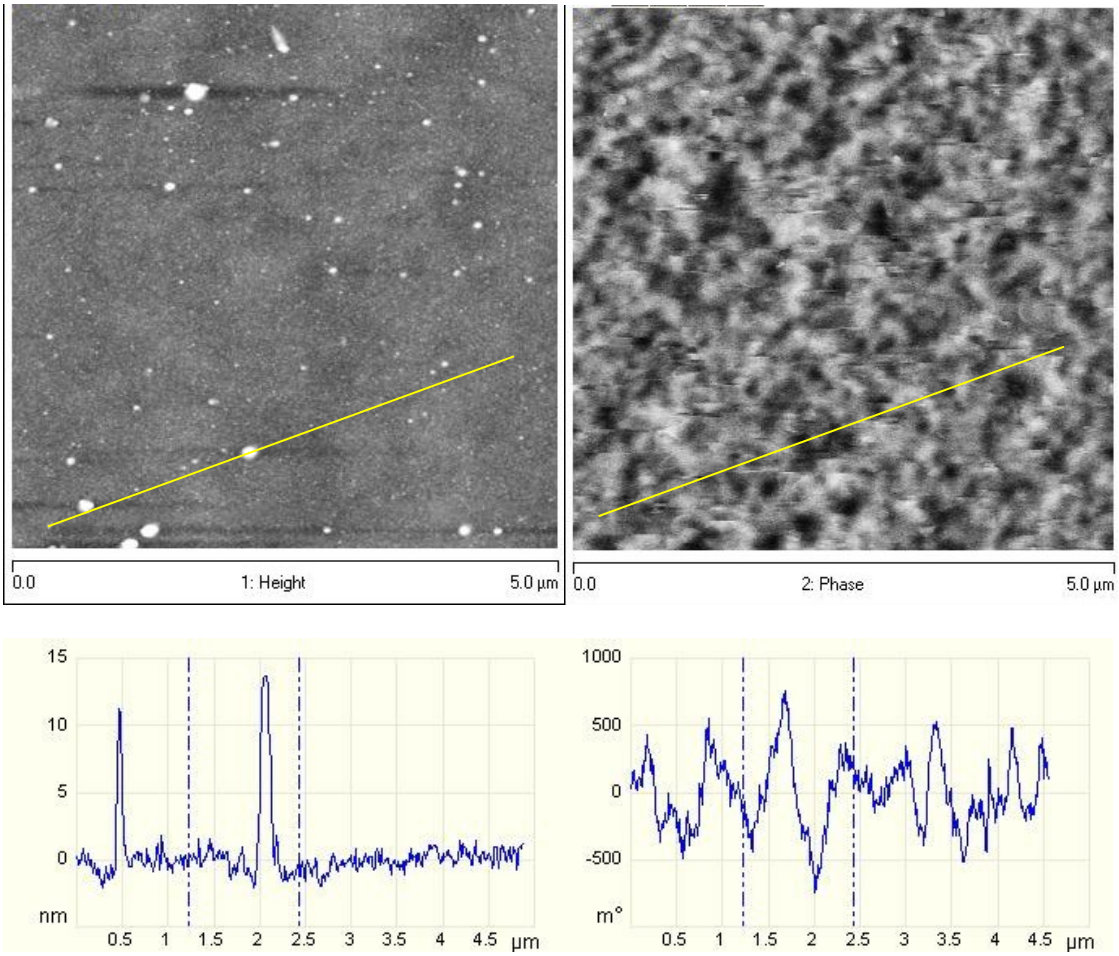

Fig. 10.16: MFM images of the Co10 sample. Left: topography, right: magnetic phase image; the yellow lines on the images represent the cross sections bellow. Scanning parameters: MESP probe, LSH 30 nm, scan rate 1 Hz, targeted amplitude 2 V.

As was estimated from the magnetization isotherms, the average magnetic moment of nanoparticles in Co10 film is in order of 10^4 μ_B which also determines the average particle diameter of approximately 100 nm. If it is assumed that the dark and bright areas belong either to separate particles or to the aggregates and the procedure for highlighting the boundaries between the areas (built in ImageJ software) is applied, it is possible to measure the largest size of the well defined grain. The resulting distribution of such determined particle diameter is depicted in Fig 10.17. The grain diameter obtained from MFM lies in interval from zero to one order of magnitude higher that the

mean diameter obtained from the magnetic measurements; thus it could be concluded that the magnetic structure of separate grains and their aggregates have been visualised.

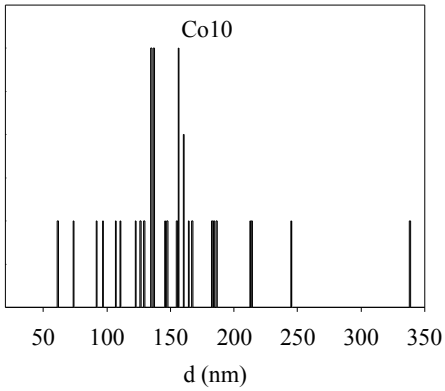

Fig. 10.17: The distribution of the particle diameters in Co10 sample, obtained from the statistical treatment of MFM phase image.

10.6.2 Evolution of the contrast with changing the LSH (Co5 sample)

When scanning the magnetic samples, the magneto-static interaction is decreasing in r^3, so the phase image contrast decreases with increasing lift scan height. To prove that the phase image contrast arises from the magnetostatic interaction in our case, the experiment in which the phase image was taken in different lift scanning heights (LSH) have been performed. As is demonstrated in Fig. 10.20, the phase contrast increases approaching the tip from the 100 nm down to the 20 nm.

10.6.3 Magnetizing the sample in in-plain orientation, at the constant LSH and different field

The Co5 sample was magnetized both in 0.5 and 5 T in parallel orientation. The Fig. 10.18 shows, that there is no significant difference between the phase scans of both films, captured at LSH = 20 nm. The sample magnetized in 5 T was expected to exhibit no or very little contrast, because all the moments should be oriented in one direction, parallel to the film plane. However, the phase roughness of both images differs in 0.3 %, which is the negligible difference. The most probable explanation of this phenomenon is that because films are magnetically soft, nanoparticles's magnetization is switched into the direction of the holder field (perpendicular to the surface) during the measurement so the magnetizing the samples in parallel orientation does not lead to stabilization of the magnetic moment in in-plain orientation during the MFM measurements.

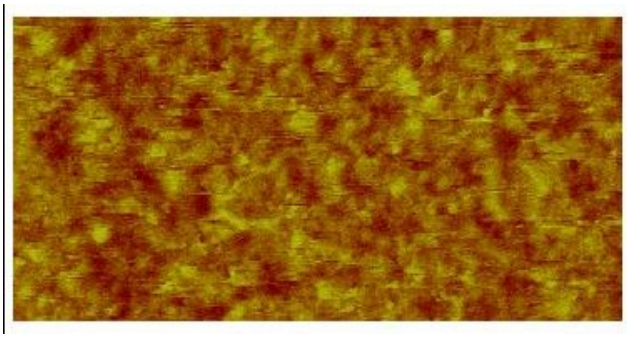

0.5 T (R_a 0.175 degree)

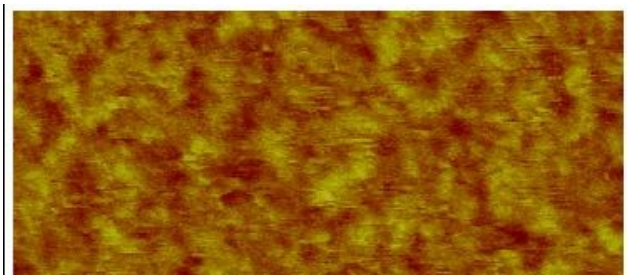

5 T (R_a 0.132 degree)

Fig. 10.18: The Co5 sample, magnetized in parallel orientation at 0.5 and 5 T, respectively. The magnetic phase images together with the cross-sections from the middle part of the image are illustrated. R_a is the value of the surface roughness.

10.6.4 Magnetizing the sample in orientation perpendicular to the film plane

Magnetizing the Co5 sample in field of 5 T for 1 hour in perpendicular orientation, the phase contrast was diminished, as expected. The topography, magnetic phase image and the cross sections are shown in Fig. 10.19. The phase contrast is increased up to 5 degrees what is far above the values obtained in previous experiments. Thus it could be

concluded that a kind of domain-stripes structure was induced. Unfortunately, sample exhibited so strong magnetization that the tip was attached to the surface even in scanning 100 nm away from surface and led to the destruction of the tip.

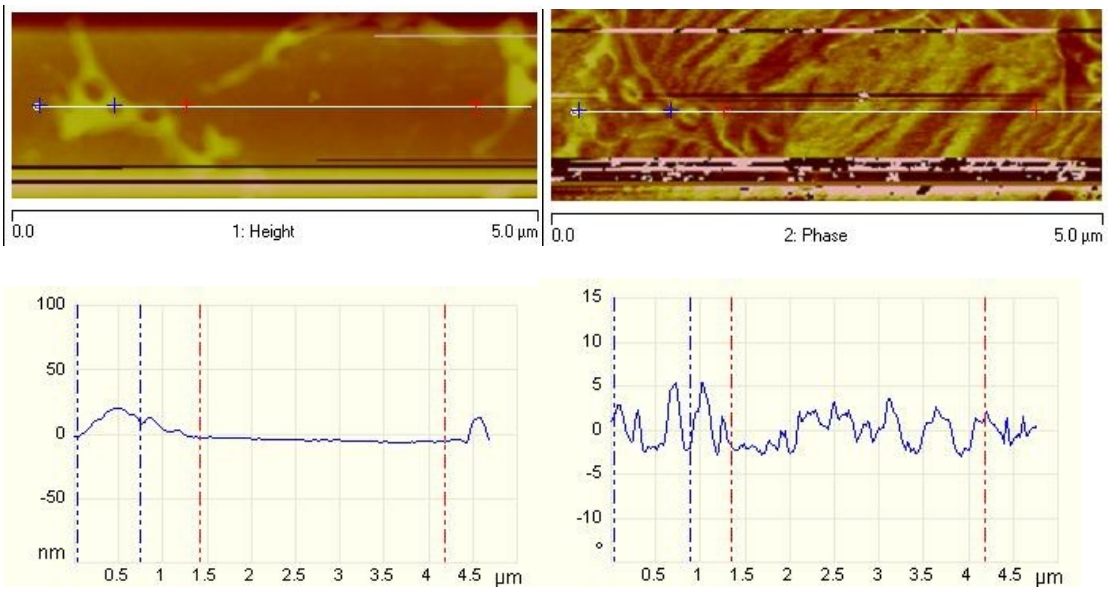

Fig. 10.20: Co5 sample magnetized perpendicular in 5 T. Scanning parameters: LSH 20 nm, scan rate 0.5 Hz, amplitude 1300 mV. The contribution of the topography was observed, but the plain areas in the central part of the image give the strong magnetic contrast. The image artefacts have arisen from strong magneto-static interaction, when the tip was attracted to the surface (lines on the images).

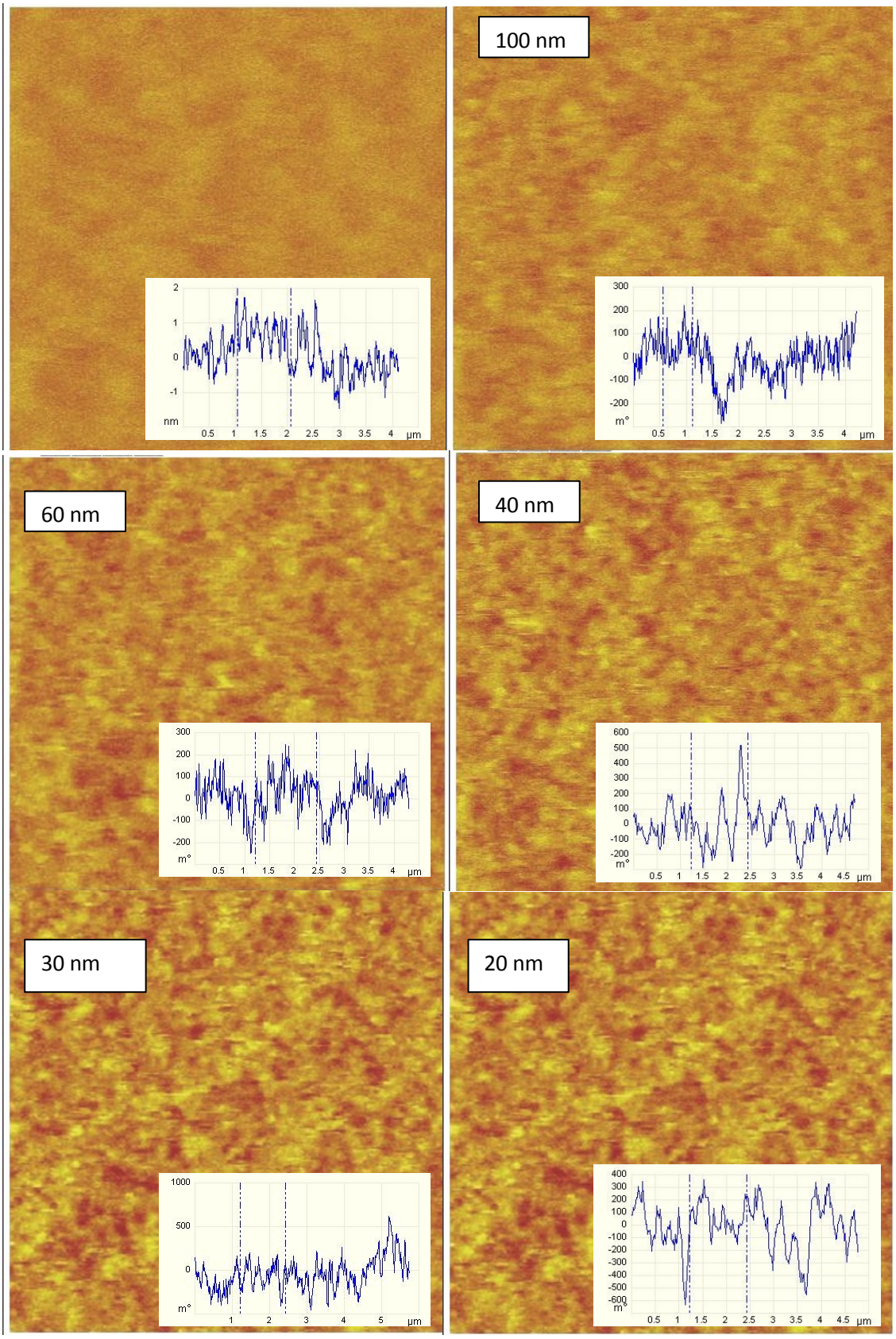

Fig. 10.20: The Co5 sample. The evolution of the contrast with decreasing LSH. The cross sections were taken in the middle of the phase images. The topography image is in the left corner. Size of the images is 5 µm.

10.7 Summary

The structure and the magnetic properties of SiO_2_Co(x)_Si(111) thin films and multilayers have been investigated. All results were discussed with respect to the assumption that layers are composed of granules (nanoparticles). Characterization of the compound and the structure by XRD has failed; analysis of the x-ray reflectivity curves highly probably showed that the thickness of the layers is of 30-40% higher than that one declared by the film grower. The determined density of single layers is lower than that of the bulk material which supports the granular structure scenario.

The magnetization measurement both in orientations parallel and perpendicular to the film plain were done. The temperature dependence of magnetization together with the appropriate magnetization isotherms signalise that the preferable orientation of film easy axis of magnetization is in plain.

The temperature dependence of magnetization measured in parallel orientation in small field (20-50 mT) up to 350, 500 and 700 K, respectively pointed out that the real blocking temperature of virgin samples lies in proximity of 450 K. The evolution of the blocking temperature in increasing field satisfies the requirements for SPM systems.

Analysing the magnetisation isotherms measured bellow and above this blocking temperature, the partial sintering of particles was observed even in heating the sample up to 500 K. The values of magnetic moments per particle determined from Langevin fit are in order 10^4 μ_B, corresponding to the 100 nm Co particles, supporting again the granular scenario.

It has to be mentioned that any significant difference in magnetic properties of single and multilayer samples was not observed, except the decrease of coercivity with increasing thickness of the layer, both in single and multi-layers.

The torque measurements of Co(10) and Co10 sample (the multi and single layer, respectively) gave the final evidence of preferable in-plain easy axis of magnetization

MFM phase images of thin films have been taken with magnetic tip in different tip-sample distances (lift scan heights) at samples magnetized in different fields (0.2, 0.5, 1 and 5 T, respectively) in the orientation parallel or perpendicular to the surface. The contrast on the phase images, bright and dark granules, was obtained. The domain-stripe structure was not observed which is not surprising result for films with in-plain magnetic anisotropy whose magnetic domains size is 10 times higher (at least) than the dimension of the scan. Also the evolution of contrast depending on the magnitude of the field in which the samples were magnetized is negligible. In conclusion, it is only possible to obtain magnetic contrast arising from the separate grains (aggregates).

Conclusion

The experimental part of the thesis consists of three quite independent parts concerning magnetic force microscopy, preparation and detail investigation of magnetic properties of cobalt-ferrite nanoparticles and finally, magnetic studies of SiO_2_Co(x)_Si(111) thin films and multilayers. However, it is the magnetic force microscopy which acts as the connection between these parts.

It has to be mentioned that during the time devoted to the work on this thesis, new technique, the scanning probe microscopy, has been established at the faculty. One of the key task of the theses was therefore installation and optimisation of the device and method. Now, as the key output of the thesis, it is possible to obtain topographical images of samples in sufficient resolution, calibrate the cantilevers both with spring constants lower and higher than 1, qualitatively analyse the tip adhesion on the surface and also visualise magnetic domains in the sample, if it is principally possible -with the available probes, at room temperature and ambient atmosphere and without the source of external magnetic field. The evidence of the last mentioned is demonstrated in Chap. 8, in which the images of magnetic structure obtained on the BFO-BFO columns are of the same nature as the images of this sample taken elsewhere.

The single-domain $CoFe_2O_4$ nanoparticles of average diameter 16, 15 and 8 nm have been prepared by the coprecipitation and the decomposition, respectively. The samples were investigated in detail with respect to the structural and especially magnetic properties. The superparamagnetic (SPM) behavior, strongly affected by inter-particle interaction, was observed. The 8 nm nanoparticles served as an educative example of super-spin-glass system.

Also the structural and magnetic properties of the thin films and multilayers have been studied, in the term of the granular structure obeying assumptions for a SPM system. The temperature and field dependences of magnetization in parallel and perpendicular film orientation together with the advanced torsion magnetometry experiments proved that the films have granular structure and also in-plain anisotropy is evolved.

As was previously declared, both the nanoparticles and thin films were used as the testing samples for the MFM. It has been observed that it is possible to visualise internal-domain magnetic structure through the 10 nm of insulating SiO_2 layer.

The MFM experiments on nanoparticles showed that it is possible to measure small magnetostatic interaction between the tip and the particle, but many further experiments necessary for optimising the scanning parameters and preparation of the single layer of particles are required. The further experiments are intensively developed with focus on qualitative and quantitative imaging of individual magnetic nanoparticles and fine domain structure of magnetic thin films.

Literature

[1] Feynmann R. P. (1960): *There is plenty room at the bottom*. Engineering and Science **23,** 25-36.

[2] Halperin W. P. (1986): *Quantum size effects in metal particles*. Rev. Mod. Phys. **58**, 533 – 608.

[3] http://www.nano.gov

[4] http://www.meti.go.jp

[5] http://ec.europa.eu/research/fp6

[6] Ascencio J. A., Rincon A., Canizal A. (2005): *Synthesis and Theoretical Analysis of Samarium nanoparticles: Perspective in Nuclear Medicine.* J. Phys. Chem. B **109**, 8806-8812.

[7] Bulte J., Duncan I., Frank J. (2002): *In vivo Magnetic Resonance Tracking of Magnetically Labeled Cells After Transplantation.* J. Cereb. Blood Flow Metab. **22**, 899-907.

[8] Jordan A., Scholz R., Wust P. et al. (1999): *Magnetic fluid hyperthremia: Cancer treatment with AC magnetic field induced excitation of biocompatible superparamagnetic nanoparticles.* J. Magn. Magn. Mater **201**, 413-419.

[9] Ferreira H. A., Graham D. L., Freitas P. P. et al. (2003): *Biodetection using magnetically labelled biomolecules and arrays of spin-valve sensors.* Biosens. Bioelectron. **18**, 7281-7.

[10] Tang S. Q. et al. : Coating of cobalt ferrite nanoparticles with silica for an in-vitro GMR spin-valve biosensors. *J. Nanosci. Nanotech.* Under review.

[11] Frenkel J. and Dorfman J. (1930): *Spontaneous and induced magnetization in ferromagnetic bodies*. Nature **126**, 274-275.

[12] Néel L. (1949): *Théorie du traînage magnétique des ferromagnétiques en grains fins avec application aux terres cuites*. Ann.Géophys. 5, 99-136.

[13] Jonsson P. (2008). *Superparamagnetism and Spin Glass Dynamics of Interacting Magnetic Nanoparticle Systems*. Adv.Chem.Phys. **128**, 191.

[14] Blundell S. (2001): *Magnetism in Condensed Matter , Oxford Master Series in Condensed Matter Physics.* Oxford University Press. Oxford.

[15] Ashcroft N. W and Mermin D. N (1976): *Solid State Physics*. Thomson Learning, Toronto.

[16] J. M. D. Coey (2009): *Magnetism and magnetic materials*. Cambridge University Press, Cambridge.

[17] Kittel Ch. (1953): *Introduction to solid state physics*. John Wiley and Sons, New York.

[18] Skomski R. (2008): *Simple models of magnetism*. Oxford University Press, Oxford.

[19] Tannous C. and Gieraltowski J. (2006): *The Stoner-Wohlfarth model of Ferromagnetism: Static properties*. Eur. J. Phys. **29**, 475-487.

[20] Stoner E. C. and Wohlfarth E. P. (1948): *Mechanism of magnetic hysteresis in heterogenous alloys*. Mat. Phys. Eng. Sci. **240**, 600 − 642 **.**

[21] Bland J., Master Thesis: *A Mossbauer spectroscopy and magnetometry study of magnetic multilayers and oxides*. Oliver Lodge Labs, Dept. Physics, University of Liverpool.

[22] PDF 4 crystallograpic database.

[23] Knobel M., Nunes W., Socolovsky L. M. et al. (2008): *Superparamagnetism and Other Magnetic Features in Granular Materials: A Review on Ideal and Real Systems*. Jour. Nanosci. Nanotechn. **8**, 2836-57.

[24] Chen Q., Zhang Z. J. (1998): *Size-dependent superparamagnetic properties of $MgFe_2O_4$ spinel ferrite nanocrystallites*. Appl. Phys. Lett. **73**, 3156.

[25] Rohrer H. (1968): *Magnetoresistance of dilute alloys*. Phys. Rev. **174**, 583 – 594.

[26] Fiorani D., Testa A. M. Lucani. D. et al. (2002): *Magnetic properties of maghemite nanoparticle systems: surface anisotropy and interparticle interaction effects*. Phys. B **320**, 122-26.

[27] Y. Komorida, Mito M., Deguchi. H et al. (2009): *Surface and core magnetic anisotropy in maghemite nanoparticles determined by pressure experiments*. Appl. Phys. Lett. **94**, 202503.

[28] Brown W. F. (1963): *Thermal Fluctuations of a Single-Domain Particle*. Phys. Rev. **130**, 1677.

[29] Shtrikman S. and Wohlfarth E. P. (1981): *The theory of the Vogel-Fulcher law of spin glasses*. Phys. Lett. A **85**, 467-70.

[30] Dormann J. L., Fiorani D., Chirkaoui R. et al. (1999): *From pure superparamagnetism to glass collective state in γ-Fe2O3 nanoparticle assemblies*. J. Magn. Magn. Mater **203**, 23-27.

[31] Dormann J. L., Fiorani D., Chirkaoui R. et al. (1999): *Collective glass state in a magnetic nanoparticle system*. Nanostr. Mat. **12**, 757-62.

[32] Dormann J. L, Bessais L., and Fiorani D. (1988): *A dynamic study of small interacting particles: superparamagnetic model and spin-glass laws*. J. Phys. C **21**, 2015.

[33] Berkov D. V and Gorn N. L. (2001): *Susceptibility of the disordered system of fine magnetic particles: a Langevin-dynamics study*. J. Phys: Cond. Mat. **13**, 9369.

[34] Dormann J. L., Fiorani D. and Tronc E. (1997): *Magnetic Relaxation in Fine-Particle Systems.* Adv. Chem. Phys. **98**, 283.

[35] Luo W., Nagel S., Rosenbaum T. F. et al. (1991): *Dipole interactions with random anisotropy in a frozen ferrofluid*. Phys. Rev. Lett. **67**, 2721.

[36] Sasaki M., Jonsson P. E., Takyama H. et al. (2005): *Aging and memory effects in superparamagnets and superspin glasses*. Phys. Rev. B **71**, 104405.

[37] Jonsson T., Nordblad P., Svedlindh. P. (1998): *Dynamic study of dipole-dipole interaction effects in a magnetic nanoparticle system.* Phys. Rev. B **57**, 497.

[38] Jonsson, P. E., Yosihino H., Mamyia H. et al. (2005): *Absence of strong rejuvenation in a superspin glass*. Phys. Rev. B **71.** 104404.

[39] Jonsson T., Svedlindh P., Hansen M. F. (1998): *Static Scaling on an Interacting Magnetic Nanoparticle System.* Phys. Rev. Lett. **81**, 3976.

[40] Tronc E., Fiorani D., Nogues M. et al. (2003): *Surface effects in noninteracting and interacting γ-Fe_2O_3 nanoparticles*. J. Magn. Magn. Mater **262**, 6-14.

[41] Vincent E. (2009): *Aging, rejuvenation and memory: the example of spin glasses.* University course, Sacley, France.
[42] Bassani G. (2005): *Encyclopedia Dictionary of Condensed Matter Physics*. Elsevier, Academic Press.

[43] Hubert A. and Schafer R. (1998): *Magnetic Domains The Analysis of Magnetic Microstructures* . Springer-Verlag, Berlin, Heidelberg.

[44] Poulopoulos P. and Baberschke K. (1999): *Magnetism in thin films*. J.Phys.: Condens. Matt. **11**, 9495-515.
[45] Buchan B. (2007): *Springer Handbook of Nanotechnology*. Springer, Verlag.

[46] Kharmouche A. et al. (2004): *Structural and magnetic properties of evaporated Co/Si(100) and Co/glass thin films*. J.Phys.D: Appl.Phys. **37**, 2583-87.

[47] Li M. and G. C. Wang. (2000): *In situ measurement of thickness dependence of magnetoresistance and magnetic hysteresis loops of ultrathin Co films on a SiO_2/Si(111)substrate*. Journ. Magn. Magn. Mater **217**, 199-206.

[48] Gubiotti G. and Carlotti G. (2003): *Dependence of the perpendicular anisotropy in Co/Au multilayers on the number of repetitions*. J. Appl. Phys. **93**, 7241-43.
[49] Gibaud A. and Hazra. S. (2000): *X-ray reflectivity and diffuse scattering*. Current Science **78**, 1467.
[50] Malý P. (2008): *Optika*. Karolinum, Praha

[51] Feynmann R. (2000): *Feynmannovy přednášky z fyziky 2*. Fragment, Praha.

[52] Bhushan B. and Marti M. (2007): SPM- *Principles of Operation, Instrumentation and Probes. Springer Handbook of Nanotechnology*. Springer, Verlag.

[53] Giessibl F. J. (2003): *Advances in atomic force microscopy*. Rev. Mod. Phys. **75**, 949.

[54] SPM Training Notebook (2005). Veeco Instruments Inc., California.

[55] http://www.veecoprobes.com

[56] Boisgard, R., Aimq J. P. and Couturier.G: (2007): *Dynamic operation modes of AFM: Non-linear behavior and theoretical analysis of the stability of the AFM oscillator*. Int. Journ. Non-lin. Mech. **42**, 673-80.

[57] http://www.nanosensors.com/

[58] Gan Y. (2009): *Atomic and subnanometer resolution in ambient conditions by atomic force microscopy*. Surf. Sci. Rep. **64**, 99-121.

[59] Bustamante C. and Keller.D. (1995): *Scanning force microscopy in biology*. Phys. Today **48**, 32-38.

[60] Leggett G. J., Brewer N. J., Chong. K. S. L. (2005): *Friction force microscopy: towards quantitative analysis of molecular organisation with nanometre spatial resolution*. Phys.Chem. **7**, 1107-20.

[61] Chen S. Wang T. (2006): *General solution to two-dimensional nonslipping JKR model with a pulling force in an arbitrary direction.* J. Col. Interf. Sci. **302**, 363-69.

[62] Jiunn-Jong, W. (2008): *Modification of Hertzian behaviour in heavily loaded contact in the DMT regime*. J. Phys. D: Appl. Phys. **41**, 185301.

[63] Schwarz, U. D. (2003): *A generalized analytical model for the elastic deformation of an adhesive contact between a sphere and a flat surface*. J. Col. Inter. Sci. **261**, 99-106.

[64] Israelachvili J. N (1992): *Intermolecular and surface forces*. Academic Press, London.

[65] Giessibl F. J., Bielefhlet H., Hembacher S. et al. (1999): *Calculation of the optimal imaging parameters for frequency modulation atomic force microscopy*. Appl. Surf. Sci.**140**, 352-57.

[66] Ohnesorge F and Binning G. (1993): *True atomic resolution by atomic force microscopy through repulsive and attractive forces*. Science **260**, 1451-56.

[67] Henderson M. A. (2002): *The Interaction of Water With Solid Surfaces: Fundamental.* Asp. Rev. **46**, 152.

[68] Giessibl F. J. (1995): *Atomic resolution of the silicon (111)-(7×7) surface by atomic force microscopy*. Science **267**, 68-71.

[69] Muller D.J. et al. (1995): *Imaging purple membranes in aqueous solutions at sub-nanometer resolution by atomic force microscopy*. Bioph. J. **68**, 1681-6.

[70] Rugar D. and Hansma P. K. (1999): *Atomic force microscopy*. Phys. Today **43**, 23-30.

[71] Giessibl F. J. (2007): *Non-Contact Atomic Force Microscopy and Related Topics.* Springer-Verlag.

[72] http://www.omicron.de

[73] Morgernstern M., Schwarz A. and Schwarz U. D. (2007): *Low-Temperature SPM . Spinger Handbook of Nanotechnology*. Springer-Verlag.

[74] Liebmann M., Schwarz A., Langkat S. et al. (2002): *A low-temperature ultrahigh vacuum scanning force microscope with a split-coil magnet*. Rev. Sci. Instrum. **73**, 3508-14.

[75] Lu Q., Chun Ch. and de Lozanne A. (1997): *Observation of Magnetic Domain Behavior in Colossal Magnetoresistive Materials With a Magnetic Force Microscope*. Science **276**, 2006-08.

[76] Xiao G., Ross J., Parasiris A. et al. (2000): *Low-temperature MFM studies of CMR manganites*. Phys. C: Superc. **341**, 769-70.

[77] Moser A., Hug. H. J., Parashikov I. et al. (1995*): Observation of Single Vortices Condensed into a Vortex-Glass Phase by Magnetic Force Microscopy*. Phys. Rev. Lett. **74**, 1847.

[78] Volodin A., Temst K., Van Haesendonc Ch. et al. (2000): *Imaging of vortices in conventional superconductors by magnetic force microscopy*. Phys. C. **332**, 156-59.

[79] Roseman, M. and Grutter P. (2002): *Magnetic imaging and dissipation force microscopy of vortices on superconducting Nb films.* Appl. Surf. Sci. **188**, 416-20.

[80] Castell M. R. (1997): *Atomic-resolution STM of a system with strongly correlated electrons: NiO(001) surface structure and defect sites*. Phys. Rev. B **55**, 7859-63.

[81] Hillebrecht, F. U. (2001): *Magnetic moments at the surface of antiferromagnetic NiO(100)*. Phys. Rev. Lett. **86**, 3419-22.

[82] Langkat, S. Holscher H., Schwarz A. et al. (2003): *Determination of site-specific forces between an iron coated tip and the NiO(001) surface by force field spectroscopy*. Surf. Sci. **527**, 12-20.

[83] Momida H. and Oguchi T. (2005): *First-principles study on exchange force image of NiO(001) surface using a ferromagnetic Fe probe*. Surf. Sci. **590**, 42-50.

[84] Okazawa T., Yagi Y and Kido Y. (2003): *Rumpled surface structure and lattice dynamics of NiO(001)*. Phys. Rev. B **67**, 195406.

[85] Kaiser U., Schwarz A. and Wiesendanger R. (2007): *Magnetic exchange force microscopy with atomic resolution*. Nature **446**, 522-25.

[86] Ramlan D. G., May S., Zheng J. et al. (2005): *Ferromagnetic Self-Assembled Quantum Dots on Semiconductor Nanowires*. Nano Lett. **6**, 50-54.

[87] Takamura Y., Chopdekar R., Scholl A. et al. (2006): Tuning Magnetic Domain Structure in Nanoscale $La_{0.7}Sr_{0.3}MnO_3$ Islands. Nano Lett. **6**, 1287-91.

[88] Agarwal G., Shchreiber S. Savla M. et al. (2009): Magnetic Force Microscopy of Superparamagnetic nanoparicles. Small 2008 **4**, 270-78.

[89] Rasa, M. and Philipse A. P. (2002): *Scanning probe microscopy on magnetic colloidal particles*. J. Magn. Magn. Mater **252**, 101-03.

[90] Dobson J. (2001): *Nanoscale biogenic iron oxides and neurodegenerative disease*. FEBS Lett. **496**, 1-5.

[91] Diebel C.E., Proksch R., Green C. R.et al. (2002): *Magnetite defines a vertebrate magnetoreceptor*. Nature **406**, 299-302.

[92] Martinelli A. L., Filho A. H., Franco R. F. et al. (2004): *Liver iron deposits in hepatitis B patients: association with severity of liver disease but not with hemochromatosisne mutations*. J. Gastroenetro.Hepatol. **19**, 1036-42.

[93] Ras, M., Kuipers B. W. M. and Philipse A. P. (2002): *Atomic Force Microscopy and Magnetic Force Microscopy Study of Model Colloids*. J. Col. Int. Sci. **250**, 303-15.

[94] Shen H., Long. D., Zhu L. et al. (2006): *Magnetic force microscopy analysis of apoptosis of HL-60 cells induced by complex of antisense oligonucleotides and magnetic nanoparticles*. Biophys. Chem. **122**, 22.

[95] Mironov V., Nikitush D., Bins Ch. et al. (2007): *MFM Contrast Simulation For Low-Coercive Ferromagnetic and Superparamagnetic Nanoparticles in an External Magnetic Field*. IEEE Trans. Magn. **43**, 3961-3963.

[96] Tartaj P., Morales M. P., Serna J. et al. (2003): *The preparation of magnetic nanoparticles for biomedical applications*. J.Phys.D: Appl.Phys. **36**, R182-R197.

[97] Valvoda V., Lukáč P., Polcarová M. (1992): *Základy strukturní analýzy*. Karolinum, Praha.

[98] Wiliams D. and Carter C. B (1996): *Transmission Electron Microscopy: A Textbook for Materials Science*. Plenum Press, New York.

[99] Nelms S. (2007): *Inductively Coupled Plasma Mass Spectrometry Handbook*. Blackwell Publishing. Oxford.

[100] PANalitical X'Pert Pro MRD manual (2003). PANalitical, Almelo, Netherlands.

[101] Rodriguez – Carvajal J. (2000): *FullProf User's Guide manual*. CEA-CRNS, France.

[102] Rodriguez – Carvajal J (2000): *Study of Micro-Structural Effects by Powder Diffraction Using the Program FULLPROF* . CEA-CRNS, France

[103] Bruker Diffractomerter User's Manual (2001), Bruker AXS GmbH, Karlsruhe.

[104] PPMS- Physical Property Measurement System User's Manual (2004). Quantum Design, San Diego.

[105] MPMS- Magnetic Property Measurement System User's Manual (2004). Quantum Design, San Diego

[106] Nanoscope software 7.3. manual (2005). Veeco Instruments Inc., San Diego

[107] Serry F. M. (2005): *Thermal Tune solution to the Cantilever Spring Constant Problem*. Veeco Instruments Inc., San Diego.

[108] Hutter J. L. and Beachhoefer J. (1993): *Calibration of atomic-force microscope tips*. Rev. Sci. Instrum. **64**, 1868.

[109] Dix N., Mularidharan R., Guyonnet J.et al. (2009): *On the strain coupling across vertical interfaces of switchable $BiFe_2O_3 – CoFe_2O_4$ multiferroic nanostructures*. Appl. Phys. Lett. **95**, 062907.

[110] Granitzer P., Rumpf K. and Roca. A. et al. (2010): *Investigation of Mesoporous Silicon Based Ferromagnetic Nanocomposite*. J. Magn. Magn. Mater **322**, 1343- 1364.

[111] Naiden E. P., Zhurlavev V. A., Itin V. I et al. (2006): *Magnetic properties of nanosized hexaferrite powders*. Chem. Mat. Sci. **45**, 1573 – 8779.

[112] Chinnasamy C. N., Jeyadevan B., Perales-Perez O. et al. (2003): *Size-Control and Size-Selection at the Nanosize Level: Production of CoFe2O4 Nnaoparticles of Unusual High Coercivity at Room Temperature*. Nanotech. **3**, 134-136.

Appendix A

Cook Book of Magnetism in Granular Nanoparticle Systems or Which System We Are Dealing With?

1) The first step is to measure the ZFC-FC curves. You should keep in mind that pure SPM behavior is very rare-observed in extremely diluted samples and so there is usually some kind of interparticle interactions (especially in powder sample).

   If your sample is composed of nanoparticles, ZFC-FC curves look like those in Fig. A.1, M(T) above T_B obeys Curie law, your sample exhibit superparamagnetic behavior. If the maximum of the ZFC curve, T_{MAX} is not the coinciding point of ZFC-FC curve, T_{DIFF}; there is the significant particle size distribution in the sample

   If there is the saturation at the beginning of the FC curve, you have to consider interparticle interaction. Theoretically, 1/M(T) above T_B should obey Curie law in case of SPM with interaction or Curie-Weiss law in case of SFM. If no one of these laws is fulfilled, maybe the system is behaving like a super spin glass. To prove it, further measurements have to be done.

2) Magnetization loops

Measuring the magnetization loops at different temperatures for superparamagnetic sample, following criteria should be fulfilled:

- Measurements of magnetization loops M(H) at different temperatures plotted in Langevin scaling should converge to the single one, Langevin's curve (if the distribution of the grain size is not considered).

- Magnetization isotherms are un-hysteretic above T_B, in other case there is the particle size distribution in the sample; the part of particles with higher sizes have blocking temperatures determined from ZFC curve maximum.

- Fitted size distribution is temperature independent.

3) Relaxation phenomena

To obtain characteristic relaxation time τ_0 of SPM system, Arrhenius law is used for fitting the frequency dependence of blocking temperature from ac susceptibility measurements.

In case of the system with interparticle interactions, the use of Vogel –Fulcher formula usually gives satisfactory results for all systems with interaction, not considering their strength. Thus measuring the ac susceptibility in zero external field with further

applying of Vogel –Fulcher law is not sufficient to resolve the systems with weak and strong interparticle interactions (SSG or SSG-like); thus the additional experiments have to be done.

In that case, measuring the ac susceptibility in non-zero external field and using the formula (2-9) can definitely determine if the interactions are strong or not. Finally, if the parameters agree with those of SSG (or SSG-like), it is necessary to do last experiment and to choose between them.

4) Aging and memory effects

Measuring the M(T) dependence at waiting time, the memory effect, is the method how to experimentally distinguish between the super-spin-glass and something what has all attributes of SSG except one (sth. called SSG-like behavior).

In a SSG bellow T_f, the single super-spins create the stable clusters which relaxation time is much longer than the relaxation time of spins and superspins. Applying the magnetic field, it takes the time since clusters 'relax' to the energetically most favourable position by turning their total magnetic moment in the field direction.

In a system exhibiting SSG-like behavior; the clusters are not stable all the time, particles (super-spins) are flowing between them or create new ones. The measuring time is too long to observe this type of dynamics, mean value of magnetization is more or less independent on waiting time because of continuous fluctuations, so the ac susceptibility measurements is not the proper one to detect this type of behavior.

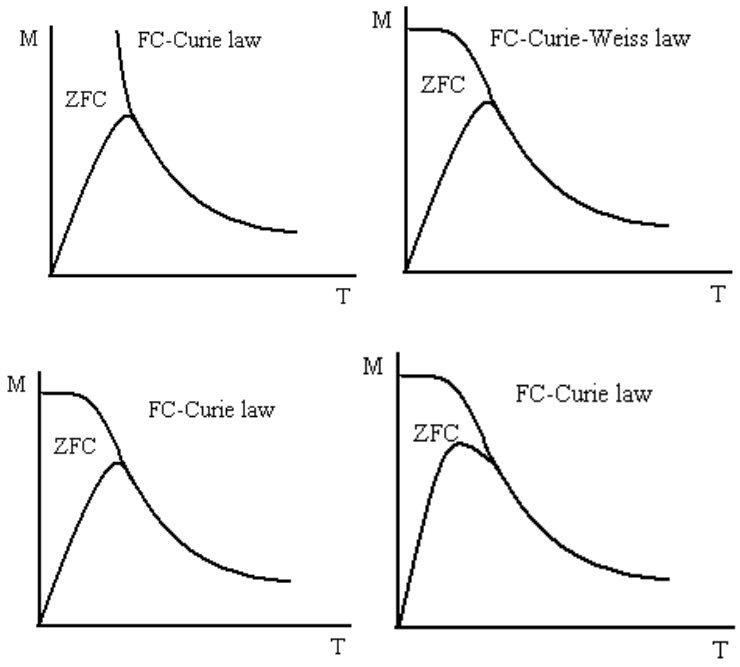

Fig. A.1: The ZFC-FC curves for superparamagnet, superferromagnet, superparamagnet with interparticle interactions and SPM with interparticle interaction together with particle size distribution.

Appendix B

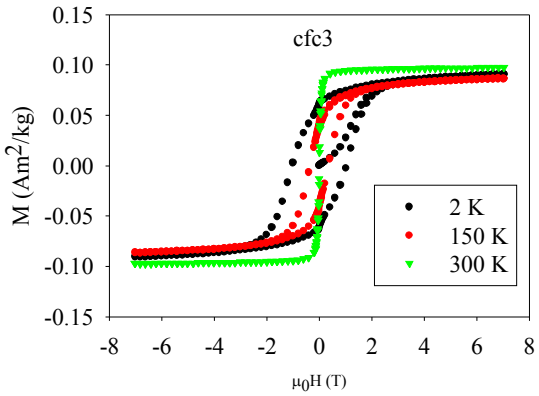

Fig. B.1: Magnetization isotherms for CFC3 sample.

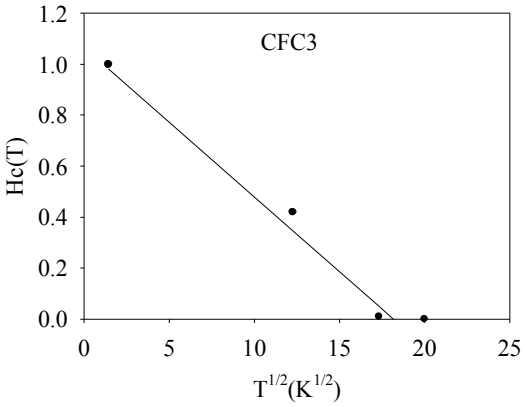

Fig. B.2: Temperature dependence of the H_C bellow the T_B.

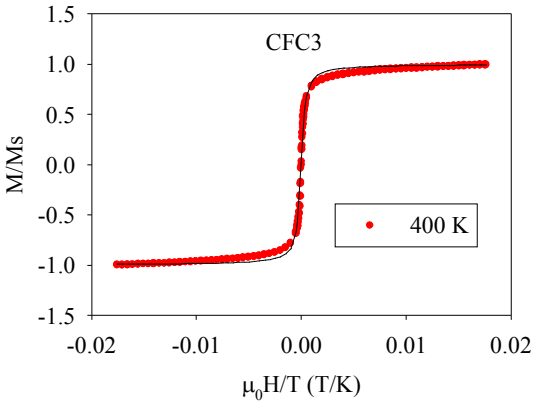

Fig. B.3: The Langevin fit (red curve) of the unhysteretic magnetization isotherm for the CFC3 sample.

Table B.1: The phase contrast of selected nanoparticles, obtained from the cross-sections of the images taken with different probes on magnetised and non-magnetised CFD2 sample in different LSH. Also the particle diameters and heights are summarised. The red, green and blue highlighted numbers connect the particles of he same size.

experiment	height (nm)	size(nm)	LSH (nm)	phase (°)
MFM Magnetised sample	11.0	65	80	0.35
	6.0	71	80	0.45
	13.0	85	80	0.29
	8.7	71	80	0.10
	8.8	66	80	0.14
	9.2	71	80	0.30
	12.8	74	80	0.21
	13.8	77	80	0.28

experiment	height (nm)	size(nm)	LSH (nm)	phase (º)
AFM Nonmagnetic sample	11.3	57	80	0.23
	11.0	39	80	0.24
	15.6	55	80	0.18
	14.2	94	80	0.34
	10.8	94	80	0.26
	8.5	44	80	0.00
	8.8	38	80	0.00
	10.0	39	80	0.00
	8.8	36	80	0.00
	9.0	20	80	0.00
	17.8	86	50	0.10
	12.7	69	50	0.07
	12.4	38	50	0.06
	9.6	21	50	0.06
	5.0	21	50	0.00
MFM Non-magnetised sample	4.0	50	50	0.92
	5.3	68	50	1.14
	6.3	103	50	0.97
	15.0	93	60	0.18
	6.5	42	60	0.12
	7.5	39	60	0.14
	6.6	58	60	0.10
	5.3	39	60	0.06
	11.9	73	60	0.15
	14.8	83	40	0.21
	7.5	43	40	0.13
	6.5	43	40	0.08
	6.6	59	40	0.09
	12.5	85	40	0.14
	6.8	51	40	0.14
	6.8	59	40	0.13
	15.2	162	20	4.39
	4.4	71	20	2.87
	4.1	66	20	2.30
	4.5	81	20	2.15
	6.7	85	20	3.84
	4.8	69	20	2.83
	7.1	55	20	2.84
	7.6	124	20	2.54

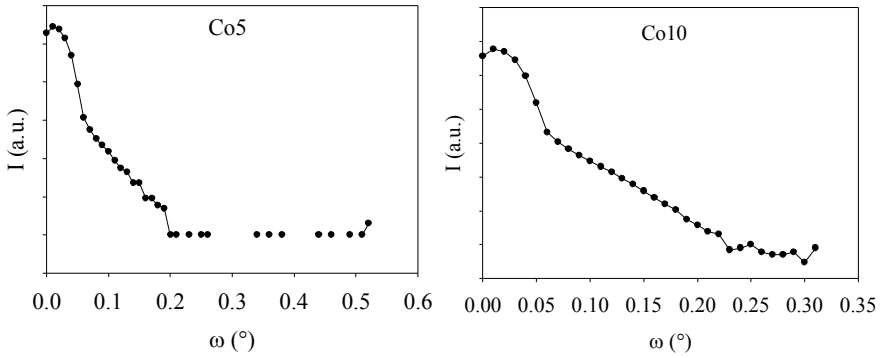

Fig. C.1: The angular dependence of reflectivity for the Co5 and Co10 samples, respectively

Co(3) sample

Following figures illustrate the fitting procedure of the reflectivity curve, the evolution of the extrapolated curves on the fitting parameters such as density (ρ), layer thickness (t) and the roughness (r), respectively. The 2nd and 3rd rows in all tables represent the parameters of Co/SiO_2 multilayer composed of 9 layers.

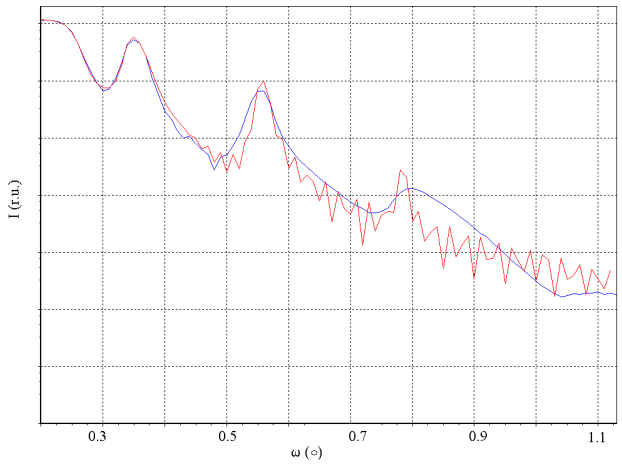

layer	ρ (g/cm^3)	t (nm)	r (nm)
Si	2.3	-	0
Co	6.66	4.01	0.67
SiO_2	2.39	13.85	1.99
Co	6.51	3.513	2.34
SiO_2	1.95	8.9	1.39

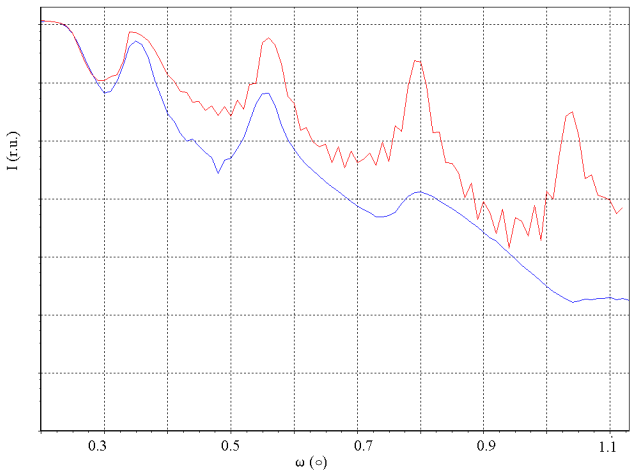

layer	ρ (g/cm^3)	t (nm)	r (nm)
Si	2.3	-	0
Co	7.5	3.8	0
SiO_2	2.3	13.8	0
Co	7.5	3.5	0
SiO_2	2.1	12	0

Fig. C.2: The measured (blue) and simulated (red) reflectivity curves for Co(3) samples, the parameters in table

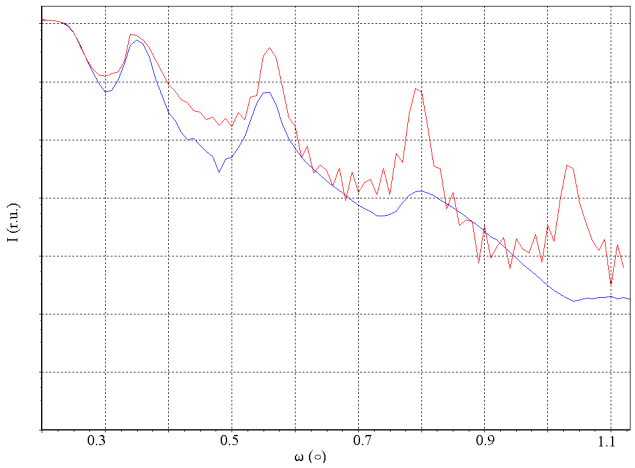

layer	ρ (g/cm^3)	t (nm)	r (nm)
Si	2.3	-	0
Co	7.0	3.8	1
SiO_2	2.3	13.8	1
Co	7.0	3.5	0.2
SiO_2	2.2	12	1

Fig. C.3: The measured (blue) and simulated (red) reflectivity curves, the parameters are in the table.

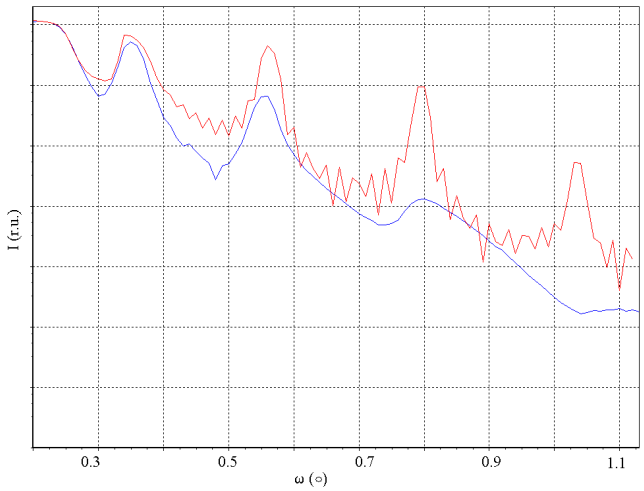

layer	ρ (g/cm^3)	t (nm)	r (nm)
Si	2.3	-	0
Co	8.9-7	3.9	1
SiO_2	2.4	13.8	1
Co	7.0	3.5	0.2
SiO_2	1.8	9	1

Fig. C.4: The measured (blue) and simulated (red) reflectivity curves, the parameters in the table.

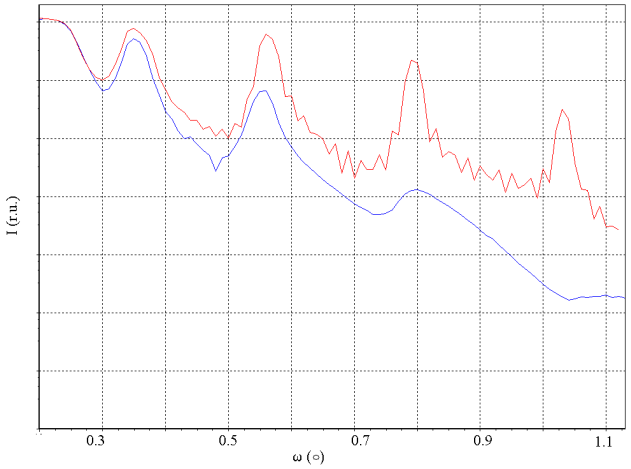

layer	ρ (g/cm^3)	t (nm)	r (nm)
Si	2.3	-	0
Co	8.9-7	3.9	0
SiO_2	2.6-2.4	13.8	0
Co	7.0	3.4	0.2
SiO_2	1.8	9	0

Fig. C.5: The measured (blue) and simulated (red) reflectivity curves, the parameters are in the table.

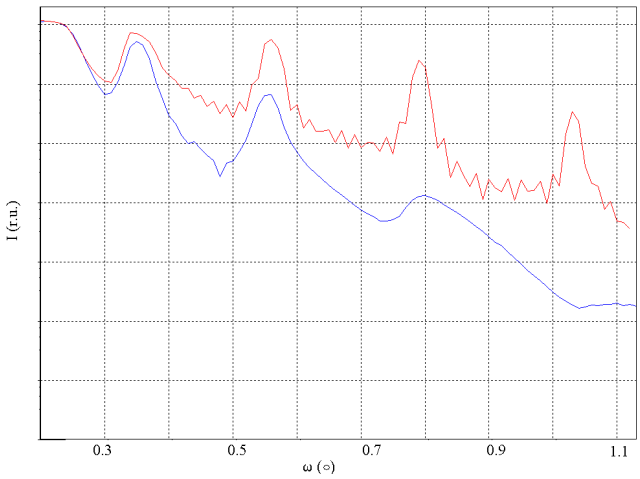

layer	ρ (g/cm^3)	t (nm)	r (nm)
Si	2.3	-	1.0
Co	8.0-7.0	3.78	1.8
SiO_2	2.6-2.3	13.99	1.8
Co	7.0	3.40	0.5
SiO_2	2.3	12.90	1.8

Fig. C.6: The measured (blue) and simulated (red) reflectivity curves, the parameters are in the table.

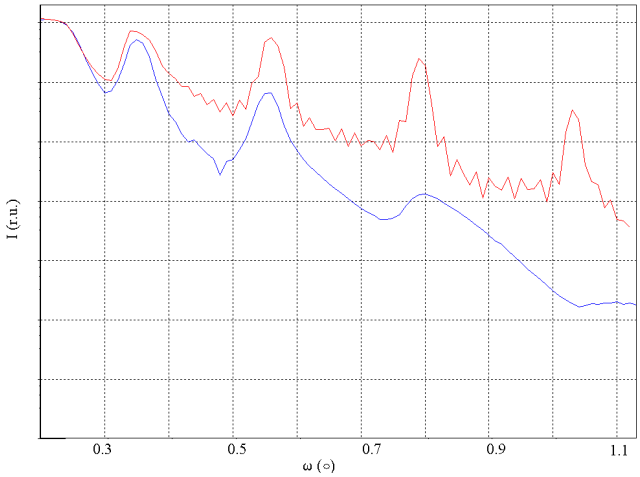

layer	ρ (g/cm^3)	t (nm)	r (nm)
Si	2.3	-	0
Co	8.9-7	3.9	0
SiO_2	2.6-2.2	13.8	0
Co	7.9	3.4	0
SiO_2	2.1	13	0

Fig. C.7: The measured (blue) and simulated (red) reflectivity curves, the parameters are in the table.

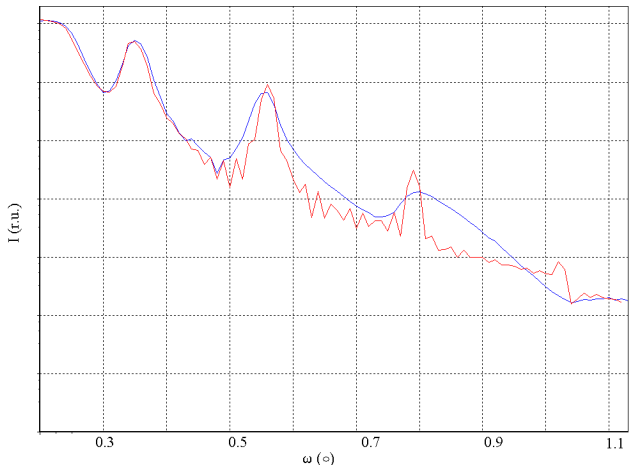

layer	ρ (g/cm^3)	t (nm)	r (nm)
Si	2.3	-	1.00
Co	8.9-6.3	3.58	1.93
SiO_2	2.2	14.06	2.70
Co	6.45	3.57	1.98
SiO_2	2.33	13.7	3.145

Fig. C.8: The measured (blue) and simulated (red) reflectivity curves, the parameters are in the table.

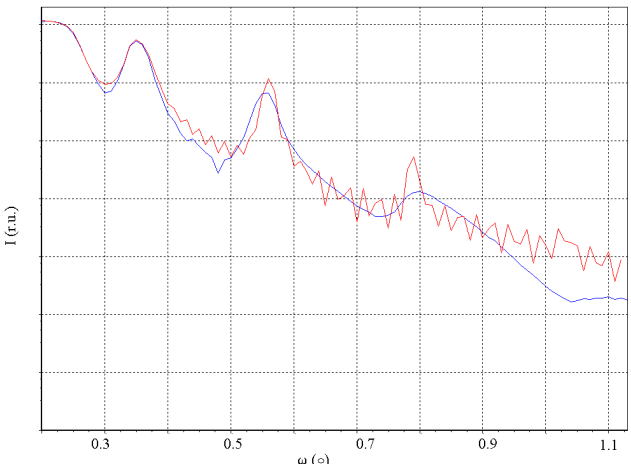

layer	ρ (g/cm^3)	t (nm)	r (nm)
Si	2.3	-	1.0
Co	8.0-6.84	4.01	1.8
SiO_2	2.31	13.75	3.0
Co	6.39	3.65	0.8
SiO_2	2.14	9.65	2.0

Fig. C.9: The measured (blue) and simulated (red) reflectivity curves for the Co(3) sample, the parameters are in the table.

Appendix D

In plain magnetic measurements

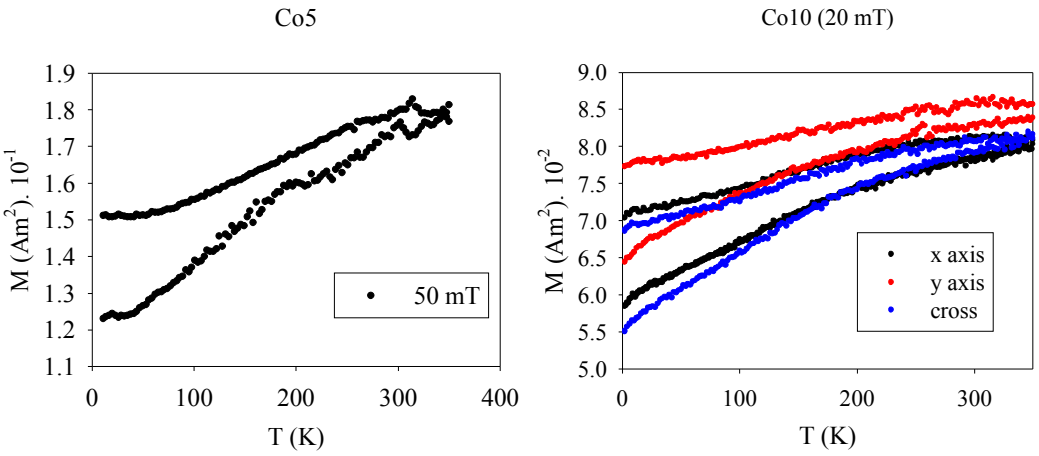

Fig. D.1: The Zfc-c curves for the Co5 (left) and Co10 samples, measured in small fields. In the Co10 sample, T_{DIFF} in y axis is higher than for x and cross. The shift of absolute values of magnetization is just the additional constant signal of magnetometer.

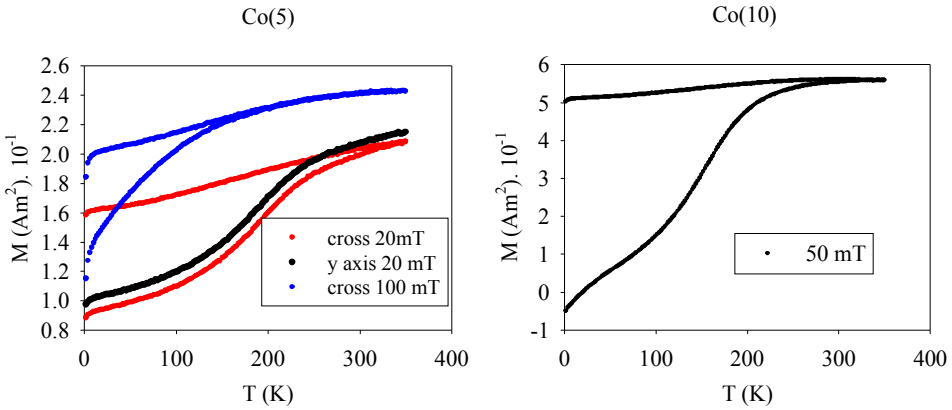

Fig. D.2: The ZFC-FC curves for the Co5 (left) and Co(10) (right) samples, measured in small fields. In the Co10 sample, T_{DIFF} in y axis is higher than for x and cross.

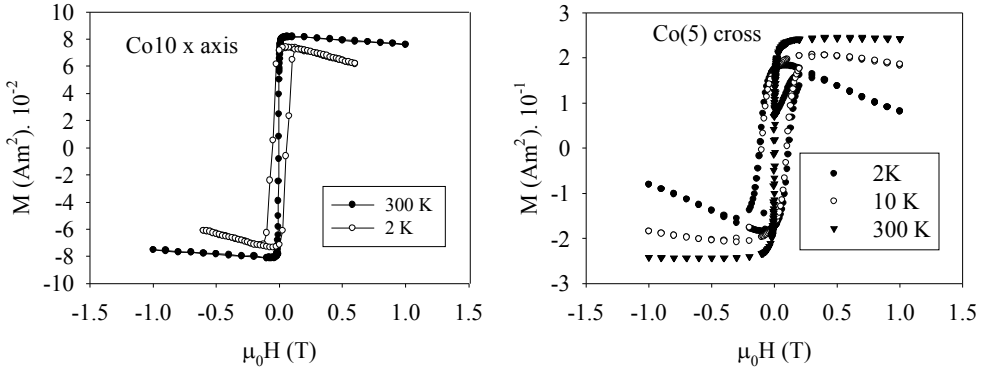

Fig. D.3: The magnetization isotherms for the Co10 (left) and Co(5) (right) samples, measured at different temperatures. The curves measured at low temperatures exhibit the diamagnetic contribution.

Perpendicular magnetic measurements

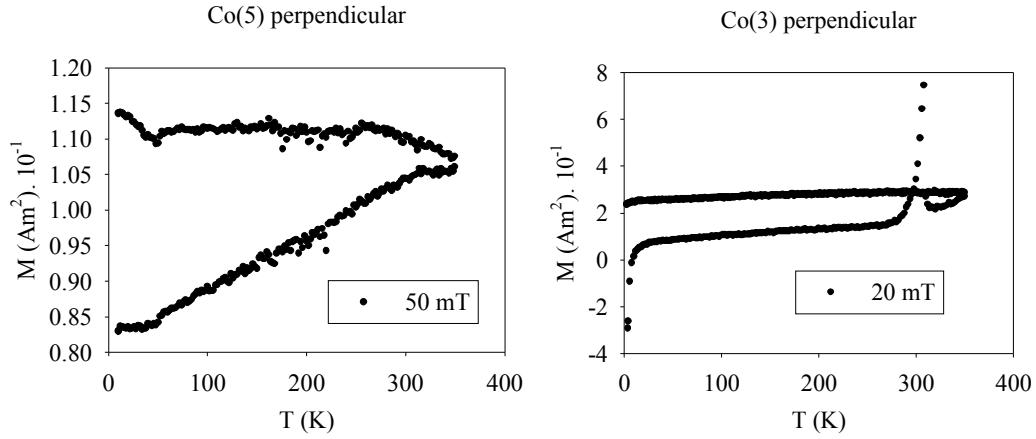

Fig. D.4: The ZFC-FC curves for the Co(5) (left) and Co(3) (right) samples measured in perpendicular orientation to the small field. The cusp on the Co(3) ZFC curve is the artefact of the measurement.

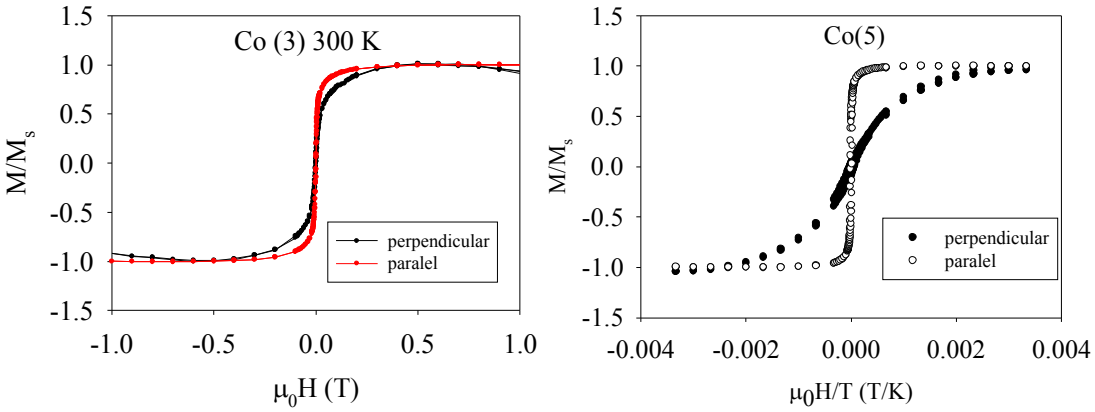

Fig. D.5: The magnetization isotherms measured at 300 K in parallel and perpendicular orientation for Co(3) and Co(5)samples, respectively. It is obvious, the MAE (area enclosed by curves) is higher in case of thicker sample, Co(5), as expected.

Torsion magnetometry

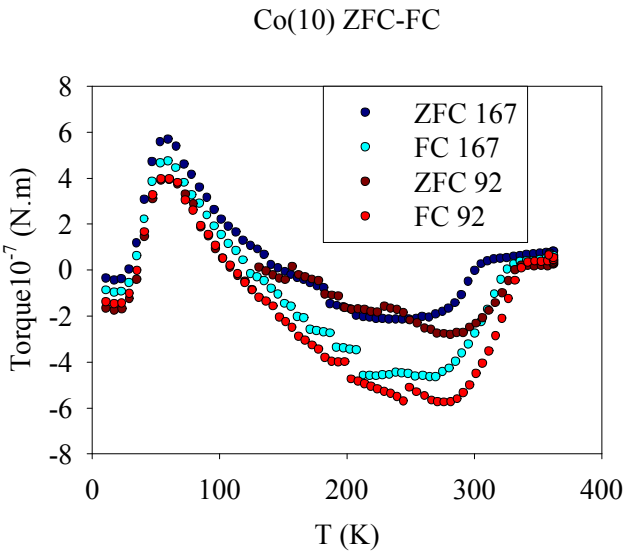

Fig. D.6: The ZFC-FC curves for Co(10) sample, measured in sample position at 167 and 92 degree with respect to the field direction (should be the directions of easy and hard axis, respectively). The evolution of curves is probably given by the artefacts originating from the chip.

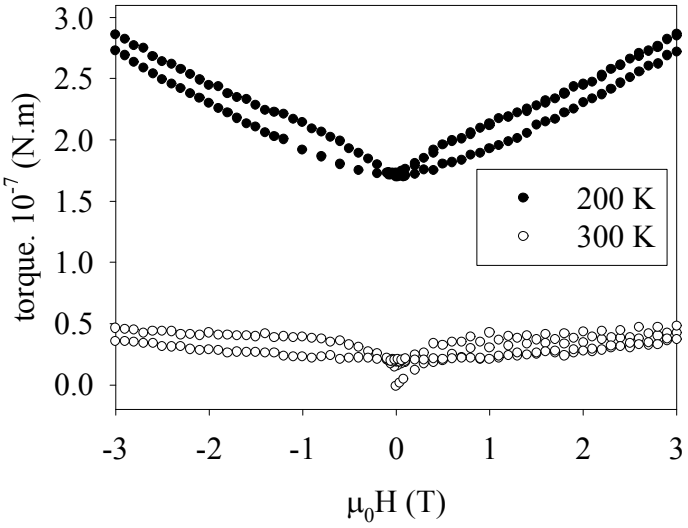

Fig. D.7: Magnetisation isotherms for Co(10) sample, measured in directions of easy and hard axis, respectively. The strong diamagnetic contribution and also demagnetising field contribution are present.

Appendix E

Co3 sample

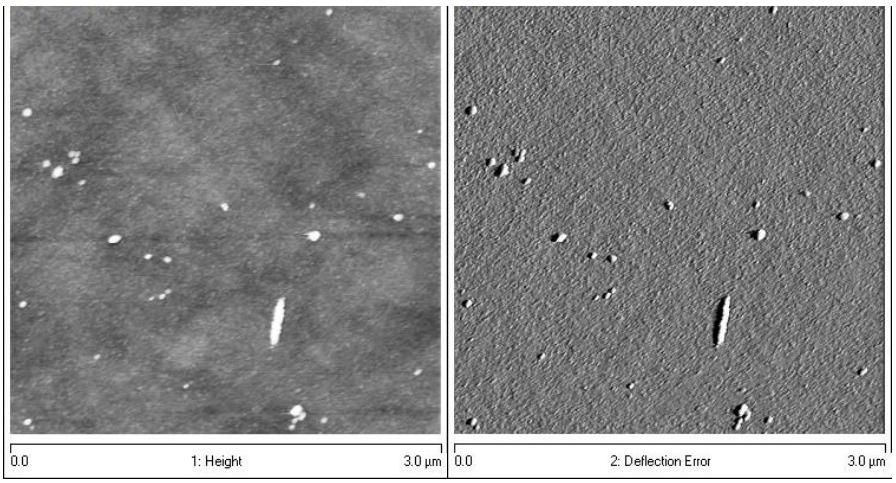

Fig. E.1: The topography height (left) and the deflection error of the Co3 sample, measured in CM with SNL-10 A probe.

Co5 sample

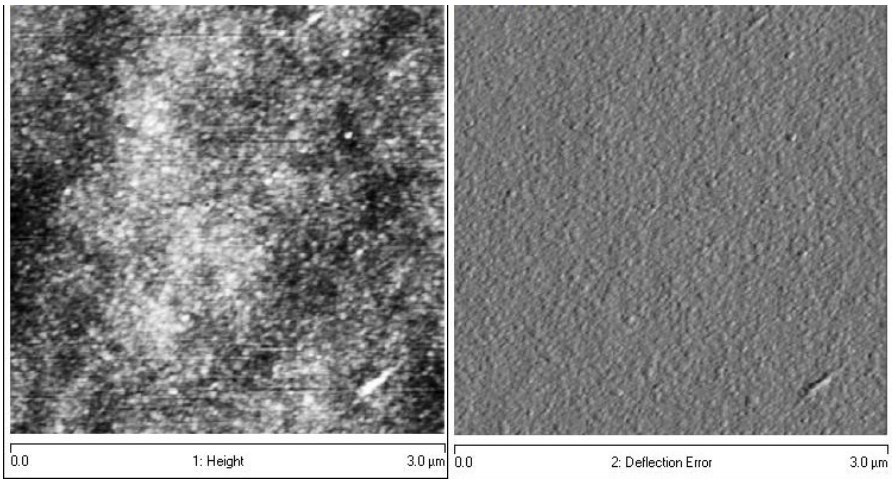

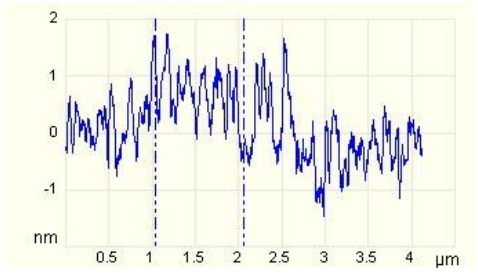

Fig. E.2: The topography height (left) and the deflection error of the Co3 sample, measured in CM with SNL-10 A probe. The cross section taken in the middle of the height image is depicted bellow.

Co(3) sample

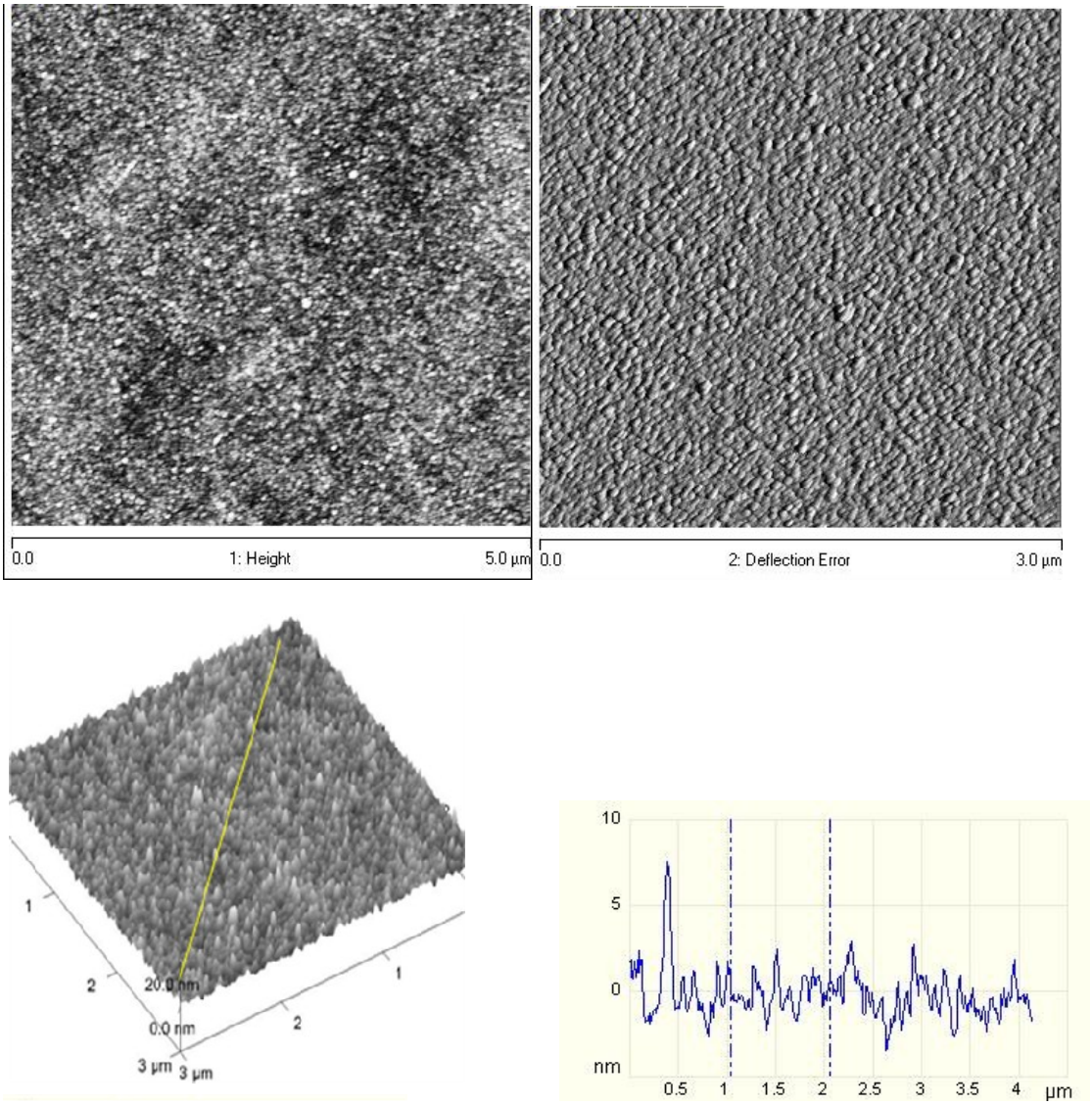

Fig. E.3: The topography height (left) and the deflection error (right) of the Co(3) sample. The 3D height cross image and the cross section (represented by the yellow line) are depicted bellow. The images were taken in the CM with the SNL-10 A probe.

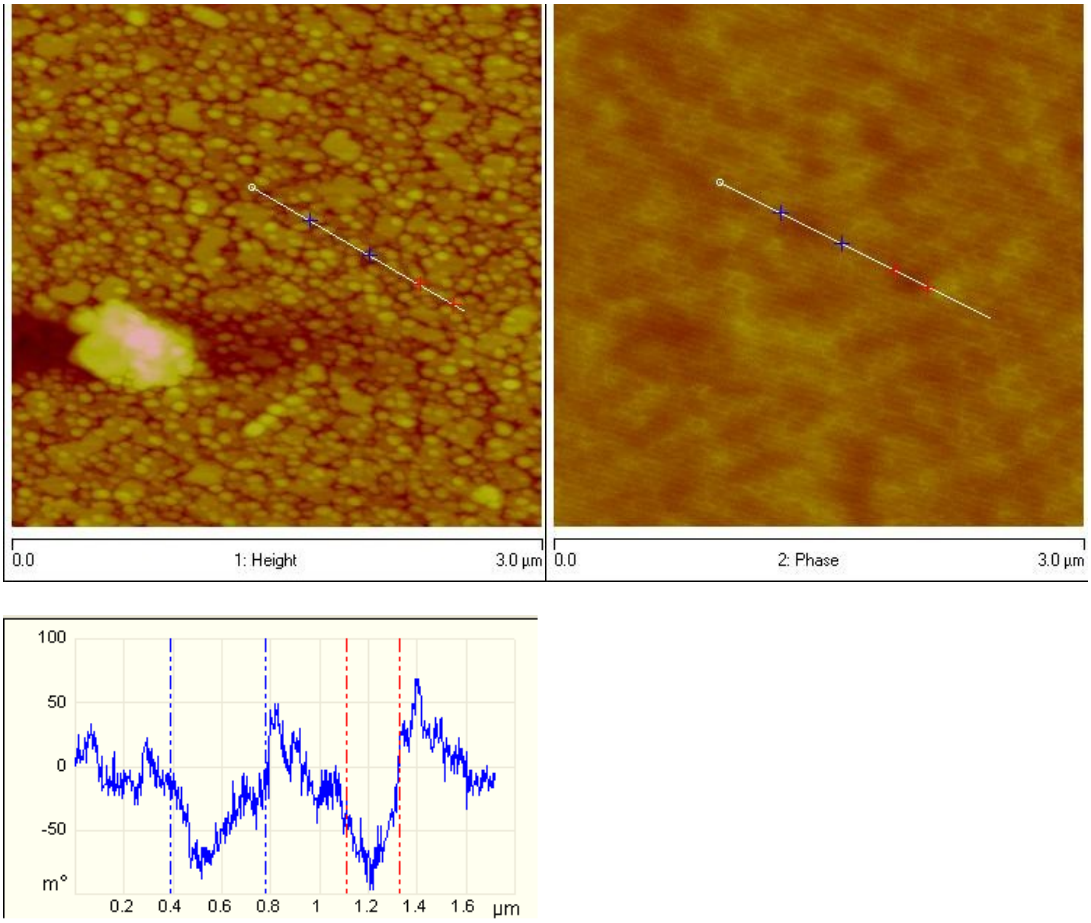

Fig. E.4: CFO-BFO columns scanned in MFM mode with the MESP tip: topography, phase and the phase cross section bellow (represented by the line in both images). It is obvious that the phase contrast is at least 6× lower than in case of scanning with the MESPHM probe (Chap. 9).